SPATIALLY AND TEMPORALLY RESOLVED STUDIES OF ELECTRON TRANSFER REACTIONS IN SOLUTIONS AND THIN ORGANIC SURFACES

by

Alexei V. Tivanski

BS, Moscow Institute of Physics and Technology, 1999

MS, Moscow Institute of Physics and Technology, 2001

Submitted to the Graduate Faculty of

University of Pittsburgh in partial fulfillment

of the requirements for the degree of

Doctor of Philosophy

University of Pittsburgh

2005

UNIVERSITY OF PITTSBURGH

FACULTY OF ARTS AND SCIENCES

This dissertation was presented

by

Alexei V. Tivanski

It was defended on

April 15, 2005

and approved by

Prof. Peter E. Siska

Prof. David H. Waldeck

Prof. Tomasz Kowalewski

Prof. Gilbert C. Walker

Dissertation Director

SPATIALLY AND TEMPORALLY RESOLVED STUDIES OF ELECTRON TRANSFER REACTIONS IN SOLUTIONS AND THIN ORGANIC SURFACES

Alexei V. Tivanski, PhD

University of Pittsburgh, 2005

ABSTRACT

Understanding electron transfer (ET) on the nanoscale is important to both the frontier of fundamental science and to applications in molecular electronics. Ultrafast infrared spectroscopy and conducting probe atomic force microscopy (CP-AFM) are valuable tools in studies of temporally and spatially resolved ET reactions in solutions and surfaces. Static optical metal-metal charge transfer spectra, infrared absorption spectra at different temperatures, resonance Raman spectra, and polarized light transient spectra are employed to reveal the solvent and vibrational coupling to reverse ET in transition metal complex $[(CN)_5OsCNRu(NH_3)_5]^-$. Experimental evidence that the non-totally symmetric vibrational mode is populated after reverse electron transfer is presented.

An electrical conduction study of nanocontacts between gold-grafted polythiophene film and conductive tip under different applied load using CP-AFM is presented. The importance of the adhesion force between a conducting probe and a conductive surface for characterization of electrical properties is demonstrated.

A method to measure localized charge within a molecular circuit that shows negative differential resistance *via* CP-AFM is presented. The voltage region over which conduction through Au-supported 11-ferrocenylundecanethiol self-assembled monolayer (SAM) was enhanced was found to strongly correlate with the region over which the scanning probe tip experienced

capacitive attraction to the surface. A mechanism involving two-step resonant hole transfer *via* sequential oxidation and subsequent reduction is proposed.

Single-molecule electrical conduction studies are presented to evaluate how the molecular linking unit influences the tunneling efficiency in metal-Molecule-metal (m-M-m) junctions. CP-AFM was employed to compare the molecular conduction of two π-bonded molecules, one with a single thiol linker and another with a conjugated double thiol linker at both ends of the molecules. The results demonstrating that the molecule with the conjugated double thiol linkers displays higher conduction than the non-conjugated single thiol-Au contacts are presented.

The electrical conduction studies of m-M-m junctions formed between Au-supported SAMs of 1-hexanethiol, 11-ferrocenylundecanethiol, and a Pt-coated AFM tip under different compressing forces using CP-AFM are presented. The observed junction resistance had two distinct power law scaling changes with compressing force. Different scaling regions were described through the change in the area of contact, tunneling distance and structure of the film under compression.

ACKNOWLEDGEMENTS

First and foremost, I would like to express my deepest gratitude to my research advisor, Professor Gilbert C. Walker, not only for his continual guidance and scientific insight, but also for his encouragement and unselfish support throughout my graduate study at the University of Pittsburgh. He gave me the freedom to pursue this research and his overall receptiveness to new ideas and willingness to examine them were always inspiring for me. I can never appreciate Gilbert enough for his understanding of the personal problems of his students.

I am also very grateful to Prof. David Waldeck, Prof. Peter Siska, Prof. Tomasz Kowalewski, Prof. John Yates and Prof. Eric Bourguet for serving on my committee and for their input and interest in this research.

I would like to thank my collaborators, Prof. David Waldeck, Prof. Eric Bourguet and Dr. Yufan He. The fifth chapter of my dissertation was conducted in excellent research collaboration with them. I have learned a lot during this work and our enlightening discussions.

I also thank all of the present and former members of the Prof. Walker's group for all their help and friendship. Together we made a great team. I would like to thank the University of Pittsburgh for giving me the opportunity to study here and for its financial support. I am deeply grateful to the Andrew Mellon foundation for the pre-doctoral fellowship.

I am most indebted to my wife, Larissa Stebounova, whose constant support and emphatic encouragement made this work possible. More practically, she cared for me and for our son, Vladimir Tivanski, when I could not, and still allowed me to enjoy the benefits of fatherhood. I

hope they will forgive me this selfishness. I would like to express my deepest gratitude to my parents, Viktor and Ludmila Tivanski, for being my first teachers and always believing in me.

I dedicate this thesis to my adorable wife, Larissa for all her love, care and patience, and to my son, Vladimir, who always smiles my fatigue away.

TABLE OF CONTENTS

LIST OF TABLES

LIST OF FIGURES

1. INTRODUCTION

In the past half century there have been extraordinary advances in our understanding of microscopic electron transfer (ET) reactions in solution. Contemporary lasers have advanced studies of chemical dynamics to a femtosecond time scale. The second chapter of this thesis describes ultrafast infrared spectroscopy studies of intramolecular ET in the mixed-valence transition metal complex $[(CN)_5OsCNRu(NH_3)_5]^-$. The objective is to understand how solute vibrational excitation couples to ET, and how the solvent couples to those vibrational modes changes after ET. Static optical metal-metal charge transfer spectra, infrared absorption (IR) spectra at different temperatures, resonance Raman spectra, and polarized light transient spectra in formamide (FA) and deuterium oxide (D_2O) solutions are described. To interpret these spectra, we have used group theory to deduce the IR and Raman active modes. We have combined static spectroscopy and polarized light pulse anisotropy data to assign the CN stretching modes. We observe that, counter to the common assumption, a non-totally symmetric mode is coupled to reverse electron transfer in transition metal mixed valence complexes in both solutions. We believe that spin-orbital coupling plays an important role. A simulation of the spectral dynamics in FA and D_2O solutions is presented using a kinetic model for vibrational excitation and relaxation. The simulation includes the effect of solvent heating through coupling a low-frequency mode to a medium-frequency oscillator. The vibrational relaxation times of trans CN are obtained from the spectral fits and show faster vibration relaxation in D_2O than FA, reflecting an overlap of the IR absorption spectra of the solvent and the CN vibrations.

While molecular level ET processes are fairly understood, characterization of processes on the nanoscale (1 to 100 nm) is at its beginning. Understanding nanoscale charge transfer is important to possible applications for molecular electronics. The development of many of these applications requires reliable methods to measure conductive properties at the nanoscale. Different approaches have been attempted to investigate such properties of metal-molecule-metal junctions, including scanning probe microscopy. In this thesis studies of thin organic film interfaces by conducting probe atomic force microscopy (CP-AFM) are reported. The capability of CP-AFM to measure precisely the contact forces between the probe and the sample surface allows independent and simultaneous measurement of the current and the contact force between the probe and the sample.

The third chapter describes studies of the conductive and adhesive properties of a polythiophene monolayer coupled between two gold electrodes using CP-AFM in an insulating organic solvent. We have shown theoretical and experimental results of how the electrostatic part of the adhesion force depends on the applied external bias. We observed an increase in conductivity with increasing applied pressure. Our results showed that neglecting the adhesion forces contribution to the overall interaction force between conductive probe and the sample can provide significantly inaccurate estimates of the pressure between the conducting tip and the sample, and thus conductive properties of the nanoscale devices should be interpreted in light of this additional adhesion force.

The fourth chapter describes mechanical and electrical conduction measurements of electroactive metal-Molecule-metal (m-M-m) junctions formed between Au-supported self-assembled monolayers (SAMs) of 11-ferrocenylundecanethiol ($FcC_{11}SH$) and a Pt-coated AFM tip using CP-AFM in bicyclohexyl solvent. The objective is to correlate the measured currents and the

bias-dependent adhesion force under different applied biases between the conductive AFM probe and the molecular film.

Simultaneous and independent measurements of currents and bias-dependent adhesion forces under different applied tip biases between the conductive AFM probe and the $FcC_{11}SH$ SAMs are presented. These measurements revealed reversible peak-shaped current-voltage (*I-V*) characteristics and correlated maxima in the potential-dependent adhesion force. A mechanism involving two-step resonant hole transfer through the occupied molecular orbitals (MOs) of ferrocene-end groups *via* sequential oxidation and subsequent reduction, where a hole is trapped by the phonon relaxation, is presented to explain the observed current-force correlation. Additionally, electric force measurements along with theoretical modeling both in and out of contact with a nonelectroactive 1-octanethiol (C_8SH) SAM are also presented.

Single-molecule electrical conduction studies are described in the chapter five to evaluate how the molecular linking unit influences the tunneling efficiency in m-M-m junctions. CP-AFM was employed to compare the molecular conduction of two π-bonded molecules, one with a single thiol linker and another with a conjugated double thiol linker at both ends of the molecules. The resulting finding is that the efficiency of charge transport through π-bonded molecules forming m-M-m junctions with thiol linking units between metals and the molecule can be improved by the use of conjugated double thiol linkers at both ends of the molecule.

The sixth chapter describes detailed measurements of electrical conduction using CP-AFM for two nanojunctions formed between a Pt-coated AFM tip and a Au-supported 1-hexanethiol and ferrocenyl-1-undecanethiol SAMs under different compressing forces with the objective to correlate electrical conduction through m-M-m junctions with mechanical and structural properties of the film. Observed junction resistances showed two distinct power laws scaling

changes with compressing interaction force for both SAMs. The elastic model for the change in contact area and tunneling gap between the AFM tip and the sample, including the different molecular structures of the films is presented to quantitatively describe these regions.

2. VIBRATIONAL MODE COUPLING TO ULTRAFAST ELECTRON TRANSFER IN $[(CN)_5OsCNRu(NH_3)_5]^-$ STUDIED BY FEMTOSECOND INFRARED SPECTROSCOPY [§]

We report studies of the coupling of vibrational excitations to photoinduced electron transfer in a mixed-valence transition metal complex $[(CN)_5OsCNRu(NH_3)_5]^-$. Static metal-metal charge transfer (MMCT) spectra, infrared (IR) absorption spectra at different temperatures, resonance Raman spectra, and polarized light transient spectra were taken to reveal the solvent and vibrational coupling to reverse electron transfer. The measured reverse electron transfer rates are greater than 3×10^{12} s^{-1}. We observe excitations in the non-totally symmetric vibrational mode accompanying the reverse electron transfer process in both formamide (FA) and deuterium oxide (D_2O) solutions. A simulation of the spectral dynamics in FA and D_2O solutions is presented using a kinetic model for vibrational excitation and relaxation. The simulation includes the effect of solvent heating through coupling a low-frequency mode to a medium-frequency oscillator. The vibrational relaxation times of trans CN obtained from the spectral fits show faster vibration relaxation in D_2O than FA, reflecting an overlap of the IR absorption spectra of the solvent and the CN vibrations.

[§] This work has been originally published as Tivanski, A. V.; Wang, C.; Walker, G. C. *J. Phys. Chem. A* **2003**, *107*, 9051-9058.

2.1. Introduction

Considerable progress has been made in recent years both in experimental and theoretical aspects of understanding electron transfer (ET) reactions in solution.[1-39] The coupling of vibrational and solvation dynamics to ET has been of particular interest. In these studies, mixed-valence transition-metal dimers are popular for investigating the dynamics of ultrafast electron transfer. Understanding the microscopic details of these reactions has been the object of recent work by our group and others.[40-45]

Our goal is to understand how solute vibrational excitation to couples ET, and how the solvent couples to those vibrational modes changes after ET. In recent years researchers have related the ET rates with resonance Raman intensities and charge transfer absorption profiles.[46-48] There is an assumption in this approach that only totally symmetric modes can couple to reverse ET. Thus, it is worthwhile examining if this assumption is valid in mixed-valence transition metal dimers.

The chemical system reported upon here is $[(CN)_5OsCNRu(NH_3)_5]^-$ (OsRu), which provides a well-defined environment in which to study the ET reaction. Optical absorption corresponds to direct electron transfer from Os to Ru. Radiationless decay from the electronic excited state(s) to the ground state results in reverse electron transfer. We are interested in studying the response of CN vibrations after reverse electron transfer. The metal-metal charge transfer (MMCT) processes can be represented as

$$[(CN)_5\,Os^{II}\,CN\,Ru^{III}\,(NH_3)_5]^- \underset{\text{reverse ET}}{\overset{h\upsilon}{\rightleftharpoons}} [(CN)_5\,Os^{III}\,CN\,Ru^{II}\,(NH_3)_5]^-.$$

We utilize pulsed 800 nm light to excite the molecule to electronic excited state(s) (direct ET) and pulsed infrared light to probe the CN vibrational absorption after reverse ET in both formamide (FA) and deuterium oxide (D_2O) solutions. We combine the static spectroscopy and

anisotropy data along with group theory analysis to assign the observed transient absorption features. Finally, we provide a simulation of transient spectra of OsRu in formamide and deuterium oxide in which we consider the effects of vibrational excitation and relaxation. In the simulation of transient spectra of OsRu in deuterium oxide we consider the time-dependent frequency shift of the low frequency mode caused by the coupling between low and high frequency modes.

2.2. Experimental methods

The apparatus and experimental method have been described in detail elsewhere.[49] Briefly, the time-resolved experiments were performed using femtosecond 800 nm pump pulses and mid-IR probe pulses. The 800 nm pump pulses (120 fs) are used to initiate the direct electron transfer, and the mid-infrared probe pulses (200 fs) are used to detect the vibrational absorption of the CN stretch modes after reverse electron transfer. Thus, the signal recorded is the change of IR absorbance in the sample induced by pump pulses. Time resolved infrared spectra and transient kinetic signals are obtained by varying the relative arrival time of pump and probe pulses at the sample and detecting transmitted IR pulses through a monochromator at a 10 element HgCdTe array detector. The spectral resolution of the IR probe light is 7 cm^{-1}. The 800 nm pump light is provided by a Ti:sapphire regenerative amplifier operated at 1.15 kHz. The mid-infrared light is generated using optical parametric amplifier (OPA) and difference frequency generation (DFG) techniques. A β-barium borate (BBO) OPA is pumped by 800 nm pulses to generate near-IR pulses (signal and idler). Tunable mid-IR is subsequently generated in a $AgGaS_2$ crystal (1 mm path length, 39° cut for type II phase-matching) by mixing signal and idler pulses *via* difference

frequency generation. The OPA is operated in a double-pass configuration. The first pass of the OPA in the BBO crystal (3 mm path length, 27° cut for type II phase-matching) is pumped with 800 nm light and seeded with white light continuum which is generated by focusing a small fraction (1-5 μJ) of fundamental 800 nm light into a 4 mm thick sapphire plate. After the second pass through the BBO crystal, the signal and idler are focused into $AgGaS_2$ crystal for difference frequency generation. Mid-IR tunable from 3-8 μm with one microjoule pulse energy and 200 fs pulse width (FWHM) can be obtained.

Formamide (FA) and N-methyl formamide (NMF) were purchased from Aldrich and used without further purification. Deuterium oxide (D_2O) was obtained from Cambridge Isotopes. For static IR absorption and resonance Raman measurements, the concentrations of OsRu were 10^{-3} M in D_2O, FA and NMF. These measurements were performed using FTIR and FT-Raman spectrometers (Nicolet 800). For Raman measurements, the excitation wavelength was 1064 nm obtained from a YAG laser; the laser power for these experiments was 350 - 400 mW. The sample was placed in a 4 mm diameter NMR tube and stirred by a magnetic stirrer to avoid localized heating of the sample by the YAG laser light.

For transient absorbance measurements, the sample solution was placed in a spinning cell with thin CaF_2 windows which provided a fresh sample volume for every laser shot (1.15 kHz). The concentrations of OsRu were 0.02 M in D_2O and 0.008 M in FA. The path length was 0.2 mm for D_2O experiments and 0.5 mm for FA experiments. The pump (800 nm) and probe (mid-IR) beams were combined and focused into the sample collinearly using a dichroic mirror. The pump and probe beams were focused to spot sizes of 0.2 and 0.15 mm in diameter, respectively. The pump energy was 3 μJ/pulse. A zero-order half-wave plate was placed in the pump beam to provide for polarization dependent measurements.

2.3. Results

Figure 2-1 shows the metal-metal charge transfer (MMCT) absorption spectra of OsRu in D_2O and formamide (FA) solvents.

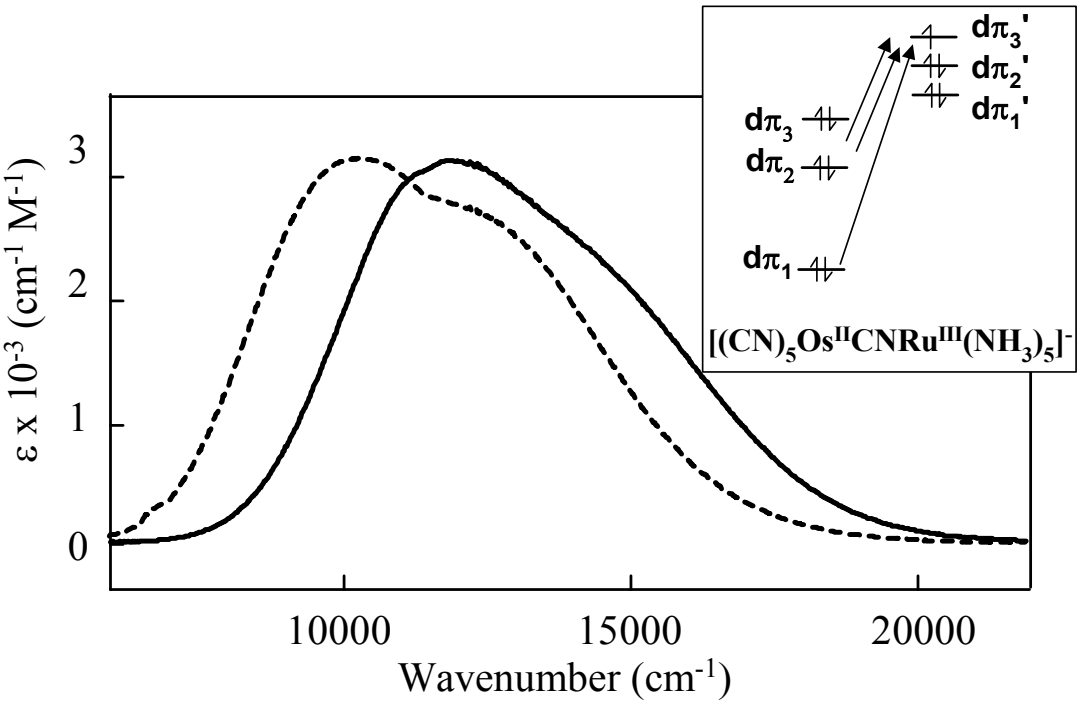

Figure 2-1 Metal-metal charge transfer absorption spectra of OsRu in D_2O (solid line) and formamide (dotted line). The inset shows the direct electron transfer process.

The absorption bands are strongly solvent broadened. In this complex the available donor orbitals derive from the nominally degenerate $5d\pi$ orbitals of the Os center. If we define the *z*-axis as lying along the two metal centers and bridging CN, then two of these orbitals (d_{xz} and d_{yz}) are directed on the z axis and the third (d_{xy}) is orthogonal. In O_h symmetry, the three $d\pi$ orbitals of the metal are degenerate. Due to spin-orbit coupling and ligand-field asymmetry, they are

partially split in symmetries lower than O_h into the nondegenerate $d\pi_1$ orbital and a degenerate pair of orbitals ($d\pi_2$ and $d\pi_3$). The spin-orbit (SO) coupling is about 3200 cm^{-1} for osmium and 1100 cm^{-1} for ruthenium.[50,51] The band width in OsRu is 2100 cm^{-1} broader than in $[(CN)_5 Fe^{III}CNRu^{II}(NH_3)_5]^-$ (FeRu) which is expected to have similar nuclear reorganization energy but 2000 cm^{-1} less SO coupling. The absorption measurements make possible the evaluation of nonadiabatic electronic coupling energies, H_{ab}. We have estimated the electron coupling between $Os^{II}Ru^{III}$ and $Os^{III}Ru^{II}$ states using the Hush-Mulliken analysis:[50,58]

$$H_{ab} = ((4.2 \times 10^{-4})\, \varepsilon_{max}\, \Delta\nu_{FWHM}\, \nu_{max}/d^2)^{1/2} \qquad (2.1)$$

Here ε_{max} is the maximum of extinction coefficient, $\Delta\nu_{FWHM}$ is the full width at half maximum (FWHM) of the band, and ν_{max} is the center frequency of the band. The distance between the metal centers d is taken to be 5 angstroms. The properties of the MMCT band are summarized in TABLE 2-1. We conclude that the MMCT band's peak frequency, width and H_{ab} are strongly solvent coupled.

TABLE 2-1 Properties of the MMCT Absorption Band of OsRu in Solution

Solvent	ν_{max} (cm^{-1})	$\Delta\nu_{FWHM}$ (cm^{-1})	ε_{max} (M^{-1} cm^{-1})	H_{ab} (cm^{-1})
D_2O	11750	8960	3010	2300
FA	10150	7380	3020	1950

Figure 2-2 shows the static infrared absorption spectra of OsRu in the CN stretch region for D_2O and formamide solvents. There are two main features in the infrared absorption spectra. There

is a strong band at around 2050 cm^{-1} and a strong wide band at around 2000 cm^{-1} which is strongly influenced by the solvent. Two weak bands are seen at ca. 2110 cm^{-1} and 2070 cm^{-1}, respectively. The characteristics of the vibrational absorption bands in CN stretch region are summarized in TABLE 2-2.

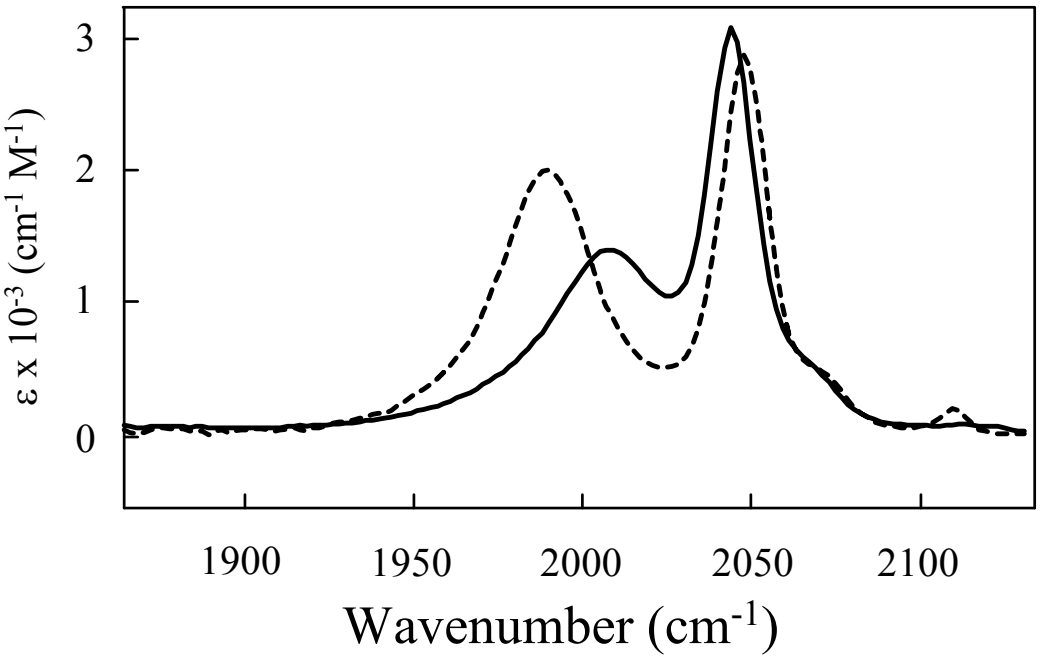

Figure 2-2 Infrared absorption spectra of OsRu in D_2O (solid line) and formamide (dotted line) in CN stretch region.

TABLE 2-2 Properties of CN Stretch Infrared Absorption Bands of OsRu in Solution

Solvent	Mode	ν_{max} (cm^{-1})	$\Delta\nu_{FWHM}$ (cm^{-1})	ε_{max} (M^{-1} cm^{-1})
D_2O	*bridge* CN	2115	9 ± 1	30
D_2O	*cis* CN	2045	16 ± 0.04	2760
D_2O	*trans* CN	2010	45 ± 0.2	1400
FA	*bridge* CN	2110	10 ± 0.4	130
FA	*cis* CN	2050	17 ± 0.03	2800
FA	*trans* CN	1990	34 ± 0.07	1990

Figure 2-3 shows the resonance Raman spectra of OsRu in CN stretch region in D_2O and formamide solvents. There is a strong band near 2110 cm^{-1} and one wide band at around 2000 cm^{-1}. No Raman band is seen around 2050 cm^{-1}, in contrast to the infrared absorption spectra.

Figure 2-4 shows the time-resolved infrared difference spectra of OsRu in FA solvent with pump polarization perpendicular and parallel to the probe polarization respectively. Negative -ΔOD features correspond to the loss of ground vibrational state absorbance due to optical excitation, and positive ΔOD features correspond to increase of ground vibrational state absorbance or new vibrational absorption created as a result of excitation by the optical pump pulses (800 nm). At positive times, there are bleaches of ground state absorbance at ca. 2050 cm^{-1} and 2000 cm^{-1}, respectively. The new absorption is seen at ca. 2100 cm^{-1}, 2030 cm^{-1} and 1975 cm^{-1}.

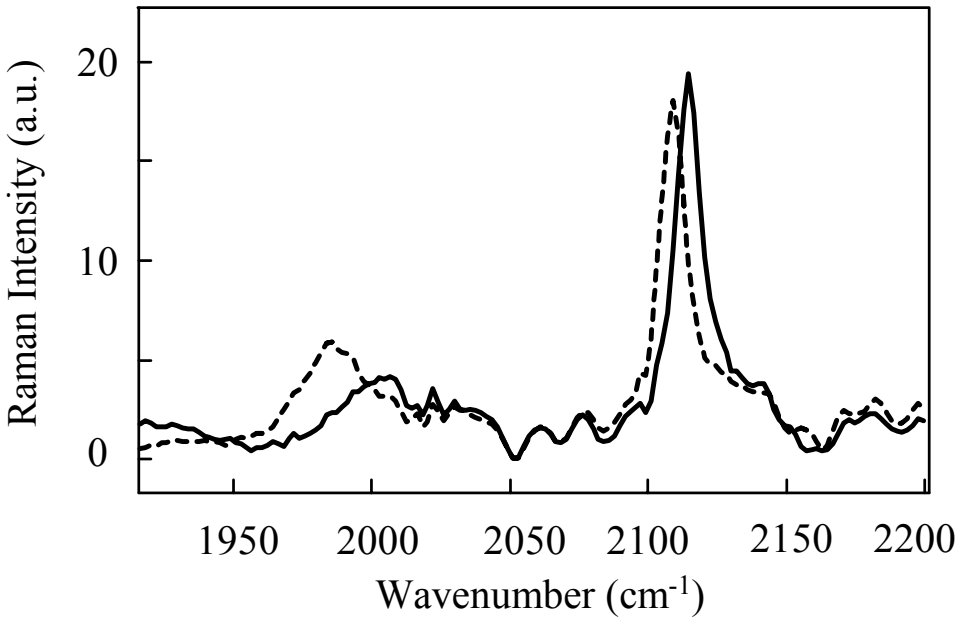

Figure 2-3 Resonance Raman spectra of OsRu in D_2O (solid line) and formamide (dotted line) in CN stretch region. The excitation wavelength is 1064 nm.

Figure 2-5 shows the time-resolved infrared difference spectra of OsRu in deuterated water solvent with pump polarization perpendicular and parallel to the probe polarization respectively. At positive times, there are bleaches of ground state absorbance at ca. 2050 cm^{-1} and 2000 cm^{-1}, respectively. The new absorption is seen at ca. 2030 cm^{-1} and 1995 cm^{-1}.

Figure 2-6 and Figure 2-7 show the time-resolved visible difference spectra of OsRu in D_2O solvent with pump polarization perpendicular and parallel to the probe polarization, respectively.

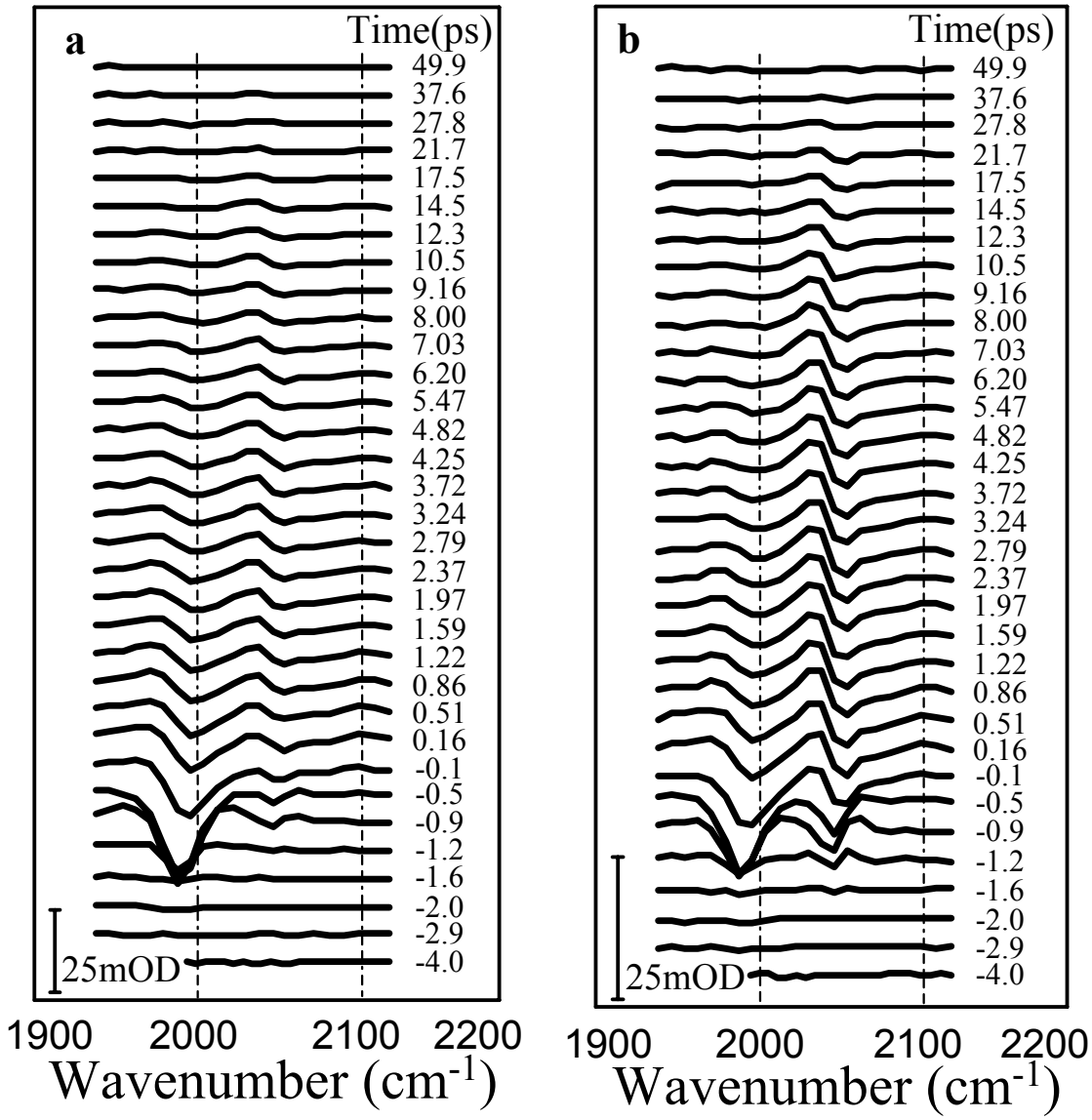

Figure 2-4 Transient infrared spectra of OsRu in formamide solvent. a. The relative polarization of pump (800 nm) and probe (mid-IR) pulses is parallel. b. The relative polarization of pump (800 nm) and probe (mid-IR) pulses is perpendicular.

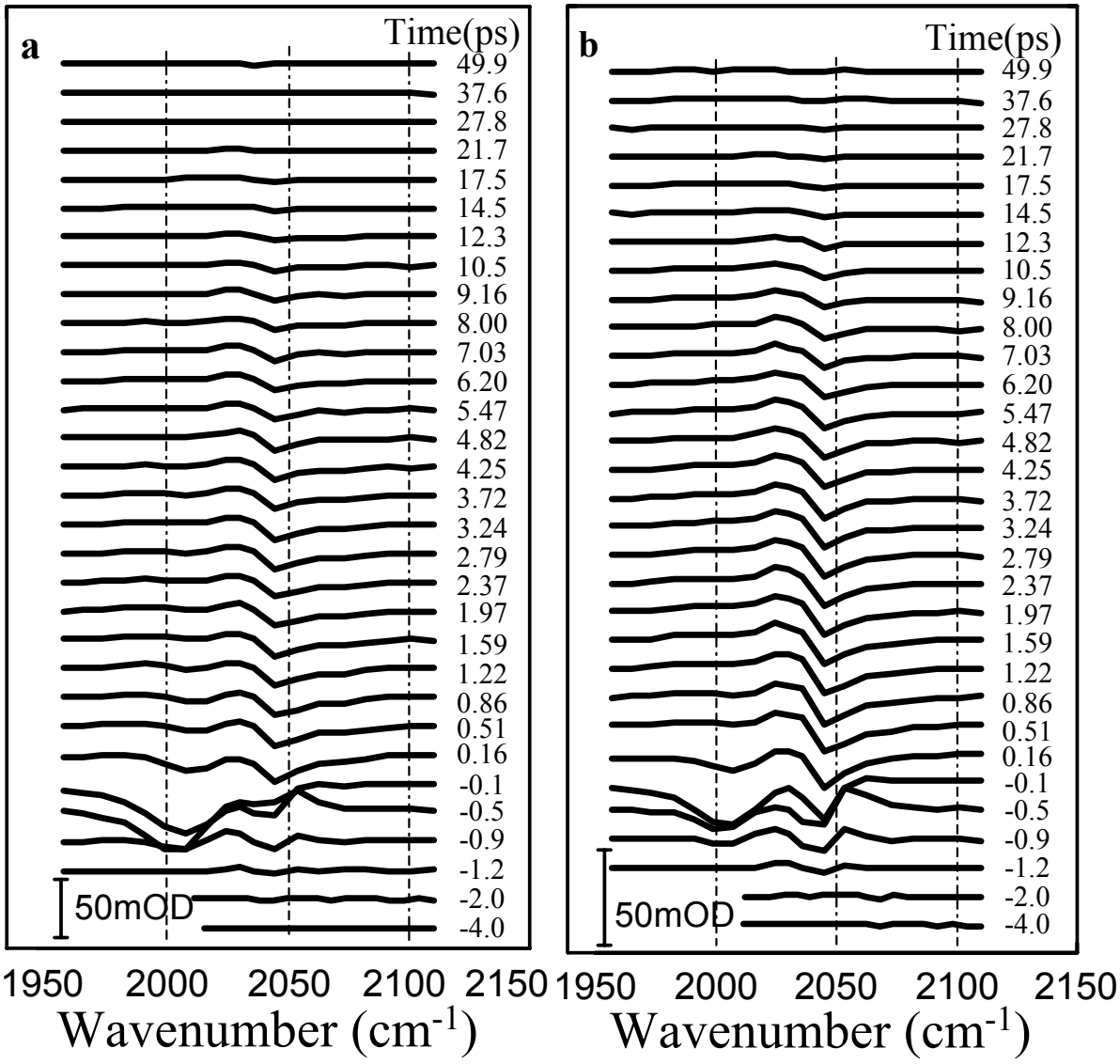

Figure 2-5 Transient infrared spectra of OsRu in deuterium water solvent. a. The relative polarization of pump (800 nm) and probe (mid-IR) pulses is parallel. b. The relative polarization of pump (800 nm) and probe (mid-IR) pulses is perpendicular.

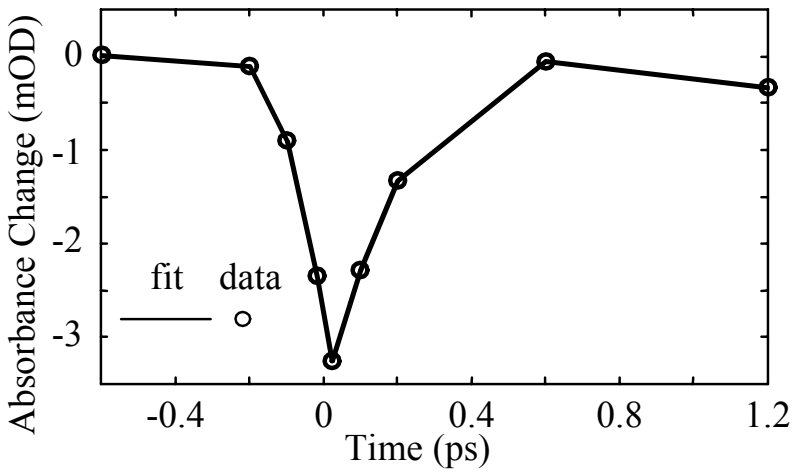

Figure 2-6 Transient visible difference spectra of OsRu in D_2O solvent with pump polarization (800 nm) perpendicular to the probe polarization (800 nm). The fit is based on the direct step-function extrapolation of the pulse profile. Assuming a one exponential decay process, we obtain a relaxation time of 180 fs.

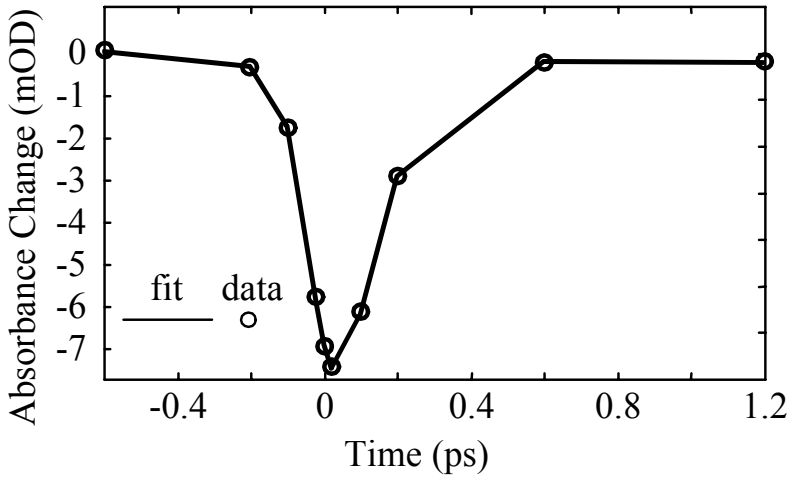

Figure 2-7 Transient visible difference spectra of OsRu in D_2O solvent with pump polarization (800 nm) parallel to the probe polarization (800 nm). The fit is based on the direct step-function extrapolation of the pulse profile. Assuming a one exponential decay process, we obtain a relaxation time of 140 fs.

2.4. Discussion

Based on the spin-orbit (SO) states picture (shown in the inset of Figure 2-1) there are two overlapping intervalence transitions. The lower energy, high intensity transition band is the optical intervalence electron transfer band from the degenerate pair of donor orbitals ($d\pi_2$ and $d\pi_3$). The high energy, lower intensity transition band is an intervalence electron transfer band from the single donor orbital ($d\pi_1$).

In order to fit the static absorption spectra, we will use a lineshape that includes a classical and a high frequency quantal degree of freedom. The form of the lineshape is therefore a sum of Gaussians in a Frank-Condon (FC) distribution (vibronic shape factor).

Variations in Raman intensity I among the modes can be connected to unitless normal-coordinate distortions Δ:

$$\frac{I_1}{I_2} = \frac{\omega_1^2 \Delta_1^2}{\omega_2^2 \Delta_2^2} \tag{2.2}$$

The magnitudes of Δ's can in principle be determined from the width of the absorption band by using Equation 3[52,53]

$$2\sigma^2 = \sum_k \Delta_k^2 (\nu_k)^2 = \sum_k \Delta_k^2 (\omega_k / 2\pi)^2 \tag{2.3}$$

where ω_k is 2π times the vibrational frequency ν_k and $2\sigma^2$ is the square of the absorption band at 1/2 of the height. From the normal coordinate or bond distortion data, individual contribution χ_i to the vibrational reorganization energy can be calculated:

$$\chi_i = \frac{1}{2} \Delta_i^2 \nu_i \tag{2.4}$$

Based on the resonance Raman spectra of OsRu in CN stretch region in D_2O and formamide solvents (shown in Figure 2-3) we can assign Raman intensities and frequencies for different modes. Since $2\sigma^2 = (\Delta\nu_{1/2})^2$, where $\Delta\nu_{1/2}$ is FWHM of the absorption spectra, we can calculate σ for different solvents. Using this data together with Equations 2.2-2.4, we can calculate normal-coordinate distortions and vibrational reorganization energy for different modes in different solvents. The results are summarized in TABLE 2-3. We note the metal-carbon stretch modes might be expected to show activity;[40] within the modest signal-to-noise ratio in the resonance Raman spectra, no such activity was observed in the expected region of the spectrum.

TABLE 2-3 Properties of Resonance Raman Bands of OsRu in Solutions and Calculated Normal Mode Distortion Δ with Vibrational Reorganization Energy χ_I for the Different Modes

Solvent	Mode	ν_{max} (cm^{-1})	$\Delta\nu_{FWHM}$ (cm^{-1})	I (a.u.)	Δ	χ_I (cm^{-1})
D_2O	*bridge* CN	2115	15	19	2.5	1400
D_2O	*trans* CN	2010	55	4	1.3	330
FA	*bridge* CN	2110	15	17	2.6	1510
FA	*trans* CN	1990	40	6	1.6	570

In order to fit the static absorption spectra, we use a lineshape that includes a classical and one high frequency quantal degree of freedom. The form of the lineshape is therefore a sum of Gaussians in a Frank-Condon distribution (vibronic shape factor). The nuclear Frank-Condon

factors for connecting n=0 of the ground state and the nth vibrational state for the excited state are

$$\left|\langle 0|n\rangle\right|^2 = \frac{S^n}{n!}\exp(-S)$$

where the electron-vibrational coupling strength is $S = \frac{\chi_i}{\nu_i}$.

Since there are two modes (*trans* CN and *bridge* CN) and assuming that the absorption spectra consist of two bands, then the overall lineshape becomes

$$F(\nu) \propto \sum_i \sum_m \sum_n \left|\langle 0|n\rangle\right|^2 \left|\langle 0|m\rangle\right|^2 \exp-\left[\frac{\left(\Delta G^0{}_{i,m,n} + \lambda_{cl} - h\nu\right)^2}{4\lambda_{cl}k_B T}\right]$$

where the modified free energy difference, $\Delta G^0{}_i$, i=1,2 is $\Delta G^0_{i,n,m} = \Delta G^0_i + nh\nu_{trans} + mh\nu_{bridge}$ and λ_{cl} is the classical reorganization energy. In the current procedure, we will neglect terms $\left|\langle 0|k\rangle\right|^2$ for k=3,4,… since these terms becomes negligible; we will only use k =0,1,2.

Figure 2-8 and Figure 2-9 show a fit of the absorption spectra of OsRu in D_2O and in FA with two bands, 1:2 amplitude ratio and the same classical reorganization energy λ_{cl} (proportional to the square of FWHM for each band). From the fitting one obtains for D_2O: $\Delta G_0{}^{(1)}$ =12550 cm^{-1}, $\Delta G_0{}^{(2)}$ =8730 cm^{-1}, λ_{cl} = 2220 cm^{-1} and for FA: $\Delta G_0{}^{(1)}$ =9750 cm^{-1}, $\Delta G_0{}^{(2)}$ =7610 cm^{-1}, λ_{cl} = 1670 cm^{-1}. These results are consistent with higher dielectric constant of D_2O than of FA.

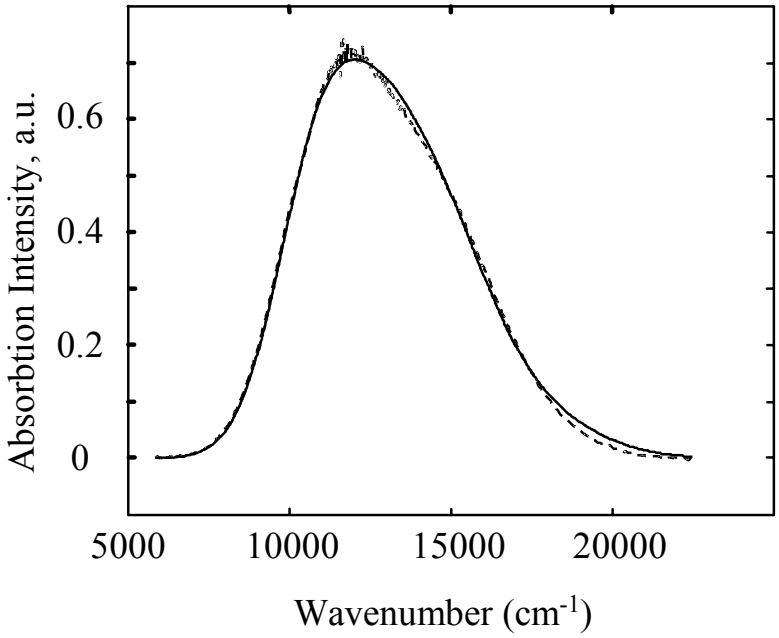

Figure 2-8 A fit of the OsRu absorption spectra in D_2O with a 1:2 amplitude ratio for the relative cross sections of the two characteristic spin orbit transitions. The dashed line represents the data while the solid line is the fit to the data.

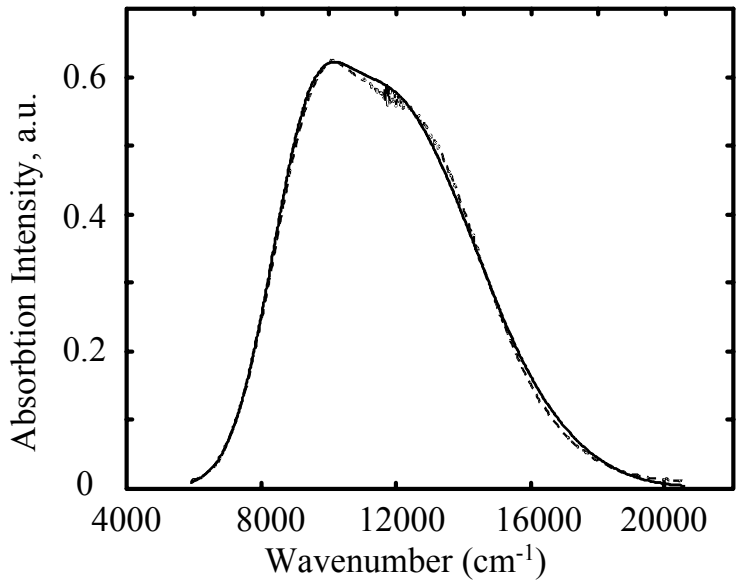

Figure 2-9 A fit of the OsRu absorption spectra in formamide with 1:2 amplitude ratio for the relative cross sections of the two characteristic spin orbit transitions. The dashed line represents the data while the solid line is the fit to the data.

Figure 2-10 shows a simplified picture of the transition metal complex and the CN vibrational modes. From group theory, the total stretching CN normal modes include three A_1, one B_1, and two E modes of $(CN)_5OsXY$ in C_{4v} symmetry, where XY represents the bridging CN group. Or we can write $\Gamma_{stretch} = 3\,A_1 + B_1 + E$. IR active modes are A_1 and E, and Raman active modes are A_1 and B_1 in these stretching modes.

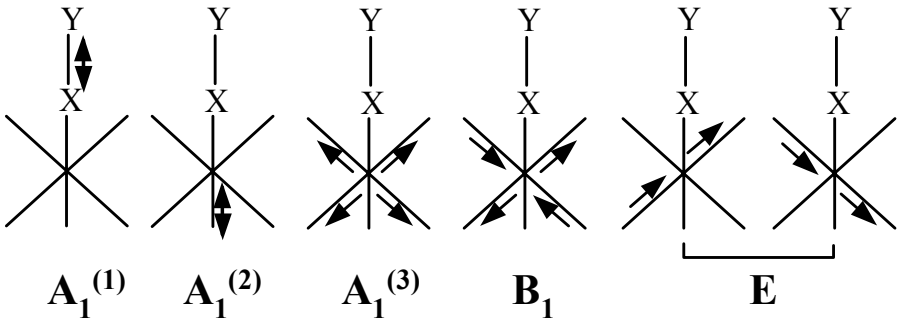

Figure 2-10 Vibrational normal modes of CN vibrations based on a simplified local C_{4v} symmetry of an OsRu molecule.

Through anisotropy measurements (shown in Figure 2-4 and Figure 2-5), one can obtain the ensemble-averaged angles between electronic and vibrational transition moments using Equations 5 and 6. The anisotropy is calculated from the formula

$$r(t) = \frac{\left(I_{II} - I_{\perp}\right)}{\left(I_{II} + 2I_{\perp}\right)} \tag{2.5}$$

where I_{II} and $I_{\perp}$ are the absorption intensity changes for the probe IR beam polarized parallel and perpendicular to the optical excitation pulse, respectively.

The angle between the electronic transition moment and the vibrational transition moment can be calculated as

$$<\cos^2(\theta(t))> = (1 + 5\, r\,(t))/3 \qquad (2.6)$$

From this measurement, the bands at 2050 cm^{-1} and 2030 cm^{-1} are found to be close to perpendicular to the electronic transition moment, and the bands at 2000cm^{-1} and 1970 cm^{-1} are close to parallel to the electronic transition moment. The anisotropy values are listed in TABLE 2-4.

TABLE 2-4 Anisotropy Values of CN Modes of OsRu in Formamide

Frequency (cm^{-1})	R / θ	Mode assignment
2000 cm^{-1}	0.26 ± 0.05 / 29°± 6°	*trans* CN
2050 cm^{-1}	-0.2 ± 0.04 / 90°± 15°	*cis* CN
2030 cm^{-1}	-0.2 ± 0.04 / 90°± 15°	v =1 → v = 2 *cis* CN
1970 cm^{-1}	0.16 ± 0.05 / 39°± 5°	v =1 → v = 2 *trans* CN
2080 cm^{-1}	0.05 ± 0.02 / 50°± 10°	
2100 cm^{-1}	0.05 ± 0.02 / 50°± 10°	

Hester and Swanson found that the highest frequency CN stretch mode in binuclear complexes was the bridging CN mode.[54,55] Thus the 2110 cm^{-1} mode is assigned here as the *bridge* CN ($A_1^{(1)}$) mode. Considering that the 2000 cm^{-1} stretch mode is close to parallel to the electronic transition moment, we can assign the mode at 2000 cm^{-1} as the *trans* CN ($A_1^{(2)}$) mode. Because the 2050 cm^{-1} stretch mode is perpendicular to the electronic transition moment and it is IR active, it must be $A_1^{(3)}$ or E. Since the $A_1^{(3)}$ mode is the totally symmetric stretching of the *cis*

CN group, the *E* mode should have greater IR intensity. Therefore the 2050 cm^{-1} band is assigned here as the *cis* CN (*E*). Here *cis* means *cis* to the bridge and *trans* means *trans* to the bridge. Considering anharmonicity, the absorption at 2030 cm^{-1} is assigned here as v=1 → v=2 absorption of *cis* CN. Similarly, the absorption at 1975 cm^{-1} is assigned as the v=1 → v=2 absorption of *trans* CN.

2.5. Simulation of the Observed Dynamics

We have developed in a previous publication[41] an analytical method to simulate the observed spectral dynamics. In this simulation we assume that the vibrational state distribution is generated in the radiationless decay process. The simulation considers the cross section and population dynamics of the *cis*, *trans*, and *bridge* modes after electron transfer. The following equations were used to calculate the vibrational populations:

$$dF_{j,i}(t)/dt = K_{j,i+1}F_{j,i+1}(t) - K_{j,i}F_{j,i}(t) \tag{2.7}$$

$$\sum_{i=0}^{k} \mathrm{F_{j,i}(t)} = \sum_{i=0}^{k} \mathrm{F_{j,i}(0)} \tag{2.8}$$

$$K_{j,k+1} = K_{j,0} = 0 \tag{2.9}$$

where *i* (*i* = *k, k-1*, …, 0) denotes vibrational states and *j* (*j* = 1,2) corresponds to *trans* and *cis* modes; $K_{j,i}$ is the rate constant. $F_{j,i}(t)$ is the population of vibrational state *i* at time *t* and $F_{j,i}(0)$ is the initial population of state *i*. From the harmonic oscillator approximation, $K_{j,i} = i\,K_{j,1}$ and this can be used to estimate the vibrational state dependent cross section.

Including the effects of vibrational anharmonicity[56] and a Gaussian lineshape for each vibrational resonance, the transient ΔOD signal (after reverse ET) is

$$\Delta A(t,\nu)=\sum_{i=0}^{k} c_1(i+1)B_{1,i}(t,\nu)\left[F_{1,i}(t)-F_{1,i+1}(t)\right]-c_1B'_{1,0}(\nu)+$$
$$\sum_{i=0}^{k} c_2(i+1)B_{2,i}(t,\nu)\left[F_{2,i}(t)-F_{2,i+1}(t)\right]-c_2B'_{2,0}(\nu)+c_3B_{3,0}(\nu)F_{3,0}(t)$$
$$c_4B_{4,0}(\nu)F_{4,0}(t). \qquad (2.10)$$

Here ΔA is the induced absorbance change and c_1, c_2, c_3 and c_4 are cross section scaling factors. $B_{1,i}(t, \nu)$ and $B_{2,i}(t, \nu)$ are the Gaussian lineshape functions with time dependent amplitudes (i = 0-k, corresponding to different vibrational states). $B'_{1,0}(\nu)$, $B'_{2,0}(\nu)$, $B_{3,0}(\nu)$ and $B_{4,0}(\nu)$ are the Gaussian lineshape functions of the modes in the ground vibrational state. $F_{1,i}(t)$ and $F_{2,i}(t)$ are the populations of vibrational state i at time t for modes 1 and 2. $F_{3,0}(t)$ and $F_{4,0}(t)$ have the form of an exponential decay. The Gaussian lineshape function is

$$B_{j,i}(t, \nu) = (1 + f\exp(-t/\tau))\exp(-(\nu - \nu_{j,0})^2/w_{j,0}^2) \qquad (2.11)$$

where $\nu_{j,0}$ is the band center frequency which might be time-dependent as will be shown below, and $w_{j,0}$ is its width. f is a parameter that accounts for the temperature dependence of the cross section; it is zero for the unpumped state. τ is the time constant for the time dependence of the cross section due to solvent cooling.

For these high frequency vibration modes, the Boltzman factors place essentially all of the population in the v = 0 state (the ground state) at negative times. At positive times, non-equilibrium vibrational populations are generated by optical excitation and reverse electron transfer. The $B_{j,i}(t, \nu)\, F_{j,i}(t)$ term represents the stimulated absorption from vibrational state i, and the $B_{j,i}(t, \nu)\, F_{j,i+1}(t)$ term represents stimulated emission from state $(i+1)$ to i. The $B_{3,0}(\nu)$

$F_{3,0}(t)$ term corresponds to the absorption due to the cross section increase as the temperature increases. The $(i + 1)$ term in Equation 2.10 comes from the vibrational excited state dependence of the vibrational transition cross section; within the harmonic oscillator approximation; μ_i^2 is proportional to $(i + 1)$ where μ^2 is proportional to the absorption cross section. The results show that vibrational levels v=0, v=1, and v=2 of *cis* and *trans* CN are populated after reverse ET. The fitted spectra for OsRu in FA are shown in Figure 2-11. The fitted parameters are listed in TABLE 2-5.

The fitted initial populations show vibrational excitation of IR active modes that are not present in the resonance Raman data in TABLE 2-3. We do not know the mechanism that leads to the observed distribution. The initially prepared electronic state has excitation in the totally symmetric modes of the system. Energy could be deposited in the IR active modes *via* evolution of the geometry of the molecule in the excited state or a vibration of suitable symmetry could couple the totally symmetric mode with the IR active mode in a fast relaxation process.[57] We note that the spin orbit states of the t_{2g} manifold are quite close, and relaxation within them may occur on the time scale of the observed dynamics.

The time-resolved visible difference spectra of the OsRu in D_2O solvent with pump polarization perpendicular and parallel to the probe polarization respectively were collected (See Figure 2-6 and Figure 2-7). The shown fit was based on the direct step-function extrapolation of the pulse profile. Assuming a single exponential decay, the relaxation time is 180 fs for pump pulse polarization perpendicular to the probe pulse polarization and 140 fs for pump pulse polarization parallel to the probe pulse polarization. Other researchers have found that electronic relaxation time within spin-orbit states in a similar transition metal complex is on the time scale of 100 fs.[58]

Additional experiments that probe electronic transitions between spin-orbit states of Os^{III} should be done in the future to better address the role of spin orbit relaxation.

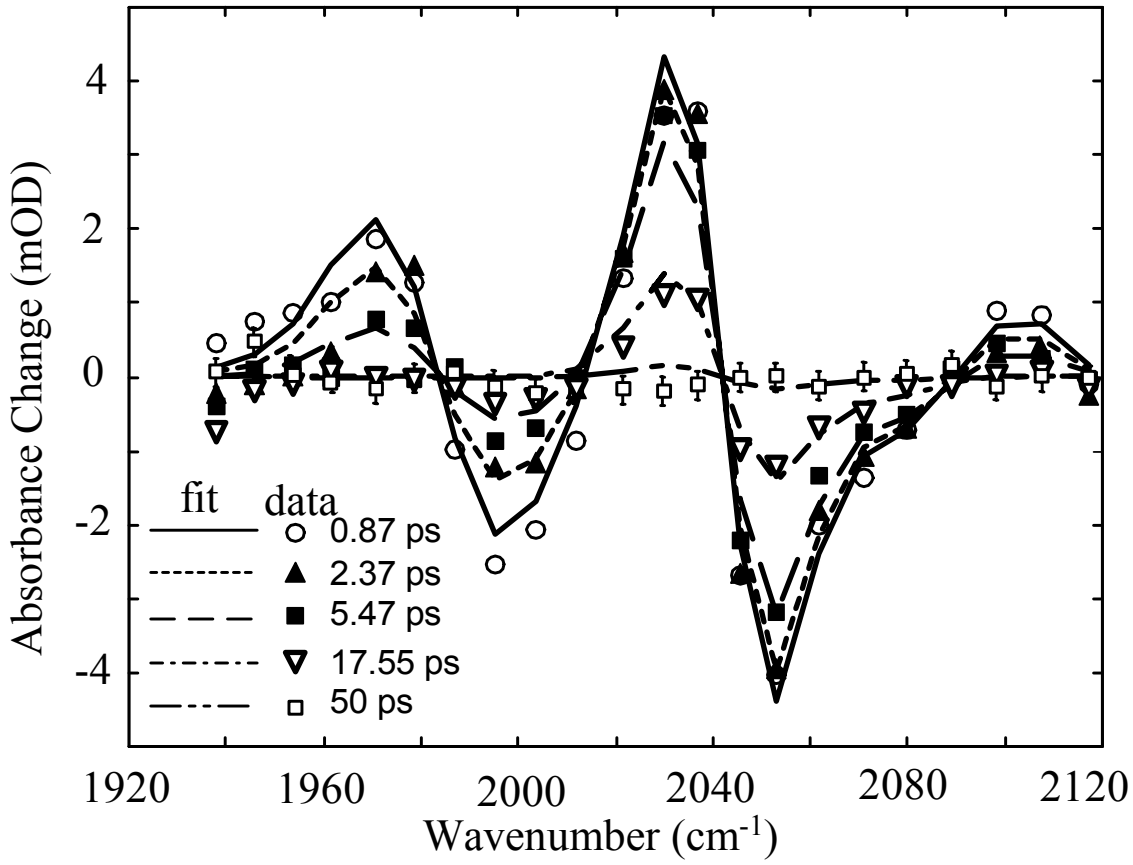

Figure 2-11 Actual and simulated pump probe difference spectra of OsRu in formamide. Open circles correspond to 0.87 ps delay data (solid line is simulation); solid triangles correspond to 2.37 ps delay data (dot line is simulation); solid squares correspond to 5.47 ps delay data (dash line is simulation); open triangles correspond to 17.55 ps data (dash dot line is simulation); open square symbols correspond to 50 ps delay data (dash double dot line is simulation).

TABLE 2-5 Fit Parameters for OsRu Reverse Electron Transfer Kinetics in Formamide

Mode	Initial vibrational populations *via* reverse ET ($F_{j,t}(0)$)			$T_{j,1}$ (ps) ($1/K_{j,1}$)
	$v = 0$	$v = 1$	$v = 2$	
trans CN	0.63 ± 0.1	0.34 ± 0.07	0.03 ± 0.01	3.6 ± 0. 5
cis CN	0.75 ± 0.1	0.25 ± 0.05	0.00 ± 0.02	15 ± 2

2.6. Model for low frequency mode coupling

In contrast with the time resolved OsRu data in formamide, OsRu data in D_2O are not well-fit by the model described above; the low frequency portion of the induced IR absorption shows a time dependent frequency shift that the above model does not describe. A possible explanation is the effect of bath (solvent) heating through coupling a low frequency oscillator to a medium frequency oscillator. This could be a suitable representation of specific, albeit weak, hydrogen bonding of a nitrile ligand to the solvent bath. Others have showed that anharmonic coupling of low frequency modes to a medium frequency mode leads to a temperature dependent shift in the IR transition frequency and broadening of the resonance band.[3,58] We represent the anharmonic potential of the *trans* CN stretch mode coordinate, X, and the intermolecular bond coordinate, x, as a Taylor series in the displacements. As was shown by Cornelius[59] and Hochstrasser,[3] the dominant anharmonic contribution in the series expansion is the term proportional to $\varphi x^2 X^2$, where φ is the coupling constant. The equation of motion may be solved under the Born-Oppenheimer approximation where the *trans* CN stretch motion at high frequency may be solved

for a fixed position of the low frequency mode. If $2\varphi x^2 << M\Omega^2$, where M and Ω are the reduced mass and frequency of the *trans* CN mode respectively, then the transition frequency for the transition from the lowest to the first excited state of the *trans* CN stretching mode is $\Omega(x) = \Omega_{1'1} + \xi x^2$ where $\xi \equiv \varphi/M\Omega$.

The frequency of the low frequency mode is assumed to be less than kT, and the mode's equation of motion, if coupled to a solvent bath, may be represented by a Langevin equation.[3] In the over-damped limit, when the friction γ exerted by the bath on the low frequency oscillator is larger than the oscillator frequency ω, the dynamics are governed by the parameter $\lambda \equiv \omega^2/2\gamma$. Solution of the Langevin equation in the overdamped limit leads to the frequency of the *trans* CN stretch

$$\Omega_{1'1}(t,T)=\Omega_{1'1}+\xi\frac{2\lambda k_B}{m\omega^2}\int_{-\infty}^{t} dt'T(t')e^{-2\lambda(t-t')} \tag{2.12}$$

Here $T(t)$ is an instantaneous bath temperature due to radiationless decay. When the low frequency oscillator is strongly overdamped, the *trans* CN transition frequency becomes linearly proportional to the bath temperature, as the bath and oscillator are in continuous equilibrium.

There is considerable local heating as a consequence of energy release of the radiationless decay process (ca. 12000 cm^{-1}). In our case the origin of temperature/time dependence is due to local solvent/solution cooling. It was shown[41] that temperature as a function of time can be fit as a exponential decay (τ~1-2 ps time constant). Using this assumption, the integral in Equation 2.12 can be calculated directly and Equation 2.12 can be simplified to

$$\Omega_{1'1}(T,t)=\Omega_{1'1}+\frac{\varphi}{M\Omega}\frac{k_BT(t)}{m\omega^2}=\Omega_{1'1}+\frac{\varphi}{M\Omega}\frac{k_B\Delta T(0)\exp(-\frac{t}{\tau})}{m\omega^2}$$

In order to find $\Delta T(0)$, we need to calculate the magnitude of the temperature increase of the surrounding water molecules caused by through radiationless decay of 12000 cm^{-1}. If we

roughly estimate the "heating" volume of the water molecules to include only first solvation shell with size 6 Å x 6 Å x 10 Å, and assume the bulk H_2O heat capacity applies, then $\Delta T(0) \cong 100$ K. We can now apply this model to simulate the transient difference spectra for OsRu in deuterium water. We add a time-dependent frequency shift $\Omega_{1'1}(T,t) - \Omega_{1'1}$ which is proportional to the temperature and time-dependent bandwidth for the *trans* CN mode. The simulated spectra are shown in Figure 2-12. From the simulation, we find that after reverse ET, vibrational levels v=0, v=1, and v=2 of *cis* and *trans* CN are populated. The results are summarized in TABLE 2-6. From the fit, the time constant for the temperature exponential decay process is 1.3 ps which is in good agreement with our previously reported results for a related mixed valence compound[41] and several times faster than is characteristic of bulk thermal conductivity of water. The importance of including the solvent heating effect is shown for *trans* CN stretch region in the inset of Figure 2-12. We note the measured vibrational relaxation times of *trans* CN show faster vibrational relaxation in D_2O than in FA.

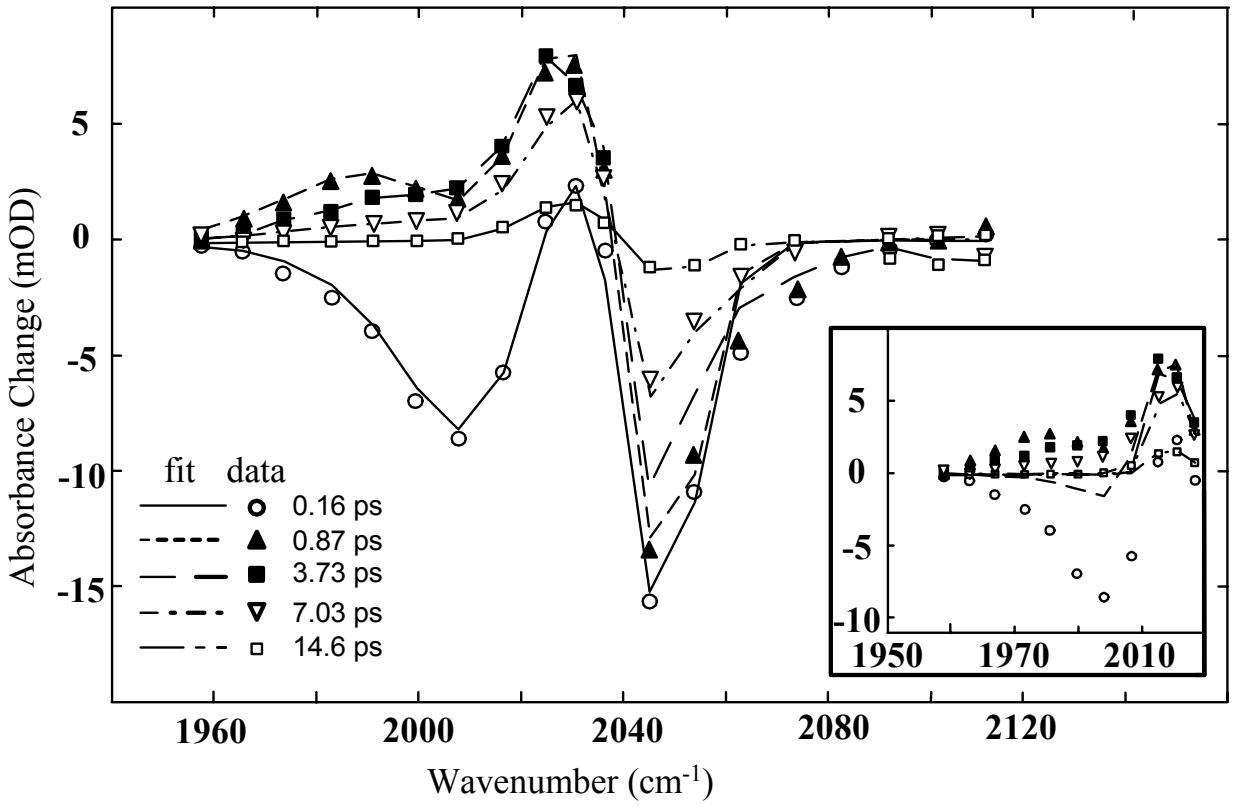

Figure 2-12 Actual and simulated pump probe difference infrared spectra of OsRu in deuterium water. Open circles correspond to 0.16 ps delay data (solid line is the simulation); solid triangles correspond to 0.87 ps delay data (dot line is the simulation); solid squares correspond to 3.73 ps delay data (dash line is simulation); open triangles correspond to 7.03 ps data (dash dot line is the simulation); open squares correspond to 14.6 ps delay data (dash double dot line is the simulation). Inset shows that a model without solvent heating cannot describe the observed kinetics for the *trans* CN stretch region. The inset shows fit results for OsRu at D_2O without solvent heating; the lines are the simulated data.

TABLE 2-6 Fit Parameters for OsRu Reverse Electron Transfer Kinetics in Deuterium Water

Mode	Initial vibrational populations *via* reverse ET ($F_{j,i}(0)$)			$T_{j,1}$ (ps)	$^{*}K_1$, ps^{-1}
	$v = 0$	$v = 1$	$v = 2$		1.33
trans CN	71 ± 5%	23 ± 5%	6 ± 1%	0.81 ± 0.1	
cis CN	75 ± 6%	21 ± 5%	4 ± 1%	3.2 ± 0.3	

* Where K_1 is the time constant for the temperature exponential decay process.

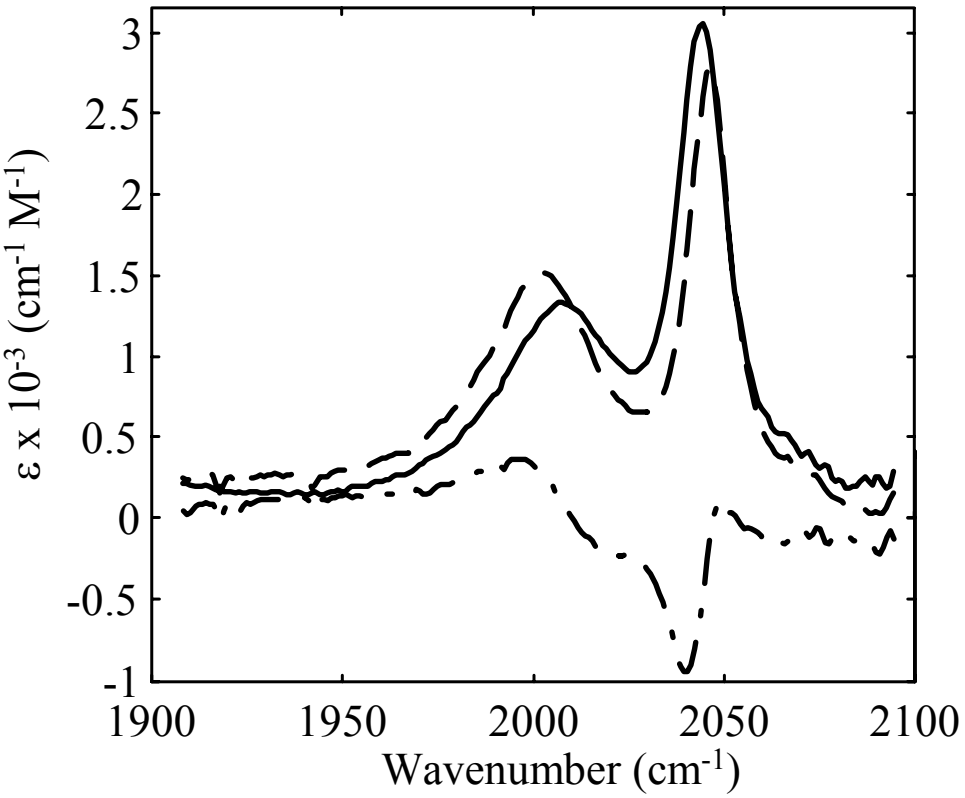

Figure 2-13 Infrared absorption spectra in CN stretch region of OsRu in D_2O at 25°C (solid line), at 90°C (dashed line) and the difference between them (dashed-dotted line).

In order to understand why formamide, a very strong hydrogen bonding solvent does not show a time dependent frequency shift in transient difference spectra, static infrared absorption spectra in CN stretch region in D_2O, formamide and N-methyl formamide (NMF) at 25°C and 90°C were collected (See Figure 2-2, Figure 2-13 and Figure 2-14). From the spectra at 25°C, *trans* CN mode shows very strong solvent (hydrogen bond) coupling in D_2O relative to the smaller coupling for FA and NMF. Static absorption IR spectra of OsRu in D_2O in Figure 2-13 show a *trans* CN band shift of approximately 9 cm^{-1} for a 65°C temperature difference. In contrast, the static temperature dependent absorption difference data in formamide (See Figure 2-14) shows a frequency shift by approximately 4 cm^{-1}. Very significant overlap between OsRu IR absorption band and D_2O IR absorption cross section could provide more efficient energy transfer to the D_2O compared with formamide where the overlap is much smaller. This might explain why the measured vibrational relaxation times of *trans* CN show faster vibration relaxation in D_2O than in FA. Similar effects have been reported previously for the cyanide ion in H_2O and D_2O by Hochstrasser and coworkers[60] and in related SCN^-/OCN^- comparison in methanol by Tominaga and co-workers.[61] The smaller temperature dependent frequency shift in FA explains why the time-resolved data in FA do not show a time-dependent frequency shift in transient difference spectra as in D_2O.

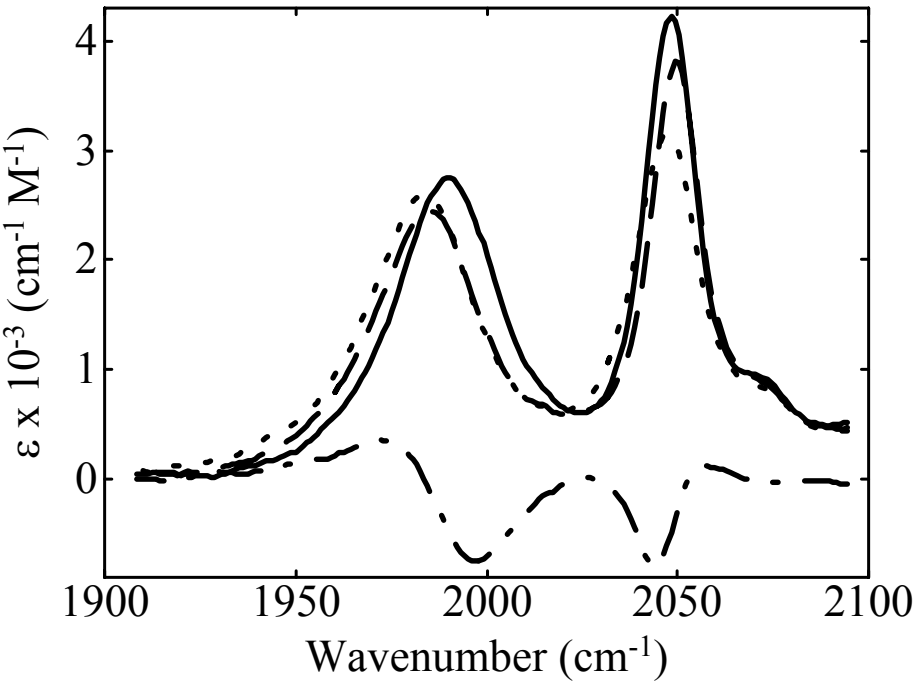

Figure 2-14 Infrared absorption spectra in CN stretch region of OsRu in formamide at 25°C (solid line), at 90°C (dashed line), the difference spectra between them (dashed-dotted line) and in N-methyl formamide at 25°C (dotted line).

It is worthwhile to compare the magnitudes of the frequency shifts of the transient difference and static IR spectra. The maximum frequency shift of the *trans* CN band in transient difference spectra is approximately 15 cm^{-1} in D_2O for the solvent temperature change $\Delta T \approx 100$ °C. We see a shift in the static temperature-dependent absorption difference data of approximately 14 cm^{-1}, suggesting that the short-lived local heating is of a comparable 100 °C magnitude.

2.7. Summary

We have presented the time-resolved infrared spectra of $[(CN)_5Os^{II}CNRu^{III}(NH_3)_5]^-$ in formamide and deuterium water solutions following optical excitation and reverse electron

transfer. The measured reverse electron transfer rates are greater than 3 x 10^{12} s^{-1}. We observe excitations in the non-totally symmetric vibrational mode accompanying reverse electron transfer process in both formamide (FA) and deuterium oxide (D_2O) solutions. Transient infrared absorption spectra showed that non-totally symmetric vibrational mode is populated after reverse ET process. However, no vibrations are highly excited. We have measured the vibrational relaxation time of *trans* CN in D_2O and FA. Our results show faster vibration relaxation in D_2O than in FA, reflecting the correlation between vibrational relaxation time of the OsRu and the IR absorption cross section of the solvent. We have provided a simulation of the spectral dynamics in formamide and deuterium water solutions. In this simulation we included effects of vibrational excitation and relaxation together with effects of the coupling between high frequency stretch-CN mode and low frequency solvent modes which accounts for the major components in the data. The results are similar to previous results for FeRu.

BIBLIOGRAPHY

1. Stratt, R. M. *J. Phys. Chem*. **1996**, *100,* 12981.
2. Eisenthal, K. G. *J. Phys. Chem*. **1996**, *100*, 12997.
3. Voth, G. A.; Hochstrasser, R. M. *J. Phys. Chem*. **1996**, *100*, 13034.
4. Barbara, P. F.; Meyer, T. J.; Ratner, M. A. *J. Phys. Chem*. **1996**, *100*, 13148.
5. Zusman, L. D. *J. Chem. Phys*. **1980**, *49*, 295.
6. Calef, D. F.; Wolynes, P. G. *J. Phys. Chem*. **1983**, *87*, 3387.
7. Sparglione, M.; Mukamel, S. *J. Chem. Phys.* **1988**, *88*, 3265.
8. Van der Zwan, G.; Hynes, J. T. *J. Chem. Phys.* **1982**, *76*, 2993.
9. Sumi, H.; Marcus, R. A. *J. Chem. Phys.* **1986,** *84*, 4894.
10. Marcus, R. A.; Sutin, N. *Biochim. Biophys. Acta* **1985**, *811*, 265.
11. Marcus, R. A. *J. Chem. Phys*. **1956**, *24*, 966.
12. Newton, M. D.; Sutin, N. *Annu. Rev. Phys. Chem*. **1984**, *35*, 437.
13. Hwang, J. K.; Creighton, S.; King, G.; Whitney, D.; Warshel, A. *J. Chem. Phys.* **1988**, *89*, 859.
14. Bixon, M.; Jortner, J. *Chem. Phys*. **1993**, *176*, 467.
15. Jortner J.; Bixon, M. *J. Chem. Phys*. **1988**, *88*, 167.
16. Bader, J. S.; Kuharski, R. A.; Chandler, D. *J. Chem. Phys.* **1990**, *93,* 230.
17. Coalson, R. D.; Evans, D. G.; Nitzan, A. *J. Chem. Phys.* **1994**, *101,* 436.
18. Myers, A. B. *Chem. Phys.* **1994**, *180,* 215.
19. Myers, A. B. *Chem. Rev.* **1996**, *96,* 911.
20. Maroncelli, M.; Fleming, G. R. *J. Chem. Phys*. **1987**, *86*, 6221.

21. Nagasawa, Y.; Yartsev, A. P.; Tominaga, K.; Bisht, P. B.; Johnson, A. E.; Yoshihara, K. *J. Phys. Chem*. **1995**, *99*, 653.

22. Wynne, K.; Galli, C.; Hochstrasser, R. M. *J. Chem. Phys*. **1994**, *100*, 4797.

23. Walker, G. C.; Barbara, P. F.; Doorn, S. K.; Dong, Y.; Hupp, J. T. *J. Phys. Chem*. **1991**, *95*, 5712.

24. Asahi, T.; Mataga, N. *J. Phys. Chem*. **1992**, *93*, 6575.

25. Gould, I. R.; Young, R. H.; Moody, R. E.; Farid, S. *J. Chem. Phys*. **1991**, *95*, 2068.

26. Kosower, E. M.; Huppert, D. *Annu. Rev. Phys. Chem*. **1986**, *37*, 127.

27. Weaver, M. J.; McManis, III, G. E. *Acc. Chem.Res.* **1990**, *23*, 294.

28. Simon, J. D.; Doolen, R. *J. Am. Chem. Soc*. **1992**, *114*, 4861.

29. Lippert, E.; Rettig, W.; Bonacic-Koutecky, V.; Heisel, F.; Miehe, J. A. *Adv. Chem. Phys.* **1990**, *92*, 7241.

30. Nocek, J. M.; Zhou, J. S.; DeForest, S.; Priyadarshy, S.; Beratan, D. N.; Onuchic, J. N.; Hoffman, B. M. *Chem. Revs.* **1996***, 96,* 2459.

31. Barbara, P. F.; Jarzeba, W. *Adv. Photochem*. **1990**, *15*, 1.

32. Maroncelli, M.; MacInnis, J.; Fleming, G. *Science*, **1989**, *243*, 1674.

33. Oxtoby, D.W. *Ann. Rev. Phys. Chem.* **1981**, *32*, 77.

34. Simon, J. D.; Su, S. G. *Chem. Phys.* **1991**, *152*, 143.

35. Reid, P. J.; Silva, C.; Barbara, P. F.; Karki, L.; Hupp, J. T. *J. Phys. Chem*. **1995**, *99*, 2609.

36. Simon, J. D. *Acc. Chem. Res*. **1988**, *21*, 128.

37. Bagchi, B. *Ann. Rev. Phys. Chem.* **1989**, *40*, 115.

38. Maroncelli, M.; Fleming, G. *J. Chem*. *Phys.* **1988**, *89*, 5044.

39. Grampp, G.; Harrer, W.; Hetz, G. *Phys. Chem.* **1990**, *94*, 1343.

40. Wang, C.; Mohney, B.K.; Williams, R.D.; Petrov, V.; Hupp, J.T.; Walker, G. C. *J. Am. Chem. Soc.* **1998**, *120*, 5849.

41. Wang, C.; Mohney, B. K.; Akheremitchev, B. B.; Walker, G. C. *J. Phys. Chem*. *A.* **2000**, *104,* 4314.

42. Stratt, R. M. *J. Phys. Chem*. **1996**, *100,* 12981.

43. Eisenthal, K. G. *J. Phys. Chem*. **1996**, *100*, 12997.

44. Voth, G. A.; Hochstrasser, R. M. *J. Phys. Chem*. **1996**, *100*, 13034.

45. Barbara, P. F.; Meyer, T. J.; Ratner, M. A. *Ibid.* **1996**, *100*, 13148.

46. Myers, A. B. *Chem. Phys*. **1994**, *180*, 215.

47. Myers, A. B. *Chem. Rev.* **1996**, *96*, 911.

48. Walker, G. C.; Barbara, P. F.; Doorn, S. K.; Dong, Y.; Hupp, J. T. *J. Phys. Chem*. **1991**, *95*, 5712.

49. Akhremitchev, B.; Wang, C.; Walker, G. C. *Rev. Sci. Inst.* **1996**, *67,* 3799.

50. Hupp, J. T.; Meyer, T. J. *Inorg. Chem*. **1987,** 2332.

51. Kober, E. D.; Goldsby, K. A.; Narayana, D. N. S.; Meyer, T. J. *J. Am. Chem. Soc.* **1983**, *105*, 4303.

52. Zink, J. I. *Coord. Chem. Rev*. **1985**, *64*, 93.

53. Heller, E. J.; Sunberg, R. L.; Tannor, D.J. *J. Phys. Chem.* **1982**, *86*, 1822.

54. Hester, R. E.; Nour, E. M. *J. Chem. Soc. Dalton Trans.* **1981**, 939.

55. Swanson, B. I. *Inorg. Chem.* **1976**, *15*, 253.

56. The vibrational anharmonicity of the CN stretch is taken to be 22 cm^{-1} in our case, as shown in Durand, D.; Carmo, L. C. S.; Luty, F. *Phys. Rev. B* **1989**, *39*, 6096.

57. Marin, T. W.; Homoelle, B. J.; Spears, K. G. *J. Phys. Chem. A*. **2002**, *106*, 1152.

58. Yeh, A. T.; Shank C. V.; McCusker, J. K. *Science* **2000**, *289*, 935.

59. Shelby, R. M.; Harris, C. B.; Cornelius, P. A. *J. Chem. Phys*. **1979**, *70*, 34.

60. Hamm, P.; Lim, M.; Hochstrasser, R. M. *J. Chem. Phys.* **1997**, *107*, 10523.

61. Ohta, K.; Maekawa, H.; Saito, S.; Tominaga, K. *J. Phys. Chem. A* **2003**, *107*, 5643.

3. ADHESION FORCES IN CONDUCTING PROBE ATOMIC FORCE MICROSCOPY[§]

This paper examines how the adhesion force between a conducting probe and a conductive surface influences the electrical properties of conductive polymers. Conducting Probe Atomic Force Microscopy (CP-AFM) was employed. When a voltage is applied between the sample and the tip, an attractive electrostatic capacitance force is added to the adhesion force. The tip-sample capacitance force in the CP-AFM of polythiophene monolayers is described through theoretical modeling and compared with experiment. Experiments were performed in an insulating organic solvent that decreased the adhesion force by approximately ten times relative to measurements in air. The results for the adhesion force measurements as a function of applied bias show good agreement with the theoretical prediction. Based on the dependence of the adhesion force *versus* applied bias and the current-voltage characteristics of polythiophene, we conclude that characterization of electrical properties of conducting polymers using CP-AFM at a desired force requires knowledge of the adhesion force.

3.1. Introduction

Conductive polymers[1,2] are facilitating the development of numerous applications, such as antistatic coatings for electronic packaging,[3] light-emitting plastics[4] and volatile organic gas

[§] This work has been originally published as Tivanski, A. V.; Bemis, J. E.; Akhremitchev, B. B.; Liu, H.; Walker, G. C. *Langmuir* **2003**, *19*, 1929-1934.

sensors.[5] These polymers are also being investigated as fundamental building blocks for molecular electronics.[6-8] The development of many of these applications requires reliable methods to measure conductive properties at the nanoscale. Different approaches[9-18] have been attempted to investigate such properties of metal-molecule-metal junctions. To probe such junctions one could use scanning tunneling microscopy (STM),[19-22] Kelvin force microscopy (KFM),[23-26] mechanically controllable break junction (MCB),[9] or conductive probe atomic force microscopy (CP-AFM).[11-13,27-32]

However, these STM, KFM and MCB experiments have demonstrated that unambiguous contact to a nanoscale objects is difficult to achieve and, what is more important, difficult to control. On the other hand, CP-AFM provides excellent control over mechanical contacts, especially for single molecule studies. The utility of the AFM for electrical measurement stems directly from the ability of the AFM to operate on either conducting or nonconducting surfaces because position control is maintained by measuring the mechanical forces acting on the tip. Thus, the current can be measured independently of the tip-sample distance and the interaction force can be measured.

One of the main goals in measuring conductivity at the nanoscale is to obtain current-voltage characteristics of nanoscale devices. Since a conductive probe is placed into contact with the conductive polymer, there is a pressure with which the conductive probe pushes into the surface. As we will show later, this pressure depends on the applied external bias because the applied bias modifies the adhesion force. Variable pressures between the tip and the sample modify overlapping of electronic wave functions that participate in the process of injecting the carriers from the electrode (conductive probe) to the conductive polymer. This modifies the injection barrier and could dramatically change the conductive properties of the studied nanocontact. In

order to obtain accurate conductive characteristics of the sample, it is necessary to perform measurements under constant pressure.

In this paper, we have performed studies of the conductive and adhesive properties of a polythiophene monolayer coupled between two gold electrodes using CP-AFM. A gold-coated conductive AFM probe served as one electrode and the other was the gold substrate on which polymers had been grafted. Experiments were performed in an insulating solvent in order to decrease the adhesion force (the measured adhesion force in air was roughly ten times larger than in organic solvent). Our results show that the adhesion force between conductive probe and conductive sample depends on the applied external bias. We find that inclusion of a capacitance force between conductive probe and conductive sample can explain the adhesion properties of our system and can be used to obtain the dependence of the adhesion force on applied external bias. We observed an increase in conductivity with increasing applied pressure. Our results show that under pressure, the contact area alone can not explain the observed conductivity; the potential barrier for charge injection is reduced. Our results show that neglecting the adhesion forces contribution to the overall interaction force between conductive probe and the sample can provide significantly inaccurate estimates of the pressure between the conducting tip and the sample, and thus conductive properties of the nanoscale devices should be interpreted in light of this additional adhesion force. This effect would be less pronounced in air, where adhesion forces are much larger.

3.2. Experimental details

A commercial atomic force microscope (Molecular Force Probe, Asylum Research, Santa Barbara, California) was used in this work. It was modified to permit conductivity measurements between the AFM probe and the sample. The idealized schematic representation of the experimental setup is shown at Figure 3-1.

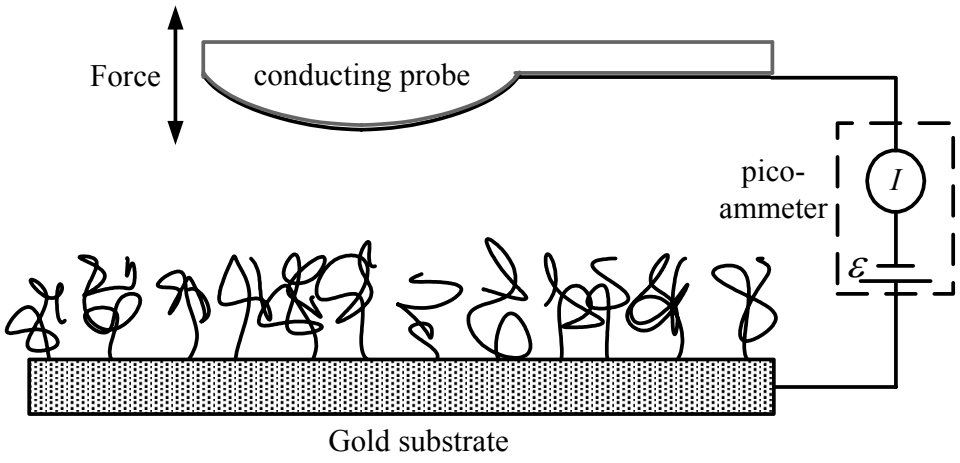

Figure 3-1 An idealized diagram of the apparatus used to measure currents using a force microscope.

The capability of AFM to precisely position a conducting probe on the sample surface and measure the force between the probe and the sample was exploited. The probe tip was a commercial contact mode silicon nitride V-legged probe (Digital Instruments Inc., Santa Barbara, California) coated with 50 nm of gold. Spring constants were calibrated using the Sader method[33,34] and typically had values of 0.1 nN/nm. Substrates for the polymer monolayers were 12 mm diameter 99.99% gold discs (Testbourne Ltd., Hampshire, England). A commercial

pico-ammeter (Chem-Clamp, Dagan Corp, Minneapolis, Minnesota) was used to apply a bias to the conducting probe and enabled sensitive measurements of the current passing between the conductive probe and the conductive surface through the sample. Thus, by applying different biases, the current through the polymer layer can be measured as a function of tip-sample separation simultaneously with detection of the force between tip and the surface. Force *versus* distance plots were obtained by moving the cantilever and pushing the tip against the surface. The difference between the signals in the two segments gives the vertical deflection signal, and hence the applied force. In order to decrease the probable effect of contamination of the tip over repeated measurements, when we started to see that the conductivity decreased under similar conditions or observed evolution of the force curves over repeated measurements, we stopped collecting data and changed the tip.

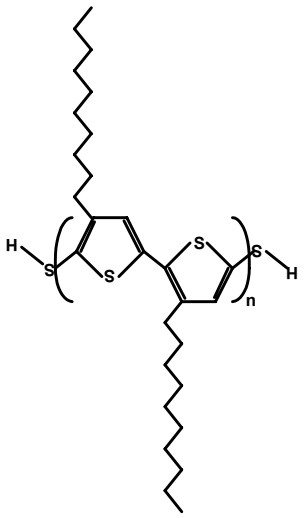

Figure 3-2 Molecular structure of the undoped poly (decyl-thiophene) polymer.

The polymer used in this work was undoped poly (decyl-thiophene) (PT) regio-regular head-to-tail end functionalized with mercapto groups[35] (See Figure 3-2). Good electrical contacts between gold electrodes and the sample can be achieved through the sulfur-gold covalent chemical bond.

Gold substrates were cleaned for 12 hours in piranha solution (1:3 of 30% H_2O_2/98% H_2SO_4). *Caution! Piranha solution has very strong oxidizing power and is extremely dangerous to handle in the laboratory; gloves, goggles, and face shields are needed for protection*. Tips were cleaned in piranha solution for two hours. Tip holder and sample holder were cleaned in a detergent solution (10% FL-70, 90% H_2O) for 2 hours. Then, tips, tip holder and sample holder were thoroughly rinsed in deionized water and dried in a stream of nitrogen gas.

Polymer and 1,4 benzene dimethanethiol (BDT) (Aldrich) were grafted to gold surfaces as follows. In order to prepare samples, the undoped PT and BDT were dissolved in freshly distilled tetrahydrofuran (THF) at concentration of 10 μM and 1 mM respectively. The gold disks were soaked in the polymer solution for about 30 for PT and 12 hours for BDT. The disks were next soaked in freshly distilled THF for 12 hours, and finally $NaBH_4$ (Aldrich) was added in excess to the solution and left for 30 hours. After incubation, the substrates were cleaned of excess polymer or BDT by sonication in THF and dried in a stream of nitrogen gas. The sodium borohydride was added to reduce the disulfide linkages between polymer chains and between BDT molecules, which formed during storage. During these steps the solution and surface were kept in enclosed weighing bottles. All these steps were performed at the room temperature. All samples were used within two days of preparation. The conductivity measurements using CP-AFM were performed in insulating, tetradecane solvent. The polymer was characterized using gel permeation chromatography (GPC).[36] GPC of polythiophene reduced by addition of $NaBH_4$

was collected relative to the calibration with polystyrene standards. An ellipsometer (L117, Gaertner Corp, USA) was used to determine the film thickness of the polythiophene monolayer. The measurements were done at a 70^0 incident angle, using a He-Ne laser (6.33 nm) as the light source. Samples to be studied by ellipsometry were examined within minutes after grafting of the polymer.

3.3. Results and discussion

GPC provided number average molecular weight M_n=26000 Daltons, weight average molecular weight M_w=46000 and polydispersity index PI=1.8. The polythiophene monomer's molecular weight is 222 Daltons, and the monomer length is 3.8 Å. Thus the approximate number of the monomers in the polymer chain was 110 repeat units. The unperturbed radius of gyration R_g was estimated to be 2.3 nm using the following equation

$$R_g = l\sqrt{M_w / 6M_0} \ .$$

A typical force plot for the conductive measurements is shown on Figure 3-3. In this force plot the applied bias was –3 V. The zero force is selected as the force when tip was far away from the surface, which can be considered constant for the different biases since electrostatic interactions become negligible at such distance. The gray line corresponds to the force during the approach of the tip to the surface. When the tip-sample separation reaches a point where the gradient of interaction force is greater than the spring constant of the cantilever, the tip jumps into the contact with the surface. The tip continues to push against the surface increasing the tip-sample force until the controller switches the direction of the tip motion. Force registered during subsequent motion is illustrated by the black line. The tip remains in contact with the surface

until the force of adhesion is exceeded; the tip jumps away to a distance that is equal to the force of adhesion divided by the spring constant of the cantilever. This jump-off event is shown by the dashed line. The interaction force between the tip and underlying sample at their contact is considered to be equal to the sum of two forces, the adhesion force and the force with which the cantilever pushes tip into the sample. The force applied by the tip is measured by recording the cantilever deflection during the entire approach-withdrawal cycle, while the adhesion force is measured during the jump-off event only.

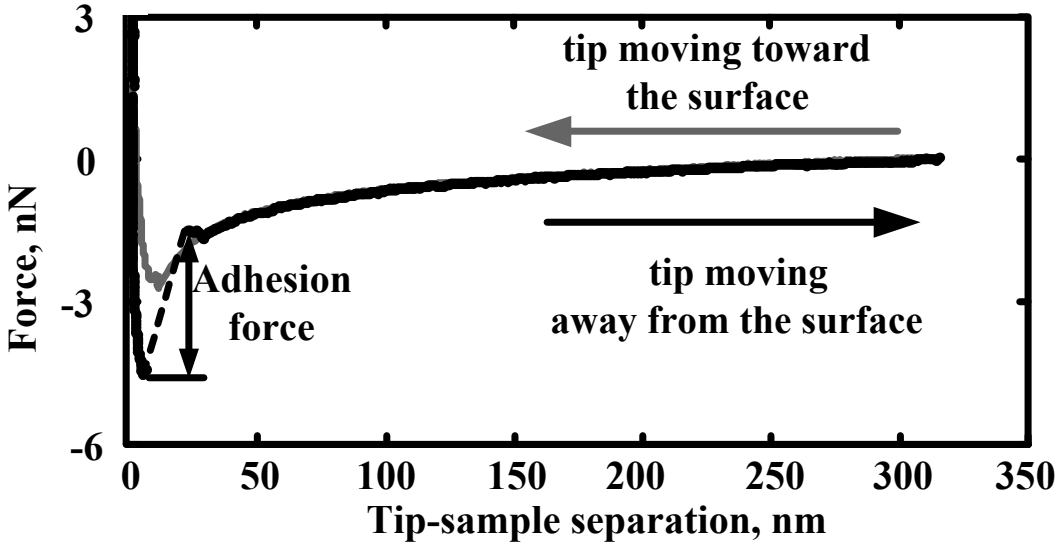

Figure 3-3 The long-range attraction force and the jump-off event during breaking of contact between the tip and the polymer.

The results show the presence of a long-range force. This force depends on the tip-sample separation and, as will be discussed later, on the applied bias. The long-range forces disappeared with no bias applied; thus the electrostatic nature of these forces is implicated.

Now we consider the origin of the electrostatic force. If a voltage is applied between two different conducting materials (in this case the conducting tip and the conducting sample), then an attractive force is added to the overall forces experienced by the probe. The difference in potential V between the tip and the sample produces an electrostatic energy of the form:

$$E_{elec} = \frac{1}{2} C V^2$$

where C is the capacitance between the tip and the sample. This can be differentiated with respect to the tip-sample separation, z, to give the capacitance force between them:

$$F_{capac} = -\frac{1}{2} \frac{dC}{dz} V^2$$

It is important to point out that even in the absence of an applied potential, some capacitance force may still exist due to the contact potential difference between different materials.[37]

The electrostatic force between the probe and the sample has two contributions: one is from the cantilever body and another is from the tip. The electrostatic force between the conductive cantilever body and conductive sample system is typically about 50-100 pN and has very weak distance dependence,[38] and since our forces are much larger, we will neglect the electrostatic force acting on the cantilever body.

The tip shape can be modeled as a truncated cone ended by a spherical apex and with a total length L_{tip}=5 μm, half angle θ=35^0 and apex radius R=100 nm. We will use method of Hudlet *et al*,[37] to approximate the capacitance force between the tip and the surface. For small distances ($d<R$), the force depends on the tip-sample separation as d^{-1}, which is the same as the force (for $d<R$) between a sphere and a semi-infinite conductive plane.[38] For distances $R<d<L$ the force has a logarithmic dependence on the tip-sample separation, and this can be related to the

uniformly charged line model.[39] Since the jump-off event occurs at rather a small tip-sample separation, we can approximate our capacitance force as

$$F_c(d) = -\pi\varepsilon_0\varepsilon_r V^2 \frac{R}{d} \tag{3.1}$$

where ε_r is an effective dielectric constant of the polymer-solvent system that is taken to be 2.5.

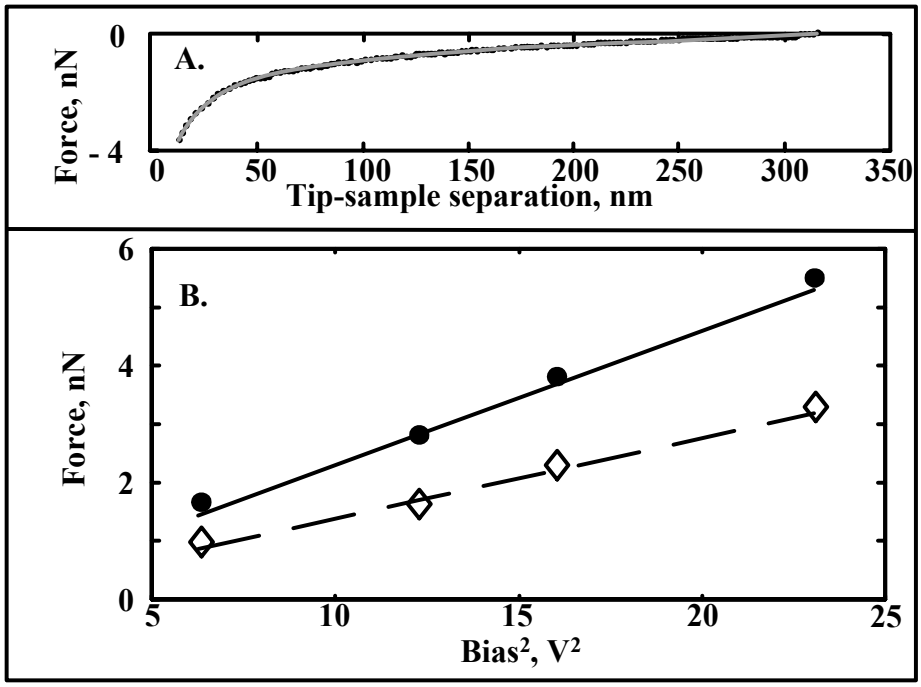

Figure 3-4 Upper Panel (A). Theoretical (gray line) and experimental (black dots) force dependence on tip-sample separation. Lower Panel (B). Experimental (diamonds 50 nm, points 30 nm tip sample separation) and theoretical (solid line 30 nm, dashed line 50 nm) dependence of the force on the applied bias.

Figure 3-4 A) represents experimental data (black dots) and calculated values (gray line) of the force for the approach data at applied bias –3.5 V as a function of tip-sample separation. Calculations were performed using Equation 3.1 for the electrostatic capacitance force as a

function of tip-sample separation for a fixed applied bias. Good agreement with experimental data has been found. Equation 3.1 also shows that force depends quadratically on the applied bias. Figure 3-4 B) shows how the force on the tip depends on the applied bias, when the tip is not in contact with the surface. The dots represent experimental data and the solid line represents a theoretical prediction given a tip-sample separation of 30 nm; diamonds represent experimental data and the dashed line represents the theoretical prediction given that the tip is 50 nm away from the surface. Here the zero force is the force on the tip when it is far away from the surface. Good agreement between the theory and experimental results provides additional confirmation that long-range forces acting on the conductive probe can be described using capacitance model. Thus we can now attempt to describe adhesion forces between conductive probe and the sample using our capacitance model.

In order to calculate the adhesion force we first have to estimate the tip-sample separation at which tip jumps away from the surface. This event occurs when the gradient of adhesion force becomes less than the spring constant of the cantilever. Thus, this distance can be determined from the following equation:

$$\left(\frac{dF}{dz}\right)_{z=z_{adh}} = -k_c \tag{3.2}$$

By combining Equations 3.1 and 3.2, one obtains an expression for the adhesion force as a function of applied bias:

$$F_{adh} = V\sqrt{\pi R \varepsilon_0 \varepsilon_r k_c} \tag{3.3}$$

Equation 3.3 shows that the adhesion force depends linearly on applied bias. For our particular system the dependence of the adhesion force on the applied bias is predicted to be linear with a slope of -0.8 nN/V in the negative bias region and 0.8 nN/V in positive.

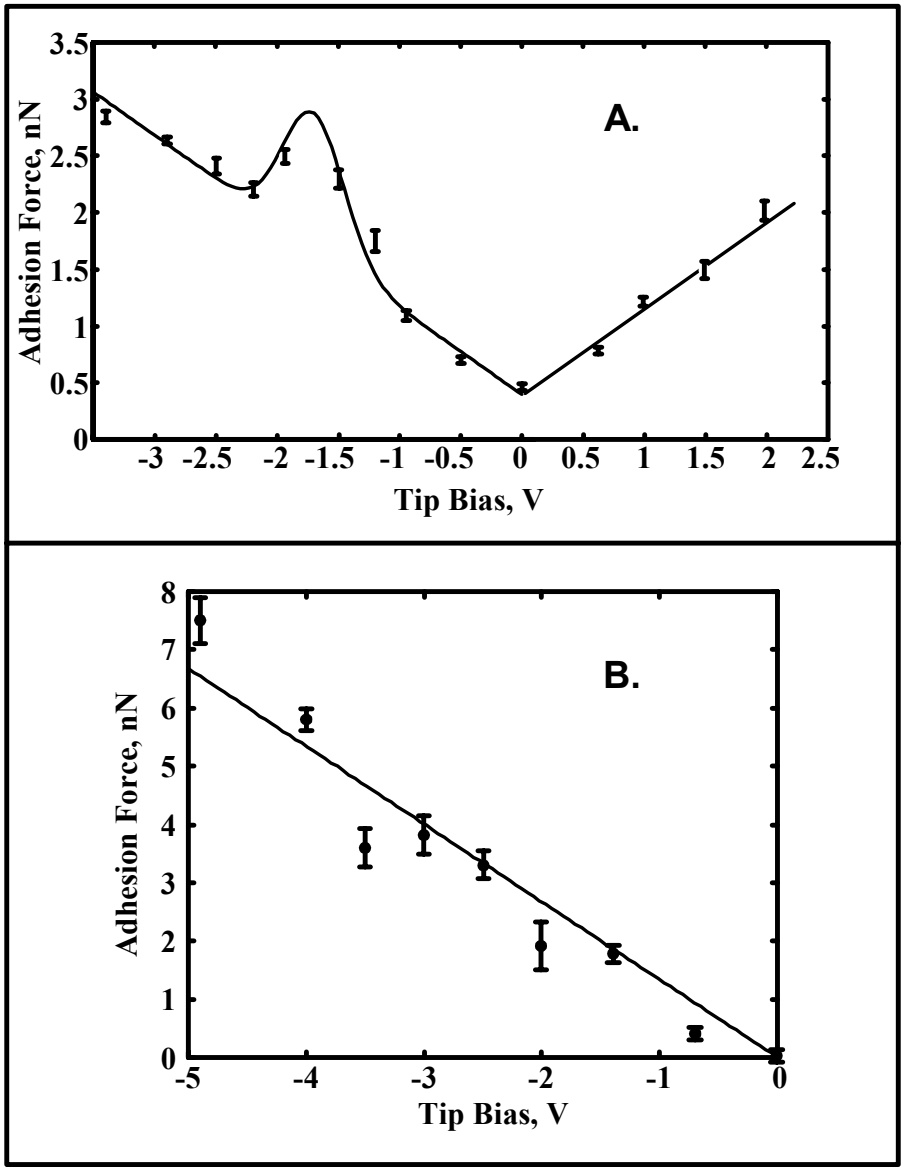

Figure 3-5 Upper Panel (A). Adhesion force as a function of applied bias. Data are represented by dots with error bars, the solid line is a fit to the data using Equation 3.4. Lower Panel (B). Adhesion force (diamonds) and the best fit line for 1,4 benzene dimethanethiol sample.

Figure 3-5 (A) shows the adhesion force (dots with error bars as the standard deviation of a series of repeated measurements) as a function of applied bias. It is important to point out that magnitudes for the adhesion force depend on both electrostatic and non-electrostatic

contributions. As can be seen in the figure, the adhesion force is not zero at an applied bias of 0 V, but has a value of F^{int}=0.45 nN. This intrinsic adhesion force the sample has been added to the calculated dependence.

The experimental dependence of the adhesion force in the negative bias region deviates from linear behaviour; it shows a peak in the range of applied biases from approximately -1.2 V to -2.2 V. The undoped polymer chain is nonconductive until it oxidizes at the applied biases more negative than approximately –1.8 V, which corresponds to the approximate maximum of the adhesion deviation peak. Figure 3-5 (B) shows the adhesion force (diamonds) for 1,4 benzene dimethanethiol as a function of applied bias. As will be discussed below, this sample is not expected to undergo redox transitions in this range of applied bias. As can be seen from the figure, the experimental dependence of the adhesion force in the negative bias region does not deviate from linear behavior, as compared to the polythiophene results. Our cyclic voltammogram measurements showed that this polythiophene oxidizes at approximately 0.7 V relative to the Ag/AgCl reference electrode. While the exact voltage of the CP-AFM oxidation peak remains to be discussed below, we conclude that the peak in Figure 3-5 originates in an oxidation state change of the polymer layer under the tip. In the CP-AFM experiments the surface with grafted polythiophene is oxidized when the surface is at a positive potential relative to the tip. If the oxidation potential of the polymer chain has a Gaussian distribution, and we assume that the additional capacitance due to the presence of positive charges is directly proportional to their number, then the expression of the adhesion force (Equation 3.3) will be

$$F_{adh} = V\sqrt{\pi R \varepsilon_0 \varepsilon_r k_c} + F_{adh}^{\text{int}} + A\exp[-(V - V_0)^2 / 2\sigma^2] \qquad (3.4)$$

The solid line in Figure 3-5 represents fit of the adhesion force data using Equation 3.4. The fit puts the center of the Gaussian at V_0 = -1.7 V and its standard deviation at σ = ± 0.25 V (A is a scaling factor).

This effect can be explained qualitatively as follows. When the polymer chain oxidizes, electrons will be removed from the molecule to the gold substrate; thus the chain becomes positively charged. These holes transport through the polymers backbone toward the negatively charged tip; thus the effective width of the capacitor between the tip and the sample has been decreased, and that in turn increases the interaction force. The force increases until the holes move to conjugated energy levels that are spatially closest to the tip, providing the maximum force because this configuration represents smallest width of the capacitor. When the bias is high enough, holes overcome the potential barrier between the tip and the polymer and move to the tip, thus current starts to flow, corresponding to the maximum of the peak at the adhesion force. Because positive charges are now removed from the chain, the effective width of the capacitor decreases and thus the interaction force decreases. After positive charges are removed from the polymer backbone, the chain can oxidize again; because there is no potential trap at the interface between the conductive tip and the polymer, the holes will not be stored near the tip and on a time-average the effective distance between capacitor plates is larger than when positive charges are trapped by the potential. Thus by increasing the absolute value of the bias, the added additional adhesion force diminishes and the adhesion force can be represented again using Equation 3.3.

Our cyclic voltammograms exhibit an oxidation peak at 0.7 V relative to the Ag/AgCl electrode with a standard deviation of +/- 0.05 V that is five times smaller than we observed at the adhesion force peak. The origin of this discrepancy is probably from the energetic distribution of

polymer HOMO states. In conjugated polymers, conformational variations will produce different conjugation lengths, which will vary the energy of the carrier. More experimental work and theoretical modeling is required to better understand this behavior.

When a conductive probe contacts the polymer, there is a pressure with which the probe pushes into the surface. Pressures between the tip and the sample modify the overlap of electronic wave functions that participate in the injection of carriers from electrode (conductive probe) to the conductive polymer. This pressure modifies the injection barrier and dramatically alters the observed conductive properties of the studied molecule. Thus, in order to perform accurate characterization of the conductive properties of the sample, such measurements should be performed under constant pressure. Since the experiments reported here utilized the same cantilever, we can assume that the pressure under the tip is proportional to the interaction force. It is essential to point out that measurements under a constant interaction force and measurements under a constant force with which the cantilever pushes the tip into the sample provide different results, since part of the interaction force is an adhesion force that is bias dependent. The difference between measurements with constant interaction and constant applied force is illustrated at Figure 3-6. This figure shows two current-voltage (*I-V*) characteristics of the polythiophene molecules under constant interaction and constant loading force. A non-constant difference between the *I-V* curves arises because the adhesion force is bias dependent.

Figure 3-7 shows the current-voltage dependence for the gold-polythiophene-gold system at a constant interaction force between the tip and the sample, for the different interaction forces (ranging from 2 nN to 7 nN). Each line represents one value of the force.

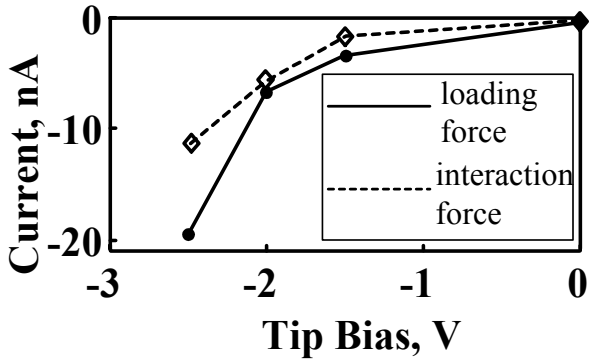

Figure 3-6 Current *versus* voltage, under constant interaction force and constant loading force. In both cases the force magnitude is 7.5 nN.

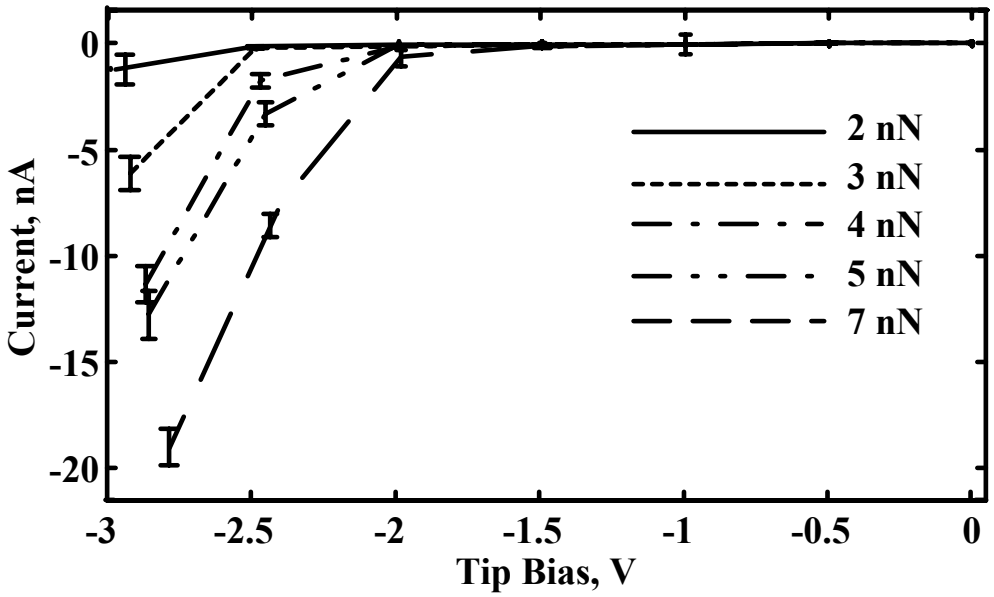

Figure 3-7 Current dependence on voltage for the gold-polythiophene-gold system at five different constant interaction forces between tip and the sample.

The importance of the interaction force between the tip and the sample is clearly shown by this figure; by applying more force onto the sample, the conductivity is increased, probably because the width of the potential barrier for injection from the gold electrode into polymer is decreased.

Such changes can be qualitatively understood by using simple ideas about tunneling through the potential barrier created at the interface between the gold electrode and the sample. The probability for the charge carrier to travel through such a potential barrier would decrease exponentially with both the width and the height of a potential barrier. By applying more pressure, the spatial separation between conductive probe and the sample is decreased; this in turn will increase the current. On the other hand, the electrodes become closer to each other, thus the overlap of the electronic wave functions participating in injection is increased, thus the potential barrier is decreased and this in turn will also increase the current.

Another observation from this figure is that, for applied biases less in absolute value than 1.5-2 V, the current is very small, and for larger biases it increases significantly. In order to understand this, we consider a hole injection mechanism between the Fermi level of the gold electrode and the HOMO energy level of the conductive polymer, closest to the Fermi level. We will use Fowler-Nordheim theory for charge injection mechanism[40,41] between metal electrode and polymer semiconductor. Based on Ouisse's work,[42] an analytical expression for the effective Fowler-Nordheim barrier between metal electrode and semiconductor is

$$\Phi_{eff} = (I^{3/2} - E_{Au}^{3/2})^{2/3} \tag{3.5}$$

Here E_{Au} is the work function of the gold electrode, and I is the ionization potential of the polythiophene. Based on the cyclic voltammograms (CV) the ionization potential relative to the vacuum is I=5.4 eV. This is the value obtained by *ab initio* Hartree-Fock calculations[43] when there is an average 20^0 torsion angle between adjacent thiophene rings. The work function of gold E_{Au}=5.2 eV. By substituting these values into Equation 3.5 for an effective injection potential for the holes one would obtain Φ_{eff} = 0.8 eV. This predicted barrier is significantly

smaller than observed in the CP-AFM experiments, though we note that contact resistance and other limiting factors have been neglected and may account for the discrepancy.

The predicted potential barrier for the electrons can be calculated the same way as for the holes. We consider a charge injection mechanism between the Fermi level of the gold electrode and the LUMO energy level of the conductive polymer, closest to the Fermi level. The effective Fowler-Nordheim barrier between metal electrode and semiconductor is

$$\Phi_{eff} = (E_{Au}^{3/2} - EA^{3/2})^{2/3} \tag{3.6}$$

Here *EA* is the electron affinity of the polythiophene. Based on the cyclic voltammograms (CV) the electron affinity relative to the vacuum is *EA*=3 eV. By substituting these values into Equation 3.6 for an effective injection potential one would obtain Φ_{eff}=3.6 eV. Thus this sample is not expected to undergo redox transitions in the range of applied bias from 0 to 2.5 V.

Another possible argument for the conductivity of the polymer chain increasing with increasing of pressure applied onto the sample is that the contact area between the conductive probe and the sample also increased. We can use JKR theory[44] to relate the contact area and the adhesion force. If the probe is treated as an elastic sphere and the sample as an elastic flat surface, then according to JKR theory[44] the contact area just before the jump-off between a sphere of radius *R* on the flat surface would depend on the interaction force as follows

$$a^2 = (\frac{R}{K} F_{adh})^{2/3} \tag{3.7}$$

where *K* is effective elastic modulus of the conductive probe and the sample. Figure 3-8 shows how the conductivity, at biases -2.5 V and –3 V depends on the adhesion force to the 2/3 power. If the increase in the contact area with the increase of the adhesion force is fully responsible for the increase in conductivity, we should observe a linear dependence. The observed dependence

is clearly nonlinear. Therefore, a contribution to conductivity that goes beyond contact area is relevant.

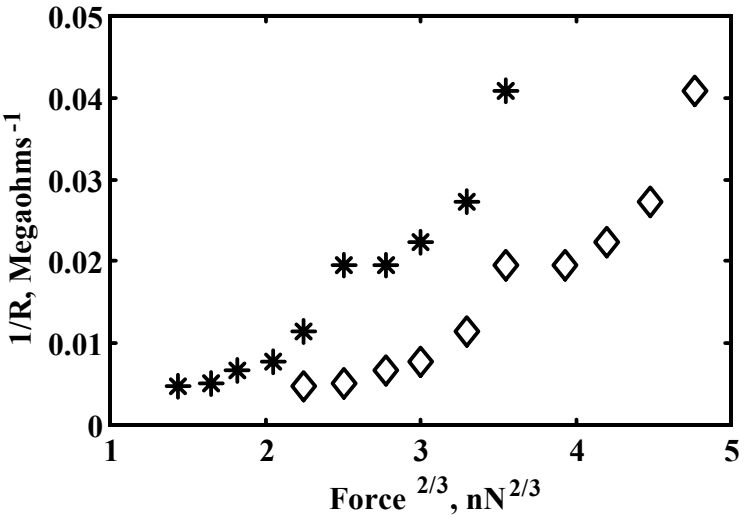

Figure 3-8 Conductivity as a function of contact area, at biases of –2.5 V (diamonds) and – 3 V (stars).

As protocol for the electrostatic characterization of the nanoobjects using CP-AFM we suggest the evaluation of the adhesion force as a function of applied bias. One should perform all conductive measurements under the same interaction force, recognizing that it is the sum of the adhesion force and the force applied on the tip. A suitable technique for this protocol would be detection of the force as a function of tip-sample separation simultaneously with current detection as a function of tip-sample separation.

3.4. Conclusions

In this work we have measured the conductance of nanocontacts between gold-grafted polythiophene SAM and conductive tip in tetradecane solvent under different applied load using CP-AFM. We have shown theoretical and experimental results of how the electrostatic part of the adhesion force depends on the applied external bias. Experiments have been performed in insulating organic solvent that decreased adhesion force approximately ten times relative to the air measurements. Results showed good agreement with the analytical expressions of the capacitance force as a function of applied bias and tip-sample separation both at the jump off event and at long-range forces. We observed an increase in conductivity with increasing applied pressure. Under pressure, the contact area alone can not explain the observed conductivity; the potential barrier for charge injection is reduced. Based on the adhesion force *vs* applied bias dependence and current-voltage characteristics of polythiophene molecules, we conclude that characterization of electrical properties of conducting polymers using CP-AFM requires taking into account an offset in the interaction force determined by the adhesion force.

BIBLIOGRAPHY

1. Heeger, A. J. *J. Phys. Chem. B* **2001**, *105*, 8475.
2. Tamarat, P.; Maali, A.; Lounis, B. *J. Phys. Chem. B* **2000**, *104*, 1.
3. Lerch, K.; Jonas, F.; Linke, M. *J. Chim. Phys. Phys.-Chim. Biol.* **1998**, *95*, 1506.
4. Greenham, N. C.; Friend, R. H. *Solid State Physics* **1995**, *49*, 1.
5. Sotzing, G. A.; Briglin, S.; Grubbs, R. H.; Lewis, N. S. *Anal. Chem.* **2000**, *72*, 3181.
6. Chen, J.; Reed, A.; Rawlett, A. M.; Tour, J. M. *Science* **1999**, *286*, 1550.
7. Tour, J. M. *Polym. News* **2000**, *25*, 329.
8. Tour, J. M. *Acc. Chem. Res.* **2000**, *33*, 791.
9. Reed, M. A.; Zhou, C.; Muller, C. J.; Burgin, T. P.; Tour, J. M. *Science* **1997**, *278*, 252.
10. Mujica, V.; Kemp, M.; Ratner, M. A. *J. Chem. Phys.* **1994**, *101*, 6849.
11. Leatherman, G.; Durantini, E. N.; Gust, D.; Moore, T. A.; Moore, A. L.; Stone, S.; Zhou, Z.; Res, P.; Liu, Y. Z.; Lindsay, S. M. *J. Phys. Chem. B* **1999**, *103*, 4006.
12. Cui, X. D.; Primak, A.; Zarate, X.; Tomfohr, J.; Sankey, O. F.; Moore, A. L.; Gust, D.; Harris, G.; Lindsay, S. M. *Science* **2001**, *294*, 571.
13. Wold, D. J.; Frisbie, C. D. *J. Am. Chem. Soc.* **2001**, *123*, 5549.
14. Frank, S.; Poncharal, P.; Wang, Z. L.; de Heer, A. *Science* **1998**, *280*, 1744.
15. Leatherman, G. *J. Phys. Chem. B* **1999**, *103*, 4066.
16. Dai, H.; Wong, E. W.; Lieber, C. M. *Science* **1996**, *272*, 523.
17. Dorogi, M.; Gomez, J.; Osifchin, R.; Andress, R. P. A. *Phys. Rev. B* **1995**, *52*, 9071.
18. Gittins, D. I.; Bethell, D.; Schiffrin, D. J.; Nichols, R. J. *Nature* **2000**, *408*, 67.
19. Stranick, S. J.; Kamna, M. M.; Krom, K. R.; Parikh, A. N.; Allara, D. L.; Weiss, P. S. *J. Vac. Sci. Technol. B* **1994**, *12*, 2004.

20. Cygan, M. T.; Dunbar, T. D.; Arnold, J. J.; Bumm, L. A.; Shedlock, N. F.; Burgin, T. P.; Jones II, L.; Allara, D. L.; Tour, J. M.; Weiss, P. S. *J. Am. Chem. Soc.* **1998**, *120*, 2721.

21. McCarty, G. S.; Weiss, P. S. *Chem. Rev.* **1999**, *99*, 1983.

22. Muralt, P.; Pohl, D. W. *Appl. Phys. Lett.* **1986**, *48*, 514.

23. Takahashi, S.; Kishida, T.; Akita, S.; Nakayama, Y. *Jpn. J. Appl. Phys.* **2001**, *40*, 4314.

24. Fujihira, M.; Kawate, H. *J. Vac. Sci. Technol. B* **1994**, *12*, 1604.

25. Weaver, J. M. R.; Abraham, D. W. *J. Vac. Sci. Technol. B* **1991**, *9*, 1559.

26. Sugimura, H.; Hayashi, K.; Saito, N.; Takai, O.; Nakagiri, N. *Jpn. J. Appl. Phys.* **2001**, *40*, 4370.

27. O'Shea, S. J.; Atta, R. M.; Welland, M. E. *Rev. Sci. Inst.* **1995**, *66*, 2508.

28. Kelley, T. W.; Granstrom, E. L.; Frisbie, C. D. *Adv. Mater.* **1999**, *11*, 261.

29. Kelley, T. W.; Frisbie, C. D. *J. Vac. Sci. Technol. B* **2000**, *18,* 632.

30. Kelley, T. W.; Frisbie, C. D. *J. Phys. Chem. B* **2001**, *105*, 4538.

31. Loiacono, M. J.; Granstrom, E. L.; Frisbie, C. D. *J. Phys. Chem. B* **1998**, *102*, 1679.

32. Dai, H.; Wong, E. W.; Lieber, C. M. *Science* **1996**, *272*, 523.

33. Sader, J. E. *Rev. Sci. Inst.* **1999**, *70*, 3967.

34. Sader, J. E. *J. Appl. Phys.* **1998**, *84*, 64.

35. Liu, H.; Waldeck, D.; Walker, G. "Synthesis of dithiol terminated polythiophene" to be submitted.

36. Cooper, A. R. *Determination of Molecular Weight,* Wiley: New York, 1989; pp 263-300.

37. Hudlet, S.; Saint Jean, M.; Guthmann, C.; Berger, J. *Eur. Phys. J. B* **1998**, *2*, 5.

38. Belaidi, S.; Girard, P.; Leveque, G. *J. Appl. Phys.* **1996**, *81*, 1023.

39. Hao, H. W.; Baro, A. M.; Saenz, J. *J. Vac. Sci. Technol. B* **1991**, *9*, 1323.

40. Yang, Y.; Pei, Q.; Heeger, A. J. *J. Appl. Phys.* **1996**, 7*9*, 934.

41. Parker, I. D. *J. Appl. Phys.* **1994**, 75, 1656.

42. Ouisse, T. *Eur. Phys. J. B* **2001**, *22*, 415.

43. Bredas, J. L.; Street, G. B.; Themans, B.; Andre, J. M. *J. Chem Phys* **1985**, *83*, 1323.

44. Israelachvili, J. N. *Intermolecular and surface forces*, second edition; Academic press: New York, 2000; page 327.

4. FERROCENYLUNDECANETHIOL SELF-ASSEMBLED MONOLAYER CHARGING CORRELATES WITH NEGATIVE DIFFERENTIAL RESISTANCE MEASURED BY CONDUCTING PROBE ATOMIC FORCE MICROSCOPY[§]

Electrical and mechanical properties of metal-molecule-metal junctions formed between Au-supported self-assembled monolayers (SAMs) of electroactive 11-ferrocenylundecanethiol ($FcC_{11}SH$) and a Pt-coated atomic force microscope (AFM) tip have been measured using a conducting probe (CP) AFM in insulating alkane solution. Simultaneous and independent measurements of currents and bias-dependent adhesion forces under different applied tip biases between the conductive AFM probe and the $FcC_{11}SH$ SAMs revealed reversible peak-shaped current-voltage (*I-V*) characteristics and correlated maxima in the potential-dependent adhesion force. Trapped positive charges in the molecular junction correlate with high conduction in a feature showing negative differential resistance. Similar measurements on an electro-passive 1-octanethiol SAM did not show any peaks in either adhesion force or *I-V* curves. A mechanism involving two-step resonant hole transfer through the occupied molecular orbitals (MOs) of ferrocene-end groups *via* sequential oxidation and subsequent reduction, where a hole is trapped by the phonon relaxation, is proposed to explain the observed current-force correlation. These results suggest a new approach to probe charge transfer involving electroactive groups on the nanoscale by measuring the adhesion forces as a function of applied bias in an electrolyte-free environment.

[§] This work has been accepted for publication in *JACS* coauthored by Alexei V. Tivanski and Gilbert C. Walker

4.1. Introduction

Negative differential resistance (NDR), *i.e.*, a negative slope in the current-voltage (*I-V*) curve, has been observed for resonant tunneling charge transfer through metal-molecule-metal (m-M-m) junctions.[1-7] In these junctions a molecular film is typically sandwiched between two metal electrodes. Tunnel contact barriers and the weak coupling between the electronic states of the molecules and the metal electrodes indicate that charges trapped on the molecules can play a significant role in NDR,[8] but direct experimental measurement of the extent of charge trapping has been limited.[6,7]

The scanning probe microscope, where the probe serves as one of the metal electrodes in scanning tunneling microscopy (STM)[1-4] and conducting probe atomic force microscopy (CP-AFM),[5-7, 9-18] has been commonly used to form and study the electrical and structural properties of m-M-m junctions. The electronic properties of a junction are sensitive to the effects of deformation caused by the interaction force between the probe and the sample;[10-15] thus, it is valuable to measure force and current simultaneously in order to properly characterize charge transfer through molecular junctions. This can be achieved directly using CP-AFM, unlike STM where the contact force is not known nor controlled. The capability of AFM to measure precisely the contact forces between the probe and the sample surface allows independent and simultaneous measurement of the current and the contact force between the probe and the sample. CP-AFM also presents the opportunity to measure directly the electrical capacitance at an interface and hence trapped charges.

Recently, we studied electroactive polythiophene monolayers self-assembled on a gold surface.[14] By measuring the "pull-off" forces under different biases, we observed a peak in the dependence of the adhesion force as a function of bias that apparently originated from an oxidation state

change of the polymer chains under the negatively charged AFM tip. Here, we report electrical conduction measurements of electroactive m-M-m junctions formed between Au-supported self-assembled monolayers (SAMs) of 11-ferrocenylundecanethiol ($FcC_{11}SH$) and a Pt-coated AFM tip using CP-AFM in bicyclohexyl solvent. The objective is to correlate the measured currents and the bias-dependent adhesion force under different applied biases between the conductive AFM probe and the molecular film. Ferrocenylundecanethiol is chosen for several reasons. First, recent STM measurements demonstrated that similar molecules displayed NDR in STM tip/SAM/Au junctions.[1,2] In addition, $FcC_{11}SH$ molecules can be easily and reversibly oxidized under relatively small applied biases due to the presence of strong electron-donating, ferrocene end-groups, and oxidation is expected to play a significant role in NDR. We explore the extent of charge trapping within the electroactive m-M-m junctions when negative differential resistance is observed. Additionally, electric force measurements along with theoretical modeling both in and out of contact with a nonelectroactive 1-octanethiol (C_8SH) SAM were also performed.

4.2. Experimental details

All self-assembled monolayers were formed by exposing the freshly prepared Au (111) facet of a single crystalline bead[19] to 1 mM 1-octanethiol (C_8SH, Sigma-Aldrich Corp., St. Louis, MO) or 5 mM 11-ferrocenylundecanethiol ($FcC_{11}SH$, Dojindo Molecular Technologies, Inc., Gaithersburg, MD) solutions in purified (by distillation) tetrahydrofuran (THF) with soaking times between 4 and 24 hours. After assembly, samples were thoroughly rinsed in purified THF

and dried in a stream of nitrogen gas. All preparations were performed at room temperature and all samples were used within one day of preparation.

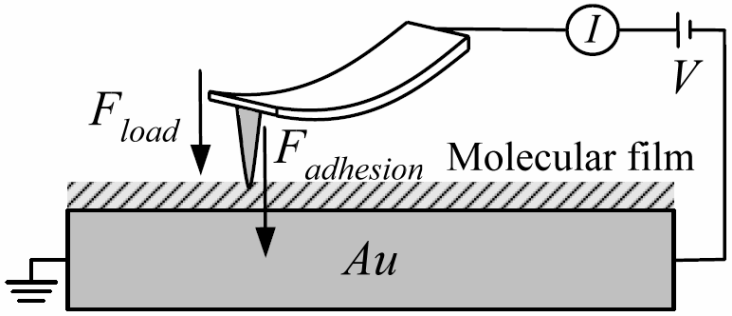

Figure 4-1 General schematic of the CP-AFM experiment used in this study.

The CP-AFM measurements (See Figure 4-1) were performed using a commercial contact mode AFM (Molecular Force Probe, Asylum Research, Santa Barbara, CA) modified in Pittsburgh for conducting probe experiments. Different fixed tip biases were applied, and currents through the junctions were measured (using a pico-ammeter, Chem-Clamp, Dagan Corp., Minneapolis, MN) as a function of vertical piezo displacement, simultaneously with independent force detection between the tip and the sample. The sample was not scanned in horizontal directions; rather the AFM tip was allowed to thermally drift over the sample surface. Measured "pull-off" forces and currents for different contact forces over different surface locations were averaged over the number of repeated measurements to obtain averaged bias-dependent adhesion forces and force-dependent current-voltage (*I-V*) characteristics of the junction. The *I-V* and *F-V* profiles were obtained by stepping the voltage in 0.05V increments, with approximately 5 second delays between successive *I* or *F* measurements. The experimental error is dominated primarily by the uncertainty in the exact number of molecules forming the junction. Because the tip drifts over

the surface, variations in the number of contacting molecules may cause fluctuations in the measured current and the adhesion force. In addition, variations in the chemical environment across the SAM surface could also introduce experimental error in both force and current measurements.

All experiments reported here were performed in an insulating bicyclohexyl solvent (99.0%, Fluka, Switzerland) in order to reduce water contamination and decrease the adhesion forces between the probe and the sample. Au and Pt-coated V-shape silicon cantilevers (MikroMash, Estonia) were used, with force constants that ranged from 0.3 to 0.5 N/m and tip radii of curvature of less than 25 nm. Cantilevers were cleaned in piranha solution (1:3 of 30% H_2O_2/98% H_2SO_4) for 5 minutes, rinsed in ultrapure water (> 18 MΩ·cm) for 1 minute, then soaked in hydrofluoric acid for 20 seconds, and finally rinsed again in ultrapure water for 1 minute followed by drying under vacuum. *Caution! Piranha solution is a very strong oxidant and is extremely dangerous to work with; gloves, goggles, and a face shield should be worn.*

In order to decrease the probable effect of tip damaging over repeated measurements, when the conduction between the tip and sample was observed to decrease under similar conditions or evolution of the force curves over repeated measurements was observed, we stopped collecting data and changed the tip. Forces higher than 30 nN were not applied due to the noticeably quick decrease in the magnitude of observed currents indicating apparent damage of the conductive coating on the tip. Depending on the coating of the tip, typically 100 to 500 force plots were collected with the same tip. All measurements were carried out at room temperature.

4.3. Bias-dependent force measurements on 1-octanethiol SAMs and models

We first describe electric force measurements and theoretical models of a tip both in and out of contact with a nonelectroactive 1-octanethiol (C_8SH) SAM. If a voltage is applied between two different conducting materials (in this case a conducting AFM tip and a conducting substrate), then an attractive electrostatic force due to the tip-sample capacitance[11,14,20] is added to the other forces experienced by the AFM probe. For the typical probe geometry, the total capacitance can be approximated as a sum of the contributions due to the tip apex, tip body, and the cantilever. The electrostatic force between the conductive cantilever body and the conductive sample system can be approximated by a parallel plate capacitor,[21] and in our case it is several pNs and has a very weak tip-sample separation dependence. Since the electrostatic forces observed here are much larger, we will neglect the electrostatic force acting on the cantilever body. The tip body resembles an inverted pyramid with a rounded tip. At very small tip-sample separations ($z < R$, where R is the tip radius of curvature and z is the tip-sample separation), the spherical tip apex provides the major contribution to the force, and an analytical expression can be obtained from the conductive sphere and a semi-infinite conductive plane model[22] while for larger tip-sample separations ($z > R$), a uniformly charged line model[23] can provide the closest description. By combining these contributions, the total capacitive force (F_{capac}) for a realistic tip shape including tip body and spherical tip apex can be approximated as

$$F_{capac} = \pi\varepsilon_0 V^2\left(\frac{R}{z} + \frac{4}{\alpha^2}\ln\left(\frac{H}{4z}\right)\right) \tag{4.1}$$

where V is the difference in potential between the probe and the sample, H is the total tip length, $\alpha=\ln[(1+\cos\theta)/(1-\cos\theta)]$, and θ is the half angle of the tip body. It is important to point out that

even in the absence of an applied potential, a capacitance force may still exist due to the contact potential difference between different materials.[24]

The presence of a thin organic layer of high dielectric constant grafted on the conductive substrate should not strongly modify the capacitive forces assuming that the electrostatic field in the dielectric material is much weaker than that in the solution space between the conductive probe and the conductive surface. Thus, in order to take into account the organic film, it suffices to replace tip-sample separation (z) in Equation 4.1 by an effective distance $z+d/\varepsilon_r$, where d and ε_r are the thickness and the dielectric constant of the organic film, respectively. With respect to the experimental force plots, the tip-sample separation measured by AFM is between the probe and the organic film, yet the relevant tip-sample separation in the capacitive forces is between the probe and the substrate on which the molecular film is grafted.

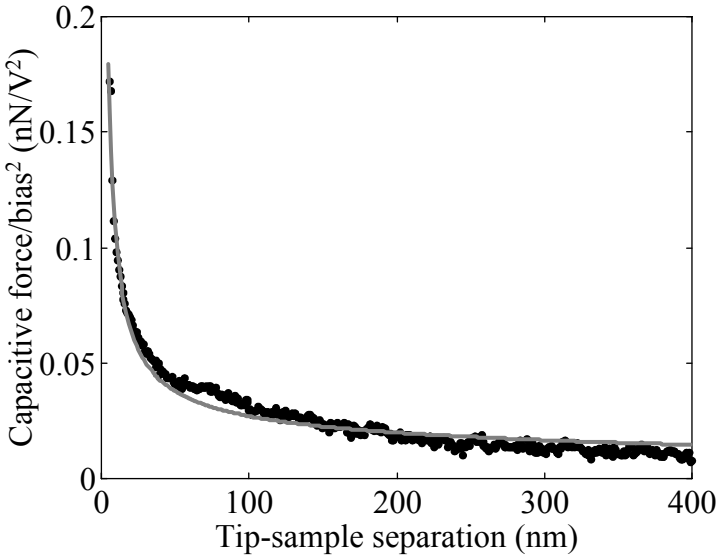

Figure 4-2 The averaged capacitive force (●) between a Au-coated tip and a C_8SH monolayer normalized by the square of tip bias is shown as a function of tip-sample separation. The solid gray line represents the best fit using the analytical expression in Equation 4.1.

Equation 4.1 suggests that non-contact attractive capacitive forces have a parabolic dependence upon the applied tip bias. For the Au-coated AFM probe over a C_8SH SAM in bicyclohexyl solvent, all force dependencies were overlapped very closely after normalizing all experimental non-contact capacitive forces with square applied biases, confirming the parabolic bias dependence. The averaged normalized non-contact capacitive force (•) as a function of tip-sample separation is shown in Figure 4-2. The zero force was selected as the force when the tip was far away (~ 500 nm) from the surface.

From Equation 4.1, an analytical expression for the capacitive non-contact attractive force can be compared with the experimental results. Since the real dimensions for the Au-coated AFM tip used in these experiments are not known precisely, a total length, half angle, and apex radius were used as free fit parameters. The solid gray line in Figure 4-2 shows the best fit by the model of the non-contact capacitive force as a function of the tip-sample separation. The fit indicates a half angle $\theta = 10.3 \pm 0.2°$, a tip radius of curvature $R = 27 \pm 0.4$ nm, and a total length of the tip $H = 22 \pm 2$ μm, which are all close to the manufacturer's reported values (15°, < 40 nm and 20 μm, respectively). The thickness of the C_8SH SAM was estimated as 1.04 nm from molecular length, as obtained from semiempirical calculations using the PM3 method, and a relative dielectric constant was taken to be 2. Reasonably good agreement between the theoretical and experimental results suggests that the long-range non-contact attractive forces acting on the conductive probe over a C_8SH SAM can be described using the analytical expression in Equation 4.1.

Using our definition of the adhesion force as the "pull-off" force relative to the zero force when the tip is far away from the surface, the experimentally measured, bias-dependent adhesion force between the Au-coated AFM probe and the C_8SH monolayer can be plotted as a function of the

applied tip bias. Bias-dependent adhesion forces were obtained by averaging over more than one thousand repeated measurements of "pull-off" forces under different tip biases with the tip contacting different surface spots of the SAM. Due to the fact that the bias-dependent adhesion forces in this case were fully symmetric for both tip bias polarities, the experimentally obtained adhesion force is shown in Figure 4-3 (•) as a function of the absolute tip bias. Each data point shown in Figure 4-3 represents the mean value of bias-dependent adhesion force for a series of ~30 repeated measurements under a particular bias; the standard deviation of the mean is typically smaller than the size of the printed point.

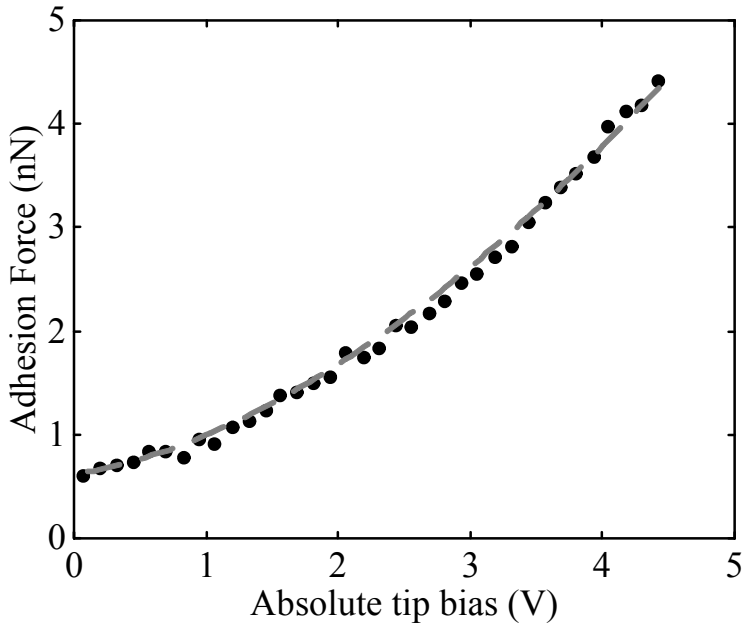

Figure 4-3 The experimental (•) and theoretical (gray dashed line) bias-dependent adhesion force between the Au-coated probe and the C_8SH SAM in bicyclohexyl solvent is shown as a function of absolute tip bias.

In order to calculate the bias-dependent adhesion force between the conductive probe and the sample, the bias-dependent tip-sample separation (z_{off}) at which the tip jumps away from the surface must be estimated. This event occurs when the gradient of interaction force becomes less or equal to the spring constant of the cantilever. This distance can be determined from the following equation

$$-\frac{dF_{capac}(z,V)}{dz} = k_c \tag{4.2}$$

where k_c is the spring constant of the cantilever. By substituting Equation 4.1 into Equation 4.2, one obtains Equation 4.3 which is an analytical expression for the bias-dependent tip-sample separation at which the tip jumps away from the surface.

$$z_{off} = d/\varepsilon_r + |V|\sqrt{\pi\varepsilon_0 R/k_c} \tag{4.3}$$

Here, the gradient of interaction force due only to the spherical tip apex contribution was considered, since the gradient of force due to the tip body was negligible. By substituting Equation 4.3 back into Equation 4.1, the theoretically predicted dependence of the adhesion force as a function of applied tip bias can be written as

$$F_{adh}(V) = \pi\varepsilon_0 V^2\left(\frac{R}{d/\varepsilon_r + |V|\sqrt{\pi\varepsilon_0 R/k_c}} + \frac{4}{\alpha^2}\ln\left(\frac{H}{4\left(d/\varepsilon_r + |V|\sqrt{\pi\varepsilon_0 R/k_c}\right)}\right)\right) \tag{4.4}$$

The first term in Equation 4.4 represents the spherical tip apex contribution, and the second term provides the contribution from the tip body to the bias-dependent adhesion force. The intrinsic adhesion force of 0.62 nN (determined at 0 V applied tip bias) has been added to the calculated dependence. Excellent agreement between the theoretical (gray dashed line in Figure 4-3) and experimental results suggests that the bias-dependent adhesion forces between the conductive probe and nonelectroactive C_8SH SAM can be described using the analytical expression in

Equation 4.4. This agreement is especially noteworthy since the fitted values of the tip dimensions obtained from the non-contact capacitance model were used to make this theoretical prediction of the adhesion force. No additional fitting was required.

4.4. Bias-dependent force and current measurements on electroactive 11-ferrocenylundecanethiol SAMs

Unlike C_8SH molecules, $FcC_{11}SH$ molecules can be easily and reversibly oxidized under relatively small applied biases due to the presence of strong electron-donating, ferrocene end-groups. m-M-m junctions were formed between Au-supported SAMs of electroactive $FcC_{11}SH$ and a Pt-coated AFM tip. As done for C_8SH, experimental measurements and data analyses were made for the non-contact bias-dependent capacitive forces to determine the Pt-coated tip radius of curvature; R = 11 ± 0.5 nm. The contact potential difference between Au and Pt materials was found to be V_r = 0.45 ± 0.05 V, which corresponds well to the difference in the work functions of Au (5.2 V) and polycrystalline Pt (5.65 V). The thickness of the $FcC_{11}SH$ SAM and the relative dielectric constants were taken to be 2.37 nm and 2, respectively.[25] The non-contact capacitive force results were consistent with those obtained for the Au-coated tips over C_8SH monolayers and were well described using our capacitive force model.

In the same way as for C_8SH, experimental measurements and data analyses were performed for the bias-dependent adhesion force. Figure 4-4 shows the measured adhesion forces (points with error bars as the mean and the standard deviation of a series of ~20 repeated measurements under a particular bias) between the Pt-coated AFM probe and the $FcC_{11}SH$ SAM in bicyclohexyl solvent as a function of applied tip bias. Bias-dependent adhesion forces were obtained by averaging over hundreds of repeated measurements of "pull-off" forces under different tip biases

with the tip contacting different surface regions of the SAM. Bias magnitudes higher than 3 volts were not applied in order to avoid high currents passing from the conductive probe to the conductive substrate, which might irreversibly damage the monolayer. The theoretically predicted dependence (dashed gray line) was plotted using Equation 4.4 with fitted parameters obtained from the non-contact capacitive force measurements, and no additional adjustment of the parameters was performed. The intrinsic adhesion force of 0.35 nN has been added to the calculated dependence.

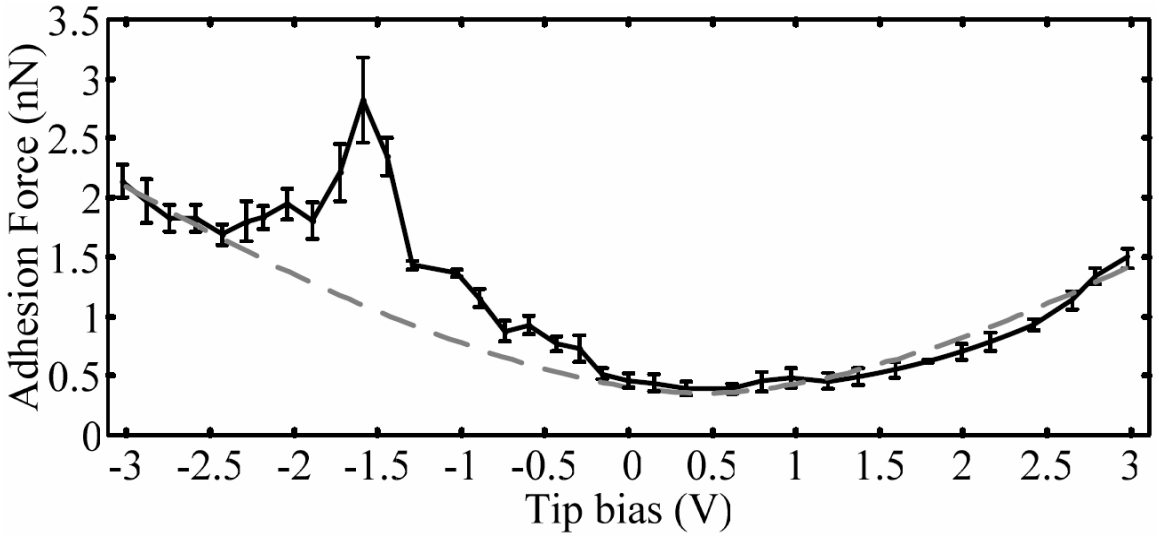

Figure 4-4 Experimental (points with error bars) and theoretical (dashed gray line) bias dependent adhesion forces between the Pt-coated probe and the $FcC_{11}SH$ SAM in bicyclohexyl solvent, as a function of the applied tip bias. The error bars represent the standard deviation of the mean for a series of ~20 repeated measurements under a particular bias.

As can be seen in Figure 4-4, the experimental dependence of the bias-dependent adhesion force in the negative bias region clearly deviates from the theoretical dependence in the bias region between –0.2 V and –2.4 V while the experimental data in the positive tip bias region closely

follow calculated dependence. The approximate maximum of the adhesion deviation peak is around -1.6 ± 0.12 V (with a peak width at half maximum of about 0.5 ± 0.1 V) with a magnitude of 1.7 ± 0.4 nN greater than the theoretical dependence. Noteworthy, this result is significantly different from measurements on the nonelectroactive C_8SH SAM where the experimental dependence of the adhesion forces closely follows the theoretically calculated dependence for both tip bias polarities. It is important to mention that in our previous measurements on a Au-coated AFM tip/1,4 benzene dimethanethiol SAM/Au substrate junction,[14] which is not expected to undergo redox transitions in this range of applied biases, no deviation from theoretically predicted behavior was observed as well. However, our CP-AFM measurements on electroactive conjugated polythiophene monolayers, sandwiched between two gold electrodes, did produce an apparent peak in addition to the expected theoretical dependence.[14] This indicates that deviation in the bias-dependent adhesion force is observable regardless of the electrode materials (at least for gold and platinum). Since the observed bias-dependent adhesion force deviation over calculated dependence is positive and the terminal ferrocene groups can be easily oxidized to ferricenium cations (Fc^+), we hypothesize that the adhesion force peak in Figure 4-4 arises from attractive Coulomb interactions between the negatively charged AFM tip and the terminal Fc^+ cations.

In order to see if there is a correlation between the measured current and the adhesion force in the negative bias region that could help to explain the origin of the observed adhesion force deviation, electrical conduction measurements were performed under different applied negative tip biases. In this way the current through the junction was measured as a function of tip-sample separation simultaneously with independent detection of the force between the tip and the sample. Force dependent current-voltage (*I-V*) characteristics of the junction were obtained by

averaging over hundreds of repeated measurements under different tip biases with the tip contacting different surface spots of the SAMs.

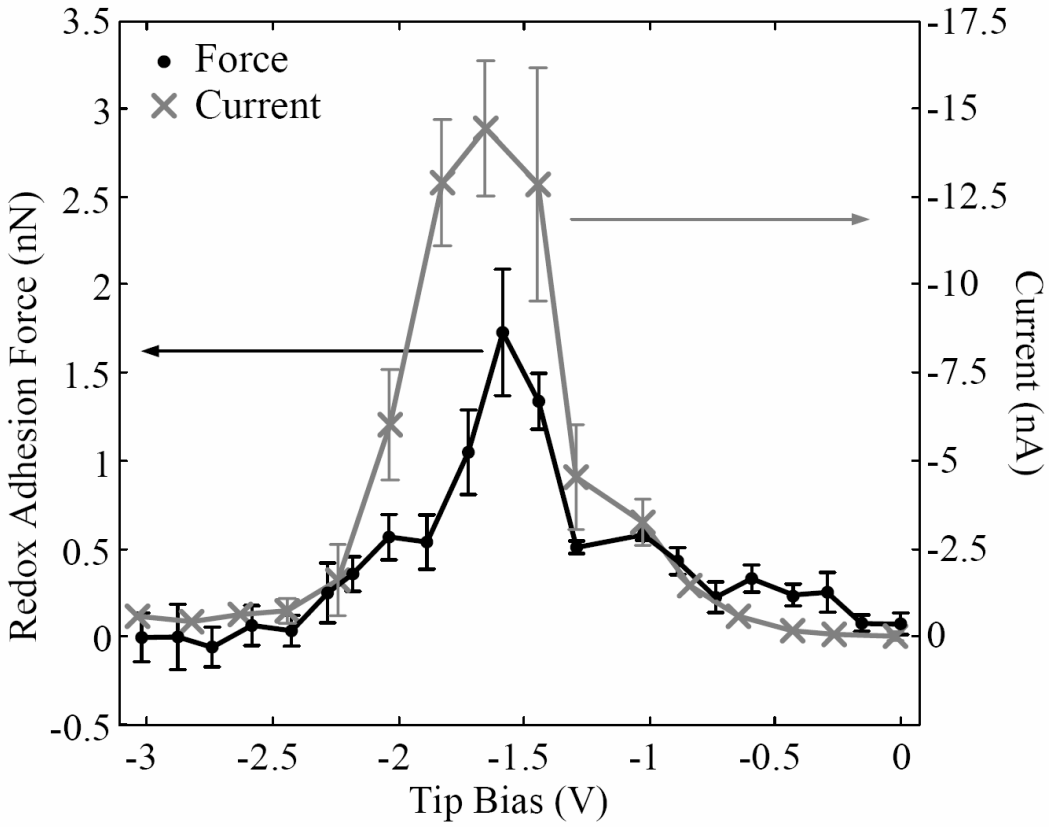

Figure 4-5 The redox adhesion force (•) and current (x) between the Pt-coated probe and the $FcC_{11}SH$ SAM are shown as a function of the applied tip bias under an interaction force of 5 nN. The error bars represent the standard deviation of the mean.

Figure 4-5 shows the averaged current (x) of the $FcC_{11}SH$ SAM in bicyclohexyl solvent under a fixed interaction force of 5 nN; error bars represent the standard deviation of the mean for a series of repeated measurements. The interaction or net force between the tip and underlying film at their contact is considered to be equal to the sum of the loading, intrinsic, and capacitance forces. This interaction force was employed to ensure that a sufficient electrical contact between

the conductive probe and the sample is achieved, yet there is no significant monolayer deformation and/or penetration of the tip into the SAM.[18] The averaged peak-shaped *I-V* characteristic is obtained in the negative tip bias region. No peak-shaped current dependence was observed in the positive bias region between 0 and +3 V where current was increasing monotonically with applied bias (not shown). This is consistent with absence of deviation in the adhesion force dependence for the same positive bias range.

As can be seen in Figure 4-5, an averaged negative differential resistance (NDR) peak, *i.e.*, a negative slope in the *I-V* curve, is observed near -1.65 ± 0.18 V (and peak width at half maximum of 0.6 ± 0.15 V) with a peak-to-valley ratio (PVR). It is important to mention that Figure 4-5 was obtained by quasistatic measurements, and not by rapidly sweeping the voltage. The NDR peak position observed here is in excellent agreement with recent STM measurements in dodecane solvent for similar molecules where a peak positioned at -1.6 ± 0.15 V was observed;[1,2] the peak width, however, was approximately four times narrower than that observed here. The reason for this deviation is unclear. However, one possibility may originate from the fact that unlike STM measurements, in CP-AFM, currents are measured with the tip directly contacting the sample. Since the tip drifts over the surface, variations in the number of contacting molecules and in the chemical environment across the SAM surface between measurements could cause fluctuations in the measured current and in the NDR peak position.

The observed *I-V* characteristics were linear within ± 0.2 volts bias range. Figure 4-6 shows the averaged *I-V* characteristic in the low-bias range of applied tip biases for the $FcC_{11}SH$ SAM (●) in bicyclohexyl solvent under a fixed interaction force of 5 nN. Ohmic dependences observed in the *I-V* curves are consistent with the Simmons model in the low-bias region[26,27] for nonresonant tunneling through a m-M-m interface. The linear portion of the *I-V* curve was fit by a straight

line, (See Figure 4-6) and the obtained slope was used to determine the junction resistance. From the fit, the junction resistance for a $FcC_{11}SH$ SAM was 25 ± 2 GΩ.

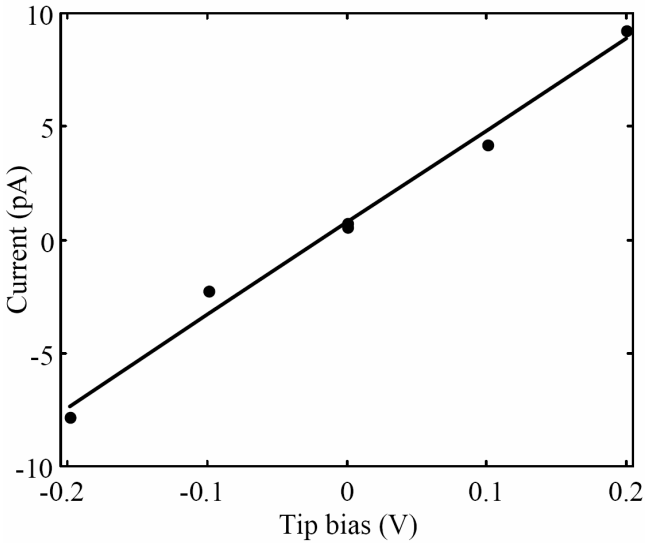

Figure 4-6 The current (•) between the Pt-coated probe and the $FcC_{11}SH$ SAM and the linear fit is shown as a function of the applied tip bias in the low-bias region under an interaction force of 5 nN.

In order to compare the measured current and the adhesion force, the calculated adhesion dependence was subtracted from the measured bias-dependent adhesion force, and we thus obtained the deviation force, which we define here as the redox adhesion force. Figure 4-5 plots the redox adhesion force (•) and the current (x) between the Pt-coated AFM probe over the $FcC_{11}SH$ SAM under the interaction force of 5 nN as a function of applied tip bias. By comparing current and redox adhesion force dependencies shown in Figure 4-5, it is apparent that, within experimental uncertainty, the biases corresponding to the peak positions in both the bias-dependent adhesion force and the current are the same; also the shape of both curves appears to be similar with the peak width at half maximum of the redox adhesion force

somewhat narrower than that of the current. The correlation between independent measurements of peak-shaped redox adhesion force and current lead us to the conclusion that the mechanisms leading to the observed NDR in current and the peak in the bias-dependent adhesion force should be coupled.

4.5. Molecular orbitals and peak-shaped current and adhesion force dependencies

The relative positions of Fermi energy levels of connecting electrodes and the highest occupied molecular orbital (HOMO) or the lowest unoccupied molecular orbital (LUMO) of the sandwiched molecules is one of the most important factors in understanding charge transport through m-M-m junctions. When the difference between the HOMO (LUMO) and the mean Fermi energy of metal electrodes is large, charge transport through an m-M-m interface under relatively small applied biases is expected to be coherent nonresonant tunneling. In the case of large applied biases, the Fermi energy level can approach the energy of molecular orbitals (MOs) and resonant transition through or in molecular electronic states may take place. For the C_8SH SAM, the molecular HOMO-LUMO gap is quite large (~8 eV) which implies that the charge transfer under relatively small applied biases is primarily dominated by the above mechanism while under higher biases, electrical breakdown of the molecular film would most likely occur before reaching the energy of MOs. Unlike C_8SH molecules, terminal ferrocene (Fc) groups of $FcC_{11}SH$ have redox-accessible states that lie within an eV of the mean Fermi level of metal electrodes implying that molecular states can be probed under relatively small applied biases without causing electrical breakdown of the film. The exact energies of these electronic states relative to the mean Fermi level of metal electrodes are not straightforward to estimate in a solid

environment and in the absence of potential control and a supporting electrolyte, so we are hesitant to provide a more quantitative analysis without further experiments and theoretical computations.

The present m-M-m junction architecture can be considered as localized discrete electronic levels of electroactive Fc groups that are weakly coupled to both metal electrodes and separated from them by two thin insulating metal/molecule junction barriers, the alkylthiolate-S interface[28] on the substrate end and the Pt-coated AFM tip/SAM interface[9] on the other end. The overall tunnel junction is noticeably asymmetrical due to the difference between the metal/electrode contacts: strong chemical bonding S-Au contacts on the substrate side and weak nonbonded (mechanical) AFM tip/ferrocenes contacts on the other side of the molecules.[9] This implies that most of the voltage drop occurs at the AFM tip/molecules interface, and under this consideration, the application of voltage would generally move the Fermi energy of the tip relative to the molecular levels more than those levels shift with respect to the Fermi energy of supporting Au substrate. Similar descriptions have been presented before for both STM and AFM measurements of redox-active moieties.[6,7,29] In this approximation, additional current is expected for the region of applied biases where narrow features in the local density of states (LDOS) of the tip apex couples with the electronic levels of ferrocenes.[30] As larger bias magnitudes are applied, coupling between the tip and the Fc electronic levels decreases, leading to a decrease in the observed current magnitude. Hence, a NDR peak in *I-V* curve is expected with the peak width primarily determined by the extent of localization in the LDOS of the tip apex. We note that the exact LDOS of the tip apex is expected to change with repeated contact of the tip with the surface. Considering the difference in molecules/electrodes contacts employed here and the fact that calculated narrow features in the LDOS of the sufficiently sharp

Pt-coated tip apex lie below the mean Fermi level of metal electrodes, NDR should occur only at the negative tip bias.[30] This expectation is consistent with our experimental observation that no peak-shaped current dependence was observed in the positive bias region between 0 and +3 V.

The nature of charge transfer through the molecular states that leads to the observed NDR for the region of applied biases where narrow features in the LDOS of the tip apex couple with molecular levels can, in principle, be described by both one-step resonant tunneling[1-7] and two-step reduction/oxidation[8,31] processes. In the resonant tunneling mechanism, charge transfer results from the charge tunneling through appropriate molecular levels without occupying them.[4,32] The molecules themselves do not attain a charge over a time scale comparable to the phonon relaxation time. While this process can, in principle, describe the peak-shaped current observed here, it can not adequately explain the origin of the peak in the bias-dependent redox adhesion force.

Unlike one-step charge transfer, in the reduction/oxidation mechanism, charge transfer occurs *via* sequential oxidation and subsequent reduction of electroactive terminal ferrocenes where charge is temporarily trapped by the phonon relaxation. Since the forces observed in the redox adhesion force *versus* bias dependence are attractive and ferrocene-end groups are strong electron-donors and LDOS of the tip apex lie below the mean Fermi level of metal electrodes, we argue that charge transfer primarily occurs through and in the HOMO of the Fc molecules. Though non-reversible change of the ferrocenylundecanethiol monolayer cannot be completely ruled out, we note that repeated measurements in the same area showed the same result on the second measurement, within experimental error.

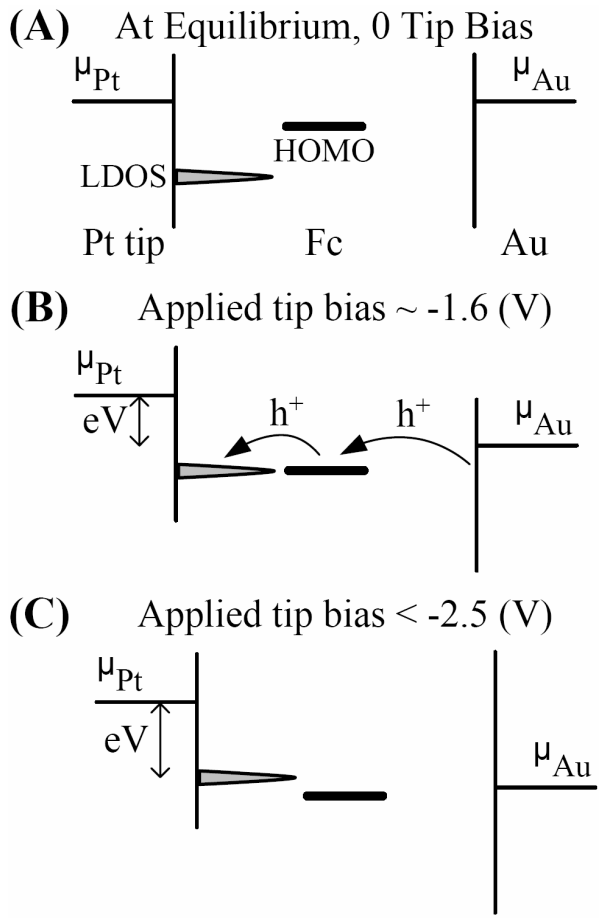

Figure 4-7 A Schematic of how the LDOS of the tip apex could float relative to the HOMO of Fc under negative bias. A) At equilibrium, $\mu_{tip}=\mu_{Au}$; B) At a negative tip bias corresponding to the perfect alignment of the LDOS with the HOMO, hole transfer via sequential oxidation and subsequent reduction would lead to the maxima in both additional current and in the number of trapped positive charges; C) At more negative tip biases, the LDOS would move away from alignment leading to a decrease in current.

The proposed mechanism for NDR and peak-shaped redox adhesion force based on the oxidation/reduction mechanism is shown schematically in Figure 4-7. The bias is applied to the tip and the electrochemical potential of the gold substrate μ_{Au} is taken as energy reference. Figure 4-7A illustrates an equilibrium energy diagram with zero applied bias where the electrochemical potentials of the substrate and the tip are the same. The narrow features in the LDOS of the tip apex lie below the HOMO of Fc, and without alignment charge transport is

primarily *via* nonresonant tunneling and no additional current is expected. As negative tip biases are applied, LDOS sweep closer to the HOMO level, and Figure 4-7B shows the relative energy levels under such negative tip bias when the narrow features in the LDOS of the tip apex align well with the HOMO of Fc, providing the largest coupling.

Hole transfer is first from the gold substrate to the HOMO level of Fc which oxidizes the molecule; the hole is temporarily trapped by the phonon relaxation of the molecular level to its new equilibrium configuration. A thermal fluctuation then allows subsequent hole tunneling from the molecular level of the molecule to the tip, returning the molecule to its neutral state. The largest coupling between the narrow features in the LDOS of the tip apex and the HOMO molecular level leads to the maxima in both additional current and in the number of trapped positive charges. In this configuration the negatively charge tip provides a stabilizing electric field for the formation of ferricenium cations, similarly to counter ions in an electrolyte solution. This is consistent with our observation that when the tip is removed from surface contact for ~5 seconds time delay between every measurement, no deviation from theoretical dependence was observed in the non-contact capacitive force for both tip bias polarities. This implies that the interface is not charged and that those cations are stable for less than several seconds. As more negative tip biases are applied, coupling between the narrow features in the LDOS of the tip apex and the HOMO molecular level decreases (See Figure 4-7C), moving the interface away from resonance and leading to a decrease in both current magnitude and number of cations, hence decrease in the redox adhesion force. We next address the extent of interface charging.

4.6. Number of trapped charges generated under the negatively biased tip

The force dependent number of molecules forming the junction can be estimated from the contact area using a Hertzian elastic contact model with the adhesion force between the probe and sample included.[33] The contact area, a^2, between a spherical tip of radius R penetrating into a uniform elastic film may be estimated as

$$a^2 = \left(\frac{FR}{K}\right)^{2/3} \tag{4.5}$$

where F is the interaction force and K is an effective modulus equaling $(4/3)[(1-\nu^2_t)/E_t+(1-\nu^2_s)/E_s]^{-1}$ (E_s, ν_s, E_t, ν_t are Young's modulus and Poisson's ratio of the sample and Pt-coated AFM tip, respectively). The Poisson ratio for most materials is between 0.25 and 0.5 and hence, assuming $\nu_t \sim \nu_s \sim 0.33$, an effective modulus can be approximated as $K=1.5E_tE_s/(E_t+E_s)$. Although measured values for elasticity modulus are not available, assuming E_t=170 GPa[34] and E_s=7 GPa,[35] the contact area for the maximum applied interaction force of 20-30 nN would be 7.8 - 10.2 nm^2. The surface coverage for a closely packed $FcC_{11}SH$ SAM is about 2.5 molecules/nm^2,[36] thus there are about 20-25 molecules in direct contact between the AFM tip and the substrate under 20-30 nN interaction force.

The deviation magnitude of 1.7 ± 0.4 nN observed in the bias-dependent adhesion force dependence may be used to estimate the total trapped charge Q. The additional attractive force arises from Coulomb interactions between the stored charge and its image charges in the tip and Au substrate. Using a simple parallel-plate geometry[37] and assuming that stored charge is localized on the ferrocene end-groups, the quantity of detected charges is Q = 80 ± 20 positive elementary charges or the same number of oxidized molecules if we assume each molecule can

store one charge. We note that the obtained number of charges is 3-4 times higher than the maximum number of molecules (20-25) in direct contact with the AFM tip. This is reasonable given that the field extends beyond the region of contact, which could enable the lateral migration of charges. It is also possible that the parameters used in the above model overestimate the amount of charge and/or underestimate the number of molecules. Since measured values for elasticity modulus are not available, if we were to consider Es = 1 GPa instead of 7 GPa as used above, we would estimate that there are about 72-110 molecules in direct contact between the AFM tip and the substrate under 20-30 nN interaction force, reasonably close to ~80 positive elementary charges obtained above.

4.7. Conclusions

We have presented a method to measure charge within a molecular circuit that shows negative differential resistance *via* conducting probe atomic force microscopy. This has been facilitated by using a prototypical redox species, ferrocene, in a metal-molecule-metal junction. We observed that the voltage region over which conduction was enhanced correlated strongly with the region over which the scanning probe tip experienced capacitive attraction to the surface. A model for the capacitance force shows that the force originates primarily at the apex of the tip, and the bias dependence indicates that the trapped charges are holes. The number of charged ferrocenylundecanethiol molecules appears to exceed the number that is in direct mechanical contact with the tip when current flows.

BIBLIOGRAPHY

1. Gorman, C. B.; Carroll, R. L; Fuierer, R. R. *Langmuir* **2001**, *17*, 6923.

2. Wassel, R. A.; Credo, G. M.; Fuierer, R. R.; Feldheim, D. L.; Gorman, C. B. *J. Am. Chem. Soc.* **2004**, *126*, 295.

3. Tao, N. J. *Phys. Rev. Lett.* **1996**, *76*, 4066.

4. Han, W.; Durantini, E. N.; Moore, T. A.; Moore, A. L.; Gust, D.; Rez, P.; Leatherman, G.; Seely, G. R.; Tao, N.; Lindsay, S. M. *J. Phys. Chem. B* **1997**, *101*, 10719.

5. Rawlett, A. M.; Hopson, T. J.; Nagahara, L. A.; Tsui, R. K.; Ramachandran, G. K.; Lindsay, S. M. *Appl. Phys. Lett* **2002**, *81*, 3043.

6. Fan, F. F.; Yang, J.; Cai, L.; Price, Jr., D. W.; Dirk, S. M.; Kosynkin, D. V.; Yao, Y.; Rawlett, A. M.; Tour, J. M.; Bard, A. J. *J. Am. Chem. Soc.* **2002**, *124*, 5550.

7. Fan, F. F.; Yao, Y.; Cai, L.; Cheng, L.; Tour, J. M.; Bard, A. J. *J. Am. Chem. Soc.* **2004**, *126*, 4035.

8. Kuznetsov, A. M.; Sommer-Larsen, P.; Ulstrup, J. *Surf. Sci.* **1992**, *275*, 52.

9. Cui, D.; Zarate, X.; Tomfohr, J.; Sankey, O. F.; Primak, A.; Moore, A. L.; Moore, T. A.; Gust, D.; Harris, G.; Lindsay, S. M. *Nanotechnology* **2002,** *13*, 5.

10. Gomar-Nadal, E.; Ramachandran, G. K.; Chen, F.; Burgin, T.; Rovira, C.; Amabilino, D. B.; Lindsay, S. M. *J. Phys. Chem. B* **2004**, *108*, 7213.

11. Leatherman, G.; Durantini, E. N.; Gust, D.; Moore, T. A.; Moore, A. L.; Stone, S.; Zhou, Z.; Rez, P.; Liu, Y. Z.; Lindsay, S. M. *J. Phys. Chem. B* **1999**, *103*, 4006.

12. Wold, D. J.; Frisbie, C. D. *J. Am. Chem. Soc.* **2001**, *123*, 5549.

13. Lee, T.; Wang, W.; Klemic, J. F.; Zhang, J. J.; Su, J.; Reed, M. A. *J. Phys. Chem. B* **2004**, *108*, 8742.

14. Tivanski, A. V.; Bemis, J. E.; Akhremitchev, B. B.; Liu, H.; Walker, G. C. *Langmuir* **2003**, *19*, 1929.

15. Tivanski, A. V.; He, Y.; Borguet, E.; Liu, H.; Walker, G. C.; Waldeck, D. H. *J. Phys. Chem. B* **2005**, *109*, 5398.

16. Ishida, T.; Mizatani, W.; Aya, Y.; Ogiso, H.; Sasaki, S.; Tokumoto, H. *J. Phys. Chem. B* **2002**, *106*, 5886.

17. Suganuma, Y.; Trudeau, P. -E.; Dhirani, A. –A. *Phys. Rev. B* **2002**, *66*, 241405.

18. Tivanski, A. V.; Walker, G. C. submitted for publication to *Langmuir*

19. Clavilier, J. F.; Guinet, G.; Durand, R. *J. Electroanal. Chem.* **1980**, *107*, 205.

20. Cui, X. D.; Zarate, X.; Tomfohr, J.; Primak, A.; Moore, A. L.; Moore, T. A.; Gust, D.; Harris, G.; Sankey, O. F.; Lindsay, S. M. *Ultramicroscopy* **2002**, *92*, 67.

21. Y. Martin, D. W. Abraham, H. K. Wrickramasinghe, *Appl. Phys. Lett.* **1988**, *52*, 1103.

22. B. D. Terris, J. E. Stern, D. Rugar, H. J. Mamin, *Phys. Rev. Lett.* **1989**, *63*, 2669.

23. H. W. Hao, A. M. Baro, J. J. Saenz, *Vac. Sci. Technol B* **1991**, *9*, 1323.

24. Hudlet, S.; Saint Jean, M.; Guthmann, C.; Berger, J. *Eur. Phys. J. B* **1998**, *2*, 5

25. Ohtsuka, T.; Sato, Y.; Uosaki, K. *Langmuir* **1994**, *10*, 3658.

26. Simmons, J. H. *Appl. Phys.* **1963**, *281*, 1793.

27. Sze, S. M. *Physics of Semiconductor Devices*, *John Wiley &Sons, Inc.*, New York, **1981**.

28. Seminario, J. M.; De La Cruz, C. E.; Deroza, P. A. *J. Am. Chem. Soc.* **2001**, *123*, 5616.

29. Snyder, S. R.; White, H. S.; *J. Electroanal. Chem.* **2001**, *393*, 177.

30. Xue, Y.; Datta, S.; Hong, S.; Reifenberger, R.; Henderson, J. I.; Kubiak, C. P. *Phys. Rev. B* **1999**, *59*, R7852.

31. Mazur, U.; Hipps, K. W. *J. Phys. Chem.* **1995**, *99*, 6684.

32. Schmickler, W. J. *J Electroanal. Chem.* **1992**, *336*, 213.

33. Weihs, T. P.; Nawaz, Z.; Jarvis, S. P.; Pethica, J. B. *Appl. Phys. Lett.* **1991**, *59*, 3536.

34. Burnham, N, A.; Colton, R. J. *J. Vac. Sci. Technol. A* **1989**, *7*, 2906.

35. Joyce, A.; Thomas, R. C.; Houston, J. E.; Michalske, T. A.; Crooks, R. M. *Phys. Rev. Lett.* **1992**, *68*, 2790.

36. Chidsey, C. E. D.; Bertozzi, C. R.; Putvinski, T. M.; Mujsce, A. M. *J. Am. Chem. Soc.* **1990**, *112*, 4301.

37. Schaadt, D. M.; Yu, E. T.; Sankar, S.; Berkowitz, A. E. *Appl. Phys. Lett.* **1999**, *74*, 472.

5. CONJUGATED THIOL LINKER FOR ENHANCED ELECTRICAL CONDUCTION OF GOLD-MOLECULE CONTACTS[§]

Single-molecule electrical conduction studies are used to evaluate how the molecular linking unit influences the tunneling efficiency in metal-Molecule-metal (m-M-m) junctions. This work employs conductive probe atomic force microscopy (CP-AFM) to compare the molecular conduction of two π-bonded molecules, one with a single thiol linker and another with a conjugated double thiol linker at both ends of the molecules. The results demonstrate that the molecule with the conjugated double thiol linkers displays higher conduction in Au-molecule-Au junctions than the non-conjugated single thiol-Au contacts.

5.1. Introduction

In recent years, improving the electrical conduction of molecular wires by using conjugated molecules has been a major focus in molecular electronics. As the conduction of the molecule becomes very large however, the metal-Molecule-metal (m-M-m) contacts can dominate the response. Recent experimental[1-9] and theoretical[10-15] work has demonstrated the importance of metal-molecule contacts to the efficiency of charge transfer through m-M-m junctions. Particularly, for alkanethiol-based junctions, metal-molecule contact resistance decreased up to two orders of magnitude when chemical bonding contacts were used instead of nonbonded

[§] This work has been originally published as Tivanski, A. V.; He, Y.; Borguet, E.; Liu, H.; Walker, G. C.; Waldeck, D. H. *J. Phys. Chem. B* **2005**, *109*, 5398-5402.

(mechanical) contacts.[1] Unlike electrical conduction studies on saturated molecules, fewer experimental studies address how the contacts effect conduction through conjugated molecular systems. This work demonstrates that the efficiency of charge transport through π-bonded molecules forming m-M-m junctions with thiol linking units between metals and the molecule can be improved by the use of conjugated double thiol linkers at both ends of the molecule. This knowledge should be useful for the design and fabrication of more efficient electrical and optical devices with potential use in molecular electronics.

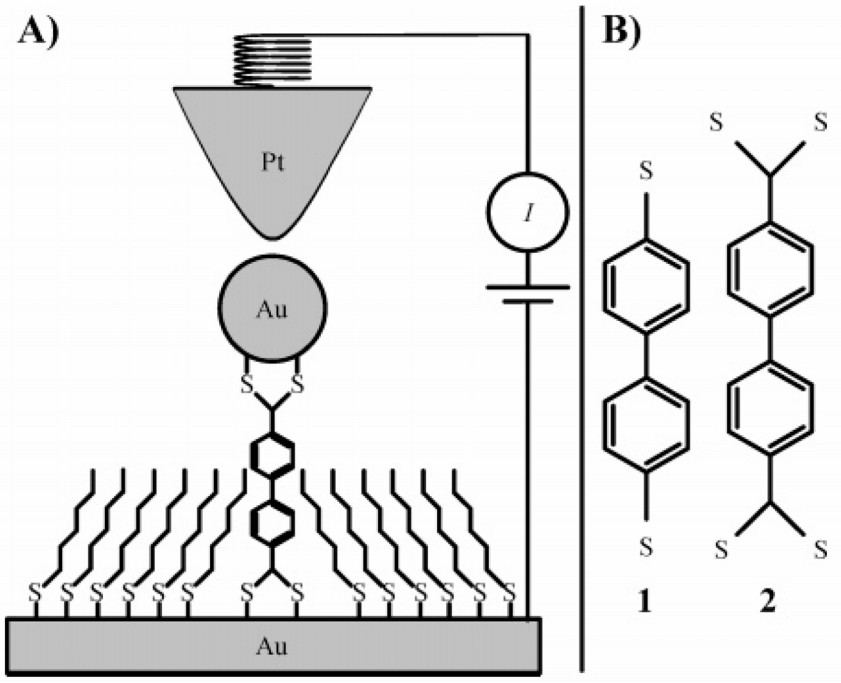

Figure 5-1 A). Schematic of the CP-AFM experiment. B). Molecular structures of the molecules that are compared in this study.

This work compares electrical conduction measurements for gold-molecule-gold tunnel junctions containing two different types of gold-molecule contacts: single Au-S-Ar-S-Au and double Au-

S_2C-Ar-CS_2-Au contacts at both ends of the molecule, where Ar is a biphenyl moiety. The Au-S_2C-Ar-CS_2-Au contacts are postulated to provide two points of contact with each Au electrode and better conjugation to the molecule's π system than the single Au-S-Ar-S-Au contact. The junctions are formed using conducting probe atomic force microscopy (CP-AFM)[16] in which a Pt-coated AFM probe serves as the contact to the gold nanoparticle electrode and the other electrode is a gold substrate on which the conducting molecules have been assembled (See Figure 5-1A). Measurements were performed on samples containing isolated conducting molecules in self assembled monolayers (SAMs) of nonconductive molecules that were prepared using an insertion process.[17] Conduction measurements were performed on single molecules in order to avoid the uncertainty in the exact number of conducting molecules forming a junction. Good electrical contact between the conductive AFM probe and the conducting molecule was achieved by covalently attaching gold nanoparticles to the exposed sulfur groups of the molecules.[2] The two molecules compared in this study are biphenyl-4,4'-dithiol (**1**) and biphenyl-4,4'-dicarbodithioic acid (**2**) (See Figure 5-1B).

5.2. Experimental Section

All 1-hexanethiol (C_6, Sigma-Aldrich Corp., St. Louis, MO) self-assembled monolayers (SAMs) were formed by exposing the freshly prepared Au (111) facet of a single crystalline bead[18] to 1 mM C_6 solution in ethanol for about two days and then were rinsed in ethanol and dried in a stream of nitrogen gas. The biphenyl-4,4'-dicarbodithioic acid was synthesized according to a method developed by Gotthardt and co-workers.[19] 1H NMR (300 MHz, NaOD, D_2O) δ 7.65 (d, J = 9 Hz, 4H), 7.12 (d, J = 9 Hz, 4H). *m/z* (%): 306 (M^+, 28%), 273 (66%), 241 (100%), 196

(56%), 152 (58%), 120 (32%), 76 (20%). Briefly, the compound was dissolved in a 0.1 M NaOH water/ethanol (1:1, v/v) solution at a concentration of 0.5 mM. The gold substrate with the C_6 SAM was then immersed into the solution for sixty minutes to form mixed monolayers using the insertion process.[17] After assembly, the sample was rinsed with water, then ethanol and subsequently dried in a stream of nitrogen gas.

The thioacetic acid S-(4'-acetylsulfanyl-biphenyl-4-yl) ester was synthesized according to procedures described elsewhere.[20,21] 1H NMR (300 MHz, $CDCl_3$) δ 2.54 (s, 6H), 7.70 (d, J = 9 Hz, 4H), 7.57 (d, J = 9 Hz, 4H). *m/*z: (%) 302 (M^+, 100%), 260 (60%), 218 (98%), 184(16%). The compound was dissolved in a freshly distilled CH_2Cl_2 solution (Sigma-Aldrich Corp., St. Louis, MO) at a concentration of 1 mM. The gold bead with C_6 SAM was exposed to this solution for seventy-five minutes to form mixed monolayers. After assembly, the sample was rinsed in distilled CH_2Cl_2 and then exposed to a 0.1 M H_2SO_4 solution for 20 minutes to remove the acetate and deprotect the thiol groups on the outer surface of the SAM. This procedure was followed by rinsing in distilled CH_2Cl_2 solution and dried in a stream of nitrogen gas.

The gold beads with inserted molecules were incubated overnight in a gold nanoparticle solution (Ted Pella Inc., Redding, CA) with a nanoparticle core diameter of about 5 nm, followed by rinsing in water and ethanol, and then drying in a stream of nitrogen gas. The gold nanoparticles were stabilized with citrate ligand. All preparations were performed at room temperature, and all samples were used within two days of preparation.

The CP-AFM measurements were performed using a commercial contact mode AFM (Molecular Force Probe, Asylum Research, Santa Barbara, CA) that was modified in Pittsburgh for conducting probe experiments. Different fixed tip biases were applied, and currents through the junctions were measured (using a pico-ammeter, Chem-Clamp, Dagan Corp., Minneapolis, MN)

as a function of vertical piezo displacement simultaneously with independent force detection between the tip and the sample. The sample was not scanned in horizontal directions, rather the AFM tip was allowed to thermally drift over the sample surface. Currents were measured over different gold nanoparticles for different contact forces and were averaged over the number of repeated measurements to obtain averaged force dependent current-voltage (*I-V*) characteristics of the junction. The experimental error is primarily dominated by uncertainty in the tip to Au nanoparticle contact. Because the tip drifts over the surface variations in the compressing force may cause fluctuations in the measured current. In addition, variations in the biphenyl torsion, arising from environmental changes, could modify the measured conductance. All experiments reported here were performed in an insulating bicyclohexyl solvent (99.0%, Fluka, Switzerland) in order to reduce water contamination and decrease the adhesion forces between the probe and the sample. Pt-coated V-shape silicon cantilevers (MikroMash, Estonia) were used in this work with force constants of 0.8 N/m and tip radii of curvature of about 25 nm. Cantilevers were cleaned in piranha solution (1:3 of 30% H_2O_2/98% H_2SO_4) for 5 minutes, rinsed in ultrapure water (> 18 MΩ·cm) for 1 minute, then soaked in hydrofluoric acid for 20 seconds, and finally rinsed again in ultrapure water for 1 minute followed by drying under vacuum. *Caution! Piranha solution is a very strong oxidant and is extremely dangerous to work with; gloves, goggles, and a face shield should be worn.*

Scanning tunneling microscope (STM) images were obtained with a Nanoscope IIIa STM unit (Veeco Metrology-Digital Instruments Inc., Santa Barbara, CA) operating in air. A tunneling current of 10 pA and tip bias of 0.8 V were used.

5.3. Evidence for Single Molecule Measurements

Single-molecule measurements were achieved by inserting a small number of conductive molecules into a self-assembled monolayer (SAM) of 1-hexanethiol (C_6) on gold. A number of steps were taken to ensure that single-molecules, or at most a few molecules were probed in each experiment. First, the physical properties of assemblies at different preparation stages were characterized using scanning tunneling microscopy (STM). Figure 5-2A shows a constant current STM image of a C_6 SAM with inserted molecules **2** that were exposed to a gold nanoparticle solution. Sizes of the observed bright spots compare reasonably well to a gold nanoparticle core diameter of about 5 nm, implying that they correspond to immobilized nanoparticles (for cross-section, corresponding to the white lines in Figure 5-2, see Figure 5-3). In contrast, the exposure of a pure C_6 SAM to the same solution displays no bright spots (Figure 5-2B), confirming that the gold nanoparticles attach only to the inserted conductive molecules.

Second, the solution concentrations and incubation times for insertion of **1** and **2** into SAMs were adjusted so that 10-15% of the force plots correspond to gold nanoparticles. The majority (>85%) of the data correspond to measurements on non-conducting C_6 molecules with the conducting AFM probe thermally drifting over the sample surface. In the approximation that the nanoparticle distribution is random and the contact area is 5.4 nm^2 (5 nN compressing force and 25 nm tip radius on C_6), this condition corresponds to < 0.2% conducting molecules in the film. These low concentrations were used to minimize the probability of having several molecules form a junction to the nanoparticle. Particularly, for molecule **2**, electrostatic repulsion between negatively charged conducting molecules is likely to inhibit them from coming into close proximity with each other.

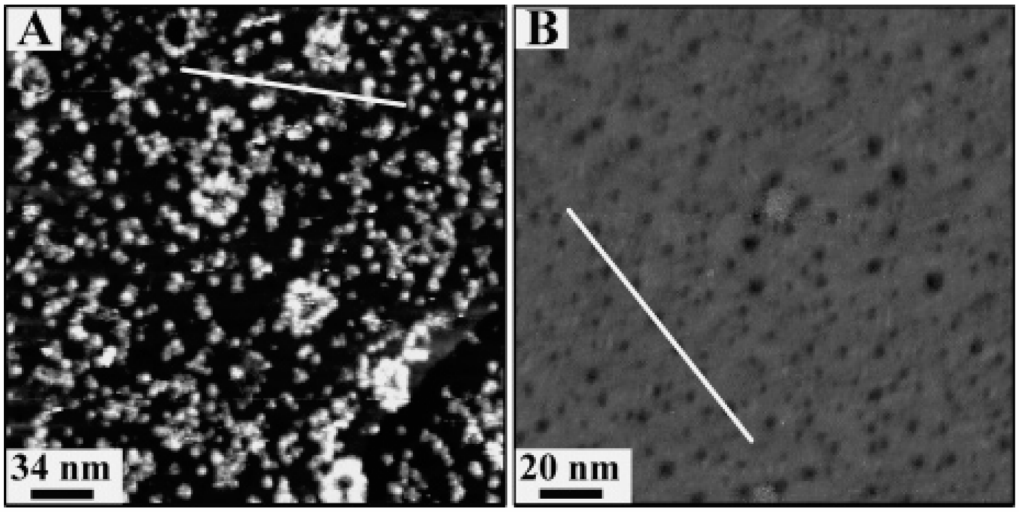

Figure 5-2 A). Constant current STM image of **2** inserted into a C_6 SAM with gold nanoparticles (bright spots) attached to the thiol groups (270 x 270 nm2). B). STM image of a pure C_6 SAM (160 x 160 nm2).

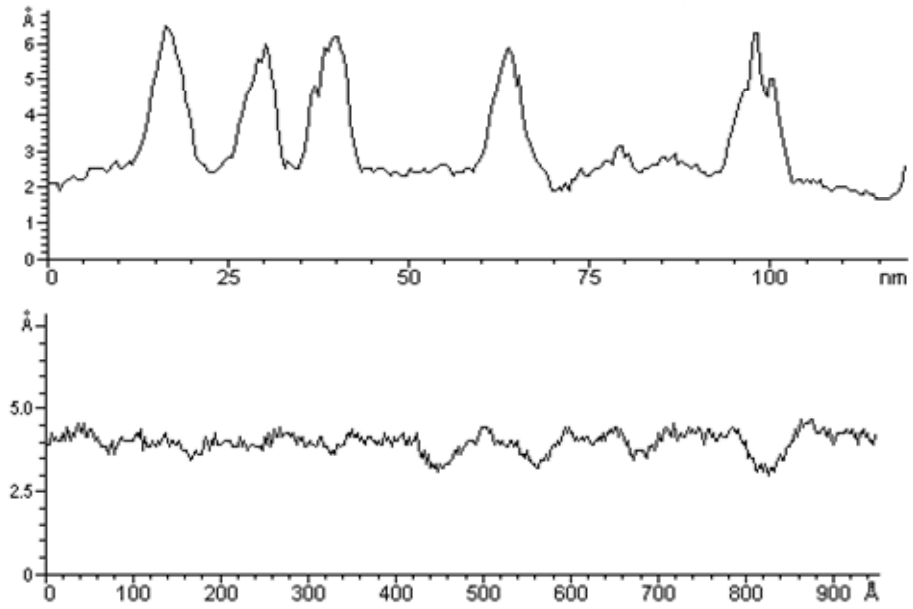

Figure 5-3 A). Cross-section of gold nanoparticles attached to the thiol groups of **2**, corresponding to the white line in Figure 5-2A. B). Cross-section of a pure C_6 SAM, corresponding to the white line in Figure 5-2B.

Because the particles are not necessarily distributed in a random way, a statistical analysis of the measurements was implemented. Under the loading force of 5 nN employed in this study, the contact area between the gold nanoparticle and sample was estimated to be 1.8 nm^2, using a Hertzian elastic contact model.[22] Using a molecular cross-section of 0.3 nm^2, the contact area estimate implies that at most six conducting molecules could contact a single particle. If the number of conducting molecules is distributed on different nanoparticles according to the Poisson distribution,[23] the current magnitudes should appear in clusters, corresponding to the number of conducting molecules.[2] For a coverage of 0.2% conducting molecules, the probability of two being under a nanoparticle would be $< 2x10^{-5}$. Although the distribution is not likely to be random, for the hundreds to a thousand of *I-V* curves collected here, no clustering was observed.

Lastly, if each nanoparticle binds to multiple conducting molecules then one might expect fluctuations in the number of contacts to the nanoparticle. For a Poisson distribution the mean and variance of the distribution should be equal to each other, hence the variances of the current distributions at different biases should scale linearly with the average current, if there were multiple conducting molecules under each nanoparticle. Figure 5-4 shows that variances of the current distributions do not significantly change with the average values of the current (with 95% confidence), indicating that number of molecules contacting nanoparticles stays the same throughout repeated measurements. These variances were obtained from the measurements over five different gold nanoparticles for every applied tip bias. The standard deviation of variances of current distributions under the different biases is 0.05. Therefore, a statistical analysis shows that the number of molecules contacting nanoparticles stays the same throughout repeated measurements.

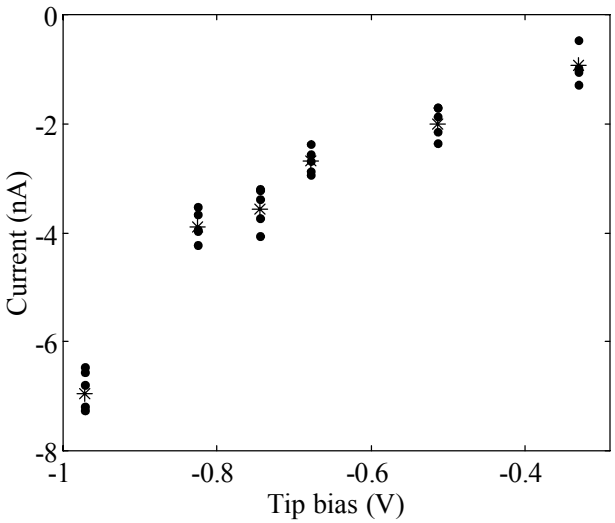

Figure 5-4 The current (dots) as a function of the applied tip bias and corresponding means of currents (asterisks) for molecule **2** (S_2C-Ar-CS_2).

Since the sample preparation conditions are likely to yield single contacting molecules per site and it is unlikely that a fixed, large number would occur, we conclude that single-molecule measurements were achieved.

5.4. Comparison of Conduction through Au-S-Ar-S-Au and Au-S_2C-Ar-CS_2-Au

Electrical conduction measurements were performed using CP-AFM at different applied tip biases so that the current through the junction could be measured as a function of tip-sample separation simultaneously with independent detection of the force between the tip and the sample. Force dependent *I-V* characteristics of the junction were obtained by averaging over a thousand repeated measurements under different tip biases within ±1 Volt bias range. Higher

biases were not applied because of the increased possibility of chemically modifying the molecule.

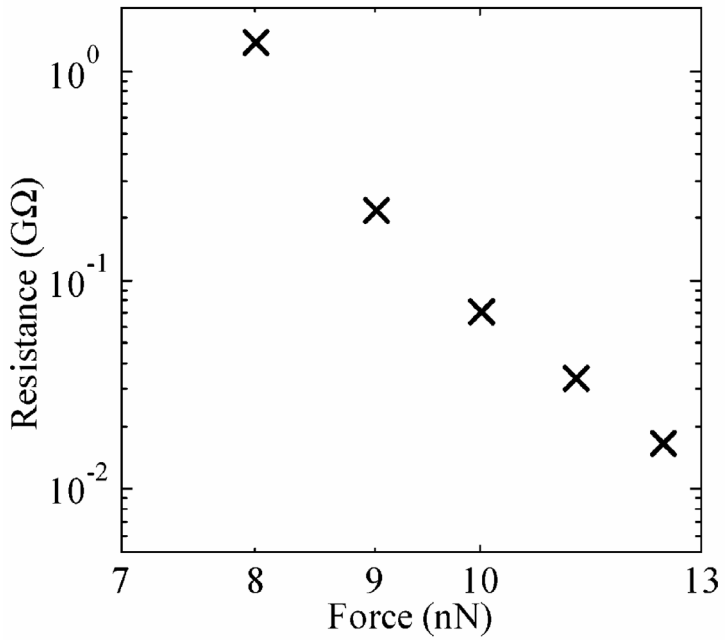

Figure 5-5 Log-log plot of junction resistance (x) versus loading force for the pure C_6 SAM.

Control CP-AFM measurements over a pure C_6 SAM (no conducting molecules present) show that at least 7 nN of loading force, with which the cantilever pushes the probe into the sample, is required to make sufficient electrical contact and cause observable currents of 10 pA or larger. Experiments were performed in bicyclohexyl solvent. The linear portions of the *I-V* curves (within ±0.2 Volt bias range) were fit to straight lines, and the determined slopes were used to define force dependent junction resistances. Figure 5-5 plots the log of the junction resistance (x) versus the log of loading force. Among the possible factors which can change the observed junction resistances under applied loading force are: (a) a change in the contact area and the

tunneling distance arising from film compression between the AFM tip and the sample, and (b) intra- and interchain order of the molecular film.[24] Measurements over a C_6 monolayer with incubation in the gold nanoparticles solution (no conducting molecules) produced similar force dependent junction resistances, confirming that the gold nanoparticles only attach when the conductive molecules **1** and **2** are inserted.

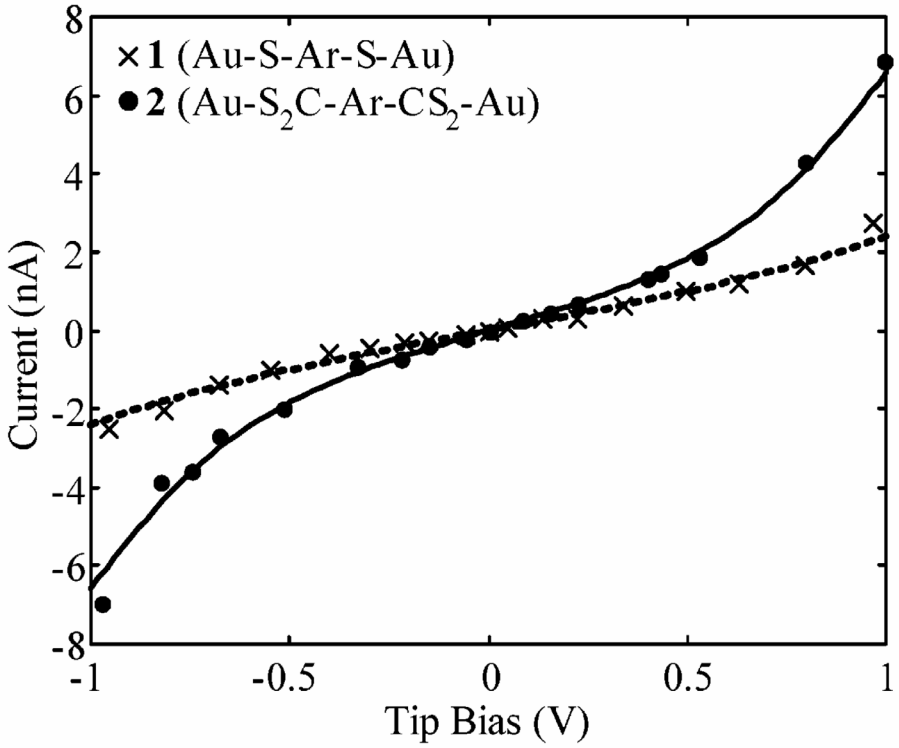

Figure 5-6 The current is shown as a function of the applied tip bias under loading force of 5nN. The curves are fits to Equation 1 for Au-S-Ar-S-Au (x) and for Au-S_2C-Ar-CS_2–Au (●).

Figure 5-6 shows the averaged single-molecule *I-V* characteristics for **1** (x) and **2** (●) inserted into a C_6 SAM in bicyclohexyl solvent under fixed loading force of 5 nN. Each data symbol shown in Figure 5-6 represents the mean value of current for a series of repeated measurements

on different gold nanoparticles under a particular tip bias. The standard deviation of the current found in different measurements is similar, or smaller, to the size of the symbol. *I-V* characteristics of the conducting molecules were collected under 5 nN loading force in order to eliminate any direct contribute through the C_6 SAM to the observed electrical current. For applied 5 nN loading force no measurable currents (less than several pA) within ±1 V bias range on pure C_6 monolayer were observed. A nonzero loading force was still required to make good electrical contact between the conductive probe and gold nanoparticles and to obtain reproducible measurements, however. The symmetrical *I-V* dependences for both bias polarities confirm the formation of good electrical contacts between the molecules and both gold electrodes.

To quantify these results, the *I-V* curves are compared to the Simmons model for nonresonant tunneling through metal-insulator-metal junction,[25-27] in which the temperature independent current *I* (in A) is given by

$$\mathrm{I} = \left(\frac{e\sigma}{4\pi^2\hbar s^2}\right)\left\{\begin{array}{l}\left(\Phi - \frac{eV}{2}\right)\exp\left[-\frac{2(2m_e)^{1/2}}{\hbar}\alpha\left(\Phi - \frac{eV}{2}\right)^{1/2}s\right] - \\ -\left(\Phi + \frac{eV}{2}\right)\exp\left[-\frac{2(2m_e)^{1/2}}{\hbar}\alpha\left(\Phi + \frac{eV}{2}\right)^{1/2}s\right]\end{array}\right\} \tag{5.1}$$

where m_e is the electron mass, σ is the cross-sectional area of the molecule, s is the length of the tunneling barrier, Φ is the barrier height relative to the Fermi level of the gold, and V is the applied tip bias. The unitless parameter α is 1 if the model of an electron tunneling through a rectangular barrier model applies. Deviations from this simple model are manifest as $\alpha \neq 1$, and can arise from a nonrectangular shape of the barrier and/or an effective mass ($m^* = m_e\alpha^2$) for the tunneling electrons through the junction.[27] The lengths of the potential barriers for molecules **1** (s = 1.1 nm) and **2** (s = 1.3 nm) were estimated from molecular lengths, as obtained from

semiempirical calculations using the PM3 method. In a corresponding way, the cross-sectional area of the molecule of 0.3 nm^2 was used.

By adjusting two parameters Φ and α, the molecular *I-V* curves for **1** and **2** were fit using Equation 1. These fits are shown by the dotted and solid lines in the Figure 5-6. The best fit curves have parameter values of Φ = 1.35±0.03 eV and α = 0.59±0.02 for Au-S-Ar-S-Au junction and Φ = 0.59±0.02 eV and α = 0.66±0.01 for the Au-S_2C-Ar-CS_2-Au junction. If the value for α is interpreted in terms of an effective mass for the tunneling electrons, then m^* = 0.35m_e for **1** and m^* = 0.44m_e for **2**. As expected, the potential barriers observed here are smaller than those found for alkanethiol SAMs[27] of the same length.

These results demonstrate enhanced electrical conduction for the junctions involving molecule **2** over that for molecule **1**. Specifically, the tunneling barrier height was about 0.8 eV smaller and the magnitude of the current for **2** was higher than that of **1**. This latter result is especially noteworthy since the tunneling length for **2** is approximately 0.2 nm larger than that for **1** (because of the presence of two extra carbon-carbon bonds), and one would expect the opposite trend.[9]

The observed *I-V* characteristics were linear within the bias range of ±0.15 Volts. Figure 5-7 shows the averaged single-molecule *I-V* characteristics in the Ohmic range of applied tip biases for **1** (x) and **2** (•) inserted into a C_6 SAM in bicyclohexyl solvent under fixed loading force of 5 nN. Each data symbol shown in Figure 5-7 represents the mean value of current for a series of repeated measurements on the different gold nanoparticles under particular tip bias; error bars represent the standard deviation of the mean). Ohmic dependences observed in the *I-V* curves are consistent with the Simmons model in the low-bias region[25-27] for nonresonant tunneling through a m-M-m interface. The linear portions of the *I-V* curves were fit by straight lines, and

the obtained slopes were used to determine junction resistances. These fits are shown by the dotted and solid lines in the Figure 5-7 for molecules **1** and **2**, respectively. From the fit, the junction resistance for molecules **1** and **2** were 0.5±0.03 GΩ and 0.37±0.02 GΩ, respectively. As expected, these resistance values are smaller than that found for the single molecule resistance of the similarly long octanedithiol (~0.8 GΩ),[2] which has no conjugation.

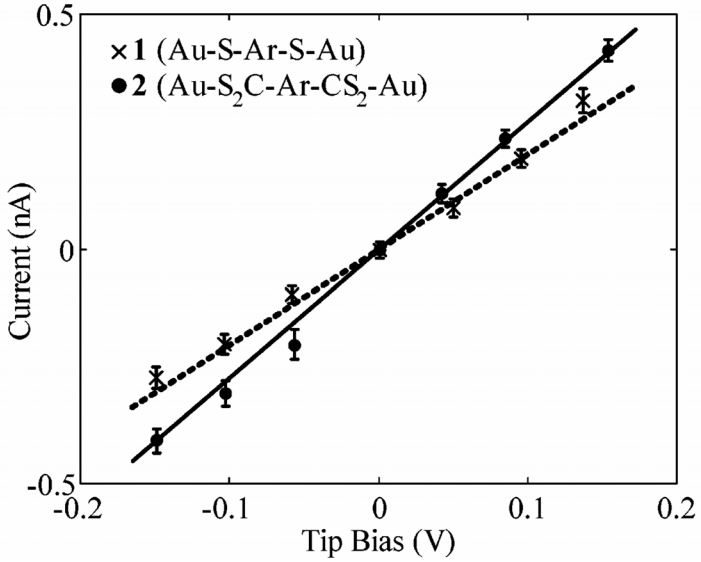

Figure 5-7 The current is shown as a function of the applied tip bias under loading force of 5nN and the corresponding linear fits for Au-S-Ar-S-Au (x) and for Au-S_2C-Ar-CS_2–Au (•).

The smaller observed resistances for the junction involving molecule **2** would not be expected, if only molecular lengths were relevant to the electrical conduction. This can be seen from the Simmons model in the low-bias regime for the nonresonant direct tunneling mechanism,[28] in which the junction resistance is predicted to scale exponentially with the length of the tunneling barrier, s. In particular, $R=R_0\, s\, \exp(\beta s)$, where R_0 is a contact resistance and β is a tunneling decay coefficient,

$$\beta = \frac{2(2m_e)^{1/2}}{\hbar}\alpha\sqrt{\Phi} \tag{5.2}$$

Using the values for Φ and α, obtained from the fits in Figure 5-6, the tunneling decay coefficients are 7 nm^{-1} for **1** and 5 nm^{-1} for **2**. With these parameters the resistance of a hypothetical molecule **1** with the length of molecule **2** (0.2 nm longer) can be computed, and is predicted to be 2.5 GΩ. In fact, the observed resistance for the junction involving molecule **2** is smaller than that of the shorter molecule **1**. The explanation for the improved conductance of **2** must lie with better overlap of the electronic wavefunctions of the molecule and substrate for the conjugated thiol linker of **2**, providing smaller contact resistance and/or smaller tunneling decay coefficient.

By modeling conducting molecules as cylinders with a diameter of 0.6 nm and a length *s* for the width of the tunneling barrier, the molecular resistivities can be estimated from the measured junction resistances. Molecules **1** and **2** display resistivities of 12.9 Ω-cm and 8 Ω-cm, respectively. These values are about one order of magnitude smaller than the intrinsic resistivity of bulk Germanium (about 65 Ωcm).

5.5. Conclusions

These measurements show enhanced conduction for the junctions involving biphenyl-4,4'-dicarbodithioic acid (**2**) over that for biphenyl-4,4'-dithiol (**1**). In particular, the magnitude of the current is higher for **2** as compared to **1** and the tunneling barriers that are extracted from the *I-V* curves are smaller. This result is especially significant since the tunneling length for **2** is larger than that for **1**, and based on the difference in tunneling length one would expect the

opposite order. Characterization of the contacts implies that only one conducting molecule binds to a Au nanoparticle, so that the smaller tunneling barrier must lie with the difference in overlap of the electronic wavefunctions of the substrate and the molecules. In summary, this work demonstrates that a conjugated molecule with a double thiol linker on both sides is a more conductive contact in Au-molecule-Au junctions than a single thiol linker on both sides.

BIBLIOGRAPHY

1. Cui, X. D.; Zarate, X.; Tomfohr, J.; Sankey, O. F.; Primak, A.; Moore, A. L.; Moore, T. A.; Gust, D.; Harris, G.; Lindsay, S. M. *Nanotechnology* **2002**, *13*, 5.

2. Cui, X. D.; Primak, A.; Zarate, X.; Tomfohr, J.; Sankey, O. F.; Moore, A. L.; Moore, T. A.; Gust, D.; Nagahara, L. A.; Lindsay, S. M. *J. Phys. Chem. B* **2002**, *106*, 8609.

3. Zhou, C.; Deshpande, M. R.; Reed, M. A.; Jones II, L.; Tour, J. M. *Appl. Phys. Lett.* **1997**, *71*, 611.

4. Reed, M. A.; Zhou, C.; Muller, C. J.; Burgin, T. P.; Tour, J. M. *Science* **1997**, *278*, 252.

5. Bumm, L. A.; Arnold, J. J.; Dunbar, T. D.; Allara, D. L.; Weiss, P. S. *J. Phys. Chem B.* **1999**, *103*, 8122.

6. Beebe, J. M.; Engelkes, V. B.; Miller, L. L.; Frisbie, C. D. *J. Am. Chem. Soc.* **2002**, *124*, 11268.

7. Fan, F. F.; Yang, J.; Cai, L.; Price, Jr., D. W.; Dirk, S. M.; Kosynkin, D. V.; Yao, Y.; Rawlett, A. M.; Tour, J. M.; Bard, A. J. *J. Am. Chem. Soc.* **2002**, *124*, 5550.

8. Kushmerick, J. G.; Holt, D. B.; Pollack, S. K.; Ratner, M. A.; Yang, J. C.; Schull, T. L.; Naciri, J.; Moore, M. H.; Shashidar, R. *J. Am. Chem. Soc.* **2002**, *124*, 10654.

9. Wold, D. J.; Haag, R.; Rampi, M. A.; Frisbie, C. D. *J. Phys. Chem. B* **2002**, *106*, 2813.

10. Yaliraki, S. N.; Kemp, M.; Ratner, M. A. *J. Am. Chem. Soc.* **1999**, *121*, 3428.

11. Xue, Y.; Datta, S.; Ratner, M. A. *J. Chem. Phys.* **2001**, *115*, 4292.

12. Conwell, E. M.; Wu, M. W. *Appl. Phys. Lett.* **1997**, *70*, 1867.

13. Samanta, M. P.; Tian, W.; Datta, S.; Henderson, J. I.; Kubiak, C. P. *Phys. Rev. B* **1996**, *53*, 7626.

14. Datta, S.; Tian, W.; Hong, S.; Reifenberger, R.; Henderson, J. I.; Kubiak, C. P. *Phys. Rev. Lett.* **1997**, *79*, 2530.

15. Bussac, M. N.; Michoud, D.; Zuppiroli, L. *Phys. Rev. Lett.* **1998**, *81*, 1678.

16. Tivanski, A. V.; Bemis, J. E.; Akhremitchev, B. B.; Liu, H.; Walker, G. C. *Langmuir* **2003**, *19*, 1929.

17. Cygan, M. T.; Dunbar, T. D.; Arnold, J. J.; Bumm, L. A.; Shedlock, N. F.; Burgin, T. P.; Jones, L.; Allara, D. L.; Tour, J. M.; Weiss, P. S. *J. Am. Chem. Soc.* **1998**, *120*, 2721.

18. Clavilier, J. F.; Guinet, G.; Durand, R. *J. Electroanal. Chem.* **1980**, *107*, 205.

19. Gotthardt, H. P.; Wolfgang; Gutowski, P. *Chemische Berichte* **1988**, *121*, 313.

20. Alov, M. N.; Novikov, S. E.; Kobylinskii, D. B.; Moskvichev, Y. A.; Kryukova, G. G.; Yasinskii, O. A.; Budanov, N. A. *Russ. J. Org. Chem.* **1998**, *34*, 1160.

21. Hendrik Ehlich, A. S.; Schmidbaur, H. *Inorg. Chem.* **2002**, *41*, 3721.

22. Weihs, T. P.; Nawaz, Z.; Jarvis, S. P.; Pethica, J. B. *Appl. Phys. Lett.* **1991**, *59*, 3536.

23. Thomas, J. B. *An Introduction to Applied Probability and Random Processes, John Wiley &Sons, Inc.*, New York, **1971**.

24. Tivanski, A. V.; Walker, G. C. submitted for publication to *Langmuir*.

25. Sze, S. M. *Physics of Semiconductor Devices*, *John Wiley &Sons, Inc.*, New York, **1981**.

26. Simmons, J. H. *J. Appl. Phys.* **1963**, *281*, 1793.

27. Wang ,W.; Lee, T.; Reed, M. A. *Phys. Rev. B* **2003**, *68*, 035416.

28. Ratner, M. A; Davis, B.; Kemp, M.; Mujica, V.; Roitberg, A.; Yaliraki, S. *Ann. N. Y. Acad. Sci.* **1998**, 852.

6. PRESSURE INDUCED RESTRUCTURING OF MONOLAYER FILM NANOJUNCTION PRODUCES THRESHOLD AND POWER LAW CONDUCTION[§]

The electrical conduction of metal-molecule-metal junctions formed between Au-supported self-assembled monolayers (SAMs) of 1-hexanethiol, ferrocenyl-1-undecanethiol, and a Pt-coated atomic force microscope tip have been measured under different compressing forces using conducting probe atomic force microscopy. The observed junction resistance had two distinct power law scaling changes with compressing force. Different scaling regions were described through the change in the area of contact, tunneling distance and structure of the film under compression.

6.1. Introduction

Recently, charge transport through metal-molecule-metal (m-M-m) junctions has been studied intensively due to their potential applications to molecular based electronics. In these junctions, a molecular film is typically sandwiched between two metal or semiconductor electrodes. One of the fundamental goals of all electrical conduction measurements in nanojunctions is to understand how structural and electrical properties of nanocontacts and molecules forming junctions influence charge transport through such junctions. The scanning probe microscope (SPM), with the probe serving as one of the metal electrodes has been commonly used to form

[§] This work has been submitted for publication to *Langmuir* coauthored by Alexei V. Tivanski and Gilbert C. Walker

nanojunctions and to study their electrical and structural properties directly, with examples including scanning tunneling microscopy (STM)[1-3] and conducting probe atomic force microscopy (CP-AFM).[4-12] In SPM, the electronic properties of a nanocontact are sensitive to the effects of deformation caused by the interaction force between the probe and the sample,[6-11] thus it is important to measure force and current simultaneously in order to understand mechanical and electrical properties of nanojunctions.

This can be achieved directly using CP-AFM rather than STM where the contact force is not precisely known since it is not controlled independently. Recent studies[6, 8-11] employed CP-AFM to demonstrate the influence of the contact force on the electrical conduction through SAMs involving alkanethiols and conjugated molecules. These measurements showed two power law scaling changes in junction resistance with applied force. While one of the power regions was related to the change in the contact area between the probe and compressing sample, another was less understood and was assigned as apparent changes in the mechanical properties of the film. Here, we report detailed measurements of electrical conduction using CP-AFM[10] for two nanojunctions formed between a Pt-coated AFM tip and a Au-supported self-assembled monolayer under different compressing forces with the objective to correlate electrical conduction through m-M-m junctions with mechanical and structural properties of the film.

The molecular SAMs studied here were 1-hexanethiol (C_6SH) and ferrocenyl-1-undecanethiol ($FcC_{11}SH$). Molecular systems were chosen for the following reasons. While the charge transport mechanism through both SAMs under relatively small applied biases is expected to be nonresonant tunneling, the structure of C_6SH assemblies is more disordered than for $FcC_{11}SH$.[13,14] The ferrocenyl-1-undecanethiol was chosen over similar length dodecanethiol due to the presence of ferrocene-end groups that are expected to decrease the contribution from

chain-to-chain coupling to the electron tunneling through the film in the absence of applied force. Having different structural properties of the films yet the same charge transport mechanism allowed us to probe how the film structure influences the measured nanojunction electrical conduction under compression.

6.2. Experimental details

All self-assembled monolayers were formed by exposing the freshly prepared Au (111) facet of a single crystalline bead to 5 mM ferrocenyl-1-undecanethiol ($FcC_{11}SH$, Dojindo Molecular Technologies, Inc., Gaithersburg, MD) or 1 mM 1-hexanethiol (C_6SH, Sigma-Aldrich Corp., St. Louis, MO) in purified (by distillation) tetrahydrofuran (THF) with soaking times between 4 and 24 hours. After assembly, each sample was rinsed in purified THF and dried in a stream of nitrogen gas. All preparations were performed at room temperature, and all samples were used within one day of preparation.

The CP-AFM measurements were performed using a commercial contact mode AFM (Molecular Force Probe, Asylum Research, Santa Barbara, CA) modified in Pittsburgh for conducting probe experiments. In order to obtain detailed measurements of the current-contact force relationship, different fixed tip biases were applied and currents through the organic film were measured (using a pico-ammeter, Chem-Clamp, Dagan Corp., Minneapolis, MN) as a function of vertical piezo displacement, simultaneously with independent force detection between the tip and the sample. The sample was not scanned in horizontal directions; rather the AFM tip was allowed to thermally drift over the sample surface. Measured currents for different contact forces over different surface locations were averaged over the number of repeated measurements to obtained

averaged force-dependent current-voltage (*I-V*) characteristics of the nanojunction. The experimental error is dominated primarily by the uncertainty in the exact number of molecules forming the junction. Because the tip drifts over the surface, variations in the number of contacting molecules may cause fluctuations in the measured current.

All experiments reported here were performed in an insulating bicyclohexyl solvent (99.0%, Fluka, Switzerland) in order to reduce water contamination and decrease the adhesion forces between the probe and the sample. Cleaned Pt-coated V-shape silicon cantilevers (MikroMash, Estonia) were used in this work where the force constants of each cantilever ranged from 0.4 to 0.6 N/m as determined by the thermal noise method. Cantilevers were cleaned in piranha solution (1:3 of 30% H_2O_2/98% H_2SO_4) for 5 minutes, rinsed in ultrapure water (> 18 MΩ·cm) for 1 minute, then soaked in hydrofluoric acid for 20 seconds, and finally rinsed again in distilled water for 1 minute followed by drying under vacuum. *Caution! Piranha solution is a very strong oxidant and is extremely dangerous to work with; gloves, goggles, and a face shield should be worn*.

6.3. Results and discussion

Typical force and current profiles as a function of vertical piezo displacement for the $FcC_{11}SH$ SAM in bicyclohexyl solvent under fixed tip bias of -2.8 V are shown in Figure 6-1 by solid and dashed lines, respectively. Only approach data are shown. Positive piezo displacements imply that the probe was not in the nominal contact with the surface which occurred at zero nanometers. Negative displacements reflect the continued motion of the cantilever toward the

surface. It is important to mention, that vertical piezo displacements do not correspond to the actual motion of the tip in contact with surface that is a combination of rotation and translation.

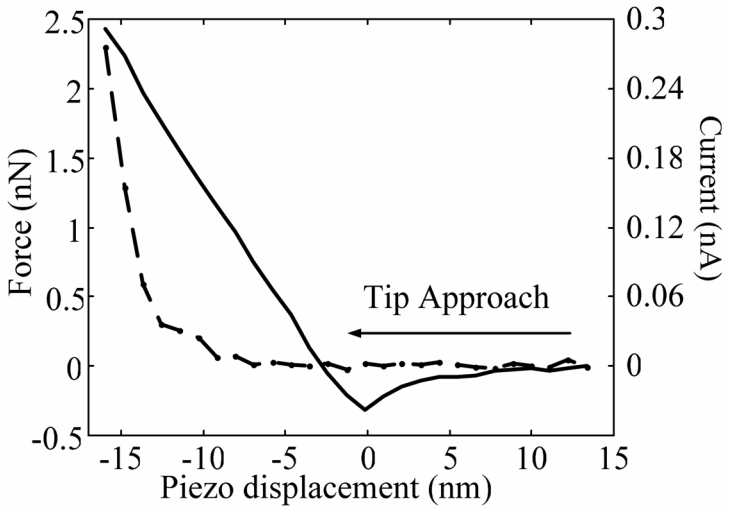

Figure 6-1 Force (solid line) and current (dashed line) profiles measured simultaneously as a function of vertical piezo displacement for the Pt-coated tip over a $C_{11}Fe$ SAM.

The zero force was selected as the force when the tip was far away from the surface. Positive forces after the contact are defined as a loading force with which the cantilever pushes the probe into the surface. Negative forces experienced by the cantilever before surface contact are primarily the attractive electrostatic forces due to the tip-sample capacitance.[7,10] The adhesion force between the probe and the sample was defined as a "pull-off" force measured while the tip was retracting from the surface. The interaction or net force between the tip and underlying film at their contact is considered to be equal to the sum of the two forces: the adhesion force and the loading force. For electrical conduction measurements, bias magnitudes less than 0.2 V were applied, so the bias-dependent adhesion force contribution to the interaction force was not significant, but under higher applied biases, it would need to be considered. Noteworthy, due to

the AFM tip-SAM contact resistance, a nonzero loading force was required to make a good electrical contact between the conductive probe and sample and cause observable currents of ~10 pA or larger. The results shown in Figure 6-1 clearly demonstrate an increase in current with applied loading force and confirm that this type of measurement can indeed be used to measure, with high force sensitivity, load-dependent nanojunction electrical conduction under compression.

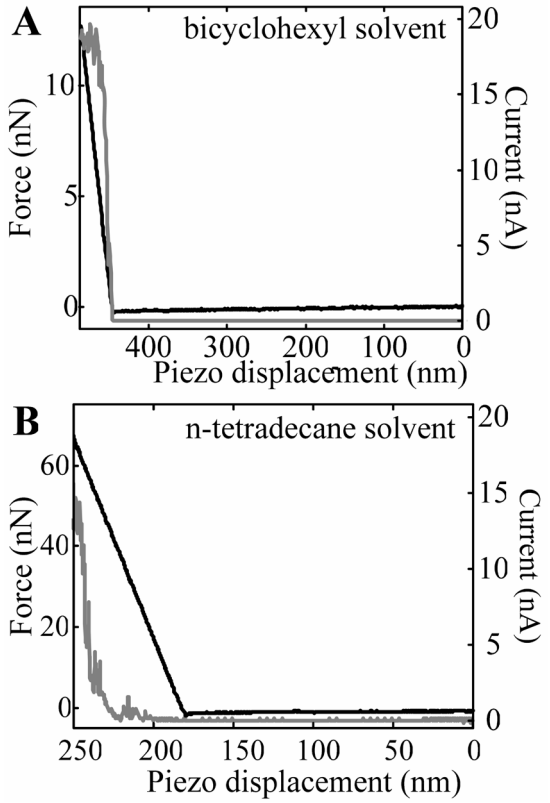

Figure 6-2 Force (black line) and current (gray line) profiles measured simultaneously as a function of vertical piezo displacement for the Pt-coated AFM tip over a crystalline gold substrate (no molecular film present) in bicyclohexyl (A) and in n-tetradecane (B) solvents under fixed tip bias of +0.7 V. Only approach data are shown. The maximum current was limited to 20 nA.

Control CP-AFM measurements over a single crystalline gold surface (no molecular film present) in bicyclohexyl solvent showed that sufficient electrical contact was achieved for the loading forces smaller than 1nN (see Figure 6-2A) and current was increasing steadily until saturation value of 20 nA. Current and force profiles shown in Figure 6-2 were obtained under the fixed tip bias of +0.7 V. On the other hand, similar experiment in n-tetradecane solvent showed that at least 15 nN of additional loading force was required to cause observable currents of ~10 pA or larger and current-force dependence was significantly more complicated than that in bicyclohexyl solvent (See Figure 6-2B). One of the possible explanations of the conduction dependence in n-tetradecane solvent is formation of the solvent layers at the interface between the AFM probe and sample. The absence of such layering effect for the bicyclohexyl solvent is consistent with its branched-like structure. Therefore, bicyclohexyl was chosen over linear alkane solvent in order to avoid this highly undesirable conduction-force dependence that can significantly complicate the interpretation of load-dependent nanojunction electrical conduction change under compression.

Electrical conduction measurements were performed at different applied tip biases with magnitudes smaller than 0.2 Volts so that the current through the junction could be measured as a function of compressing interaction force. Measured currents for different interaction forces were averaged over several hundreds of force plots to obtain averaged force dependent current-voltage (*I-V*) characteristics of the junction. The observed *I-V* characteristics were linear at all interaction forces less than 30 nN within ±0.2 Volts bias range. Ohmic dependence observed in the *I-V* curves are consistent with the Simmons model in the low-bias region[15] for nonresonant tunneling through a m-M-m interface which was expected due to the large molecular HOMO-LUMO gap. Forces higher than 30 nN were not applied due to the noticeably quick decrease in

the magnitude of observed currents indicating the apparent damage of the conductive coating on the tip. The linear portions of the *I-V* curves were fit by straight lines, and the determined slopes were used to define junction resistances as 1/slope, which as expected, were changing under different interaction forces.

Figure 6-3 plots the log of the junction resistances in bicyclohexyl solvent for $FcC_{11}SH$ (A) and C_6SH (B) *versus* the log of compressing interaction force. Each data symbol shown in Figure 6-3 represents the obtained mean value of resistance for a series of repeated measurements over the different surface locations. The standard deviation of the resistance found in different measurements is similar, or smaller, to the size of the symbol. For both molecular systems, two distinct power law scaling regimes were observed. Both scaling regions can be fit closely by straight lines (solid lines in Figure 6-3). In the low-load regime fitted resistance scales as $(force)^{-0.7}$ and $(force)^{-9.8}$ while at loads greater than 15 nN, it scales as $(force)^{-5.2}$ and $(force)^{-1.24}$ for $FcC_{11}SH$ and C_6SH, respectively. It is important to point out that although the threshold forces were somewhat similar (15 nN for $FcC_{11}SH$ and 13 nN C_6SH), the slopes were significantly different for the two SAMs.

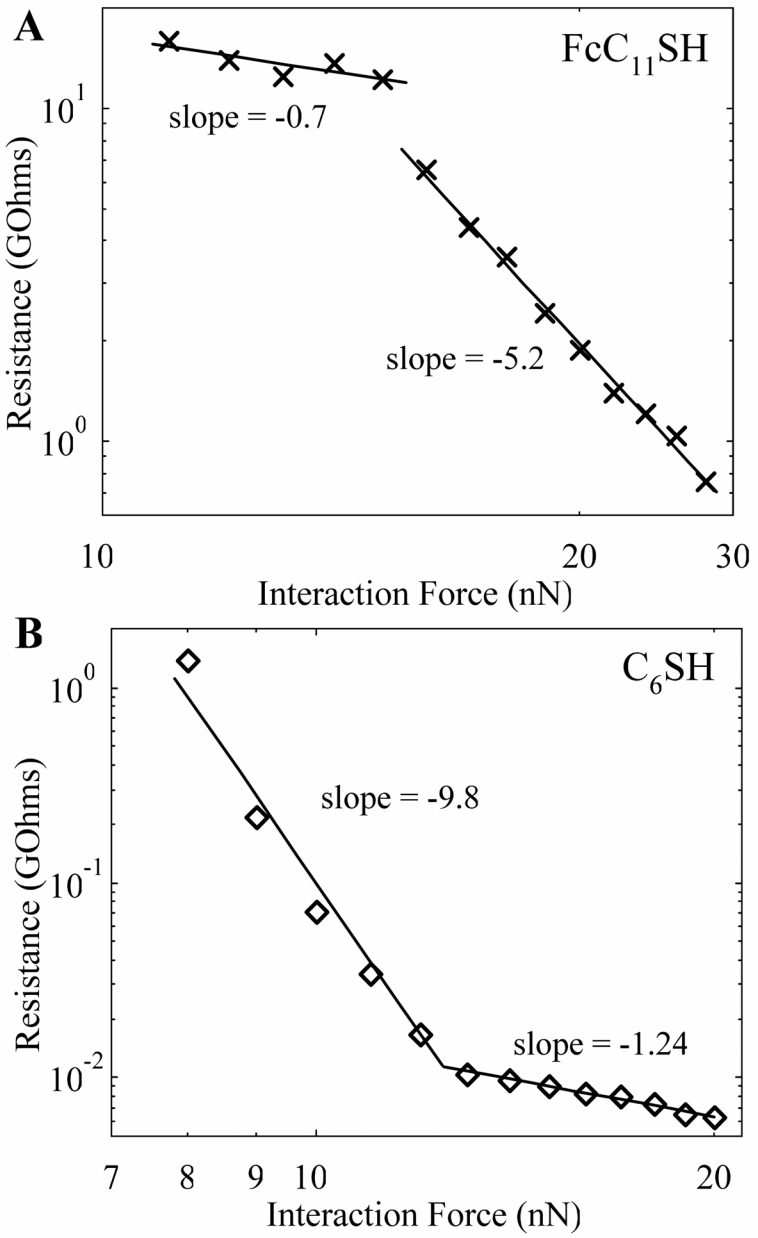

Figure 6-3 Log-log plots of junction resistance *versus* interaction force for $FcC_{11}SH$ (A) and C_6SH (B) SAMs show threshold and two power law scaling regimes. Symbols are averaged data and solid lines are the corresponding linear fit.

Among possible factors which can change the observed junction resistances under applied interaction force are: (a) change in the contact area between the AFM tip and the sample, (b) change in the tunneling distance between two electrodes due to film compression, and (c) intra- and interchain order of the molecular film. Next, a quantitative model that includes change in the elastic contact area and tunneling distance will be introduced together with consideration of the film structure to explain the different power law scaling regions observed in Figure 6-3.

Change in the junction resistance can be related to the change in contact area and film indentation using a Hertzian elastic contact model with adhesion force between the probe and sample included.[16] The contact area, a^2, between a spherical tip of radius r penetrating into a uniform elastic film may be estimated as $a^2=(Fr/K)^{2/3}$ (6.1), where F is the interaction force and K an effective modulus equals $(4/3)[(1-v^2_t)/E_t+(1-v^2_s)/E_s]^{-1}$ (E_s, v_s, E_t, v_t are Young's modulus and Poisson's ratio of the sample and Pt-coated AFM tip, respectively). The Poisson ratio for most materials is between 0.25 and 0.5 so assuming $v_t \sim v_s \sim 0.33$, an effective modulus can be approximated as $K=1.5E_tE_s/(E_t+E_s)$. The indentation of the film is given by $d=a^2/r=F^{2/3}/(K^{2/3}r^{1/3})$ (6.2). The tunneling current can be related to the contact area and film indentation by $I \sim a^2 exp(\beta_{ts}d)$ (6.3), where the tunneling decay coefficient β_{ts} represents the change in tunneling current with change in the length of the tunneling gap due to film compression. It is important to mention that this tunneling coefficient represents both through-bond and chain-to-chain tunneling paths.[17] By substituting Equations 6.1 and 6.2 into Equation 6.3, the junction resistance R which is inversely proportional to the tunneling current in the bias range of applied here depends on the interaction force as: $R(F)\sim F^{-2/3}exp(-SF^{2/3})$, with $S=\beta_{ts}/(K^{2/3}r^{1/3})$.

Hence, a plot of $Ln(RF^{2/3})$ *versus* $F^{2/3}$ should be linear with a slope of $-S$. The tip radius of curvature of ~ 25 nm was obtained from the measurements of bias-dependent long-range non-contact capacitive forces as a function of the tip-sample separation.[21] Although appropriate measured values for elasticity modulus are not available, assuming E_t=170 GPa,[18] E_s=7 GPa[19] and the tunneling decay coefficient as (12 nm^{-1}),[17] the expected slope for the electrical conduction change with compressing force over closely packed and ordered SAM would be $-S$ = -0.9 $nN^{-2/3}$.

Figure 6-4 shows a plot of $Ln(RF^{2/3})$ *versus* $F^{2/3}$ for $FcC_{11}SH$ (points) and C_6SH (triangles) SAMs where data in both scaling regions closely followed a linear dependence, as predicted by the above model. Data in different regions were fit to straight lines, as shown by the solid lines in Figure 6-4. As will be discussed later, the overall dependence for both films can be separated into three common regions: the first region with a slope of -2.3 $nN^{-2/3}$ for C_6SH, a second region with a slope of -0.01 $nN^{-2/3}$ for $FcC_{11}SH$, and a third region with slopes of -0.93 and -0.12 $nN^{-2/3}$ for $FcC_{11}SH$ and C_6SH, respectively.

The first region for C_6SH in Figure 6-4 showed a linear decrease with a slope that is 2.6 times larger than that predicted from the above model. We argue that the origin of this deviation lies in the structural properties of the film. The structure of C_6SH assemblies was shown to be significantly more disordered than that of longer chains.[14] Such a structure would result from a combination of conformationally disordered and thermally disordered alkyl chains because of the presence of gauche kinks and weak interchain interactions, respectively. Under compression, the film structure becomes more ordered due to increase in molecular packing, eventually forming closely packed assemblies at a compression force around 13 nN, similar to the longer chains. In terms of the previously described model, a change in the molecular packing under compression

forces can be represented as the tip indents through more compressible film; assuming the elasticity modulus of the sample is E_s=1.6 GPa, the observed slope of -2.3 $nN^{-2/3}$ can be obtained. The absence of such a region for the $FcC_{11}SH$ assemblies is consistent with their more ordered structure in the absence of applied force.

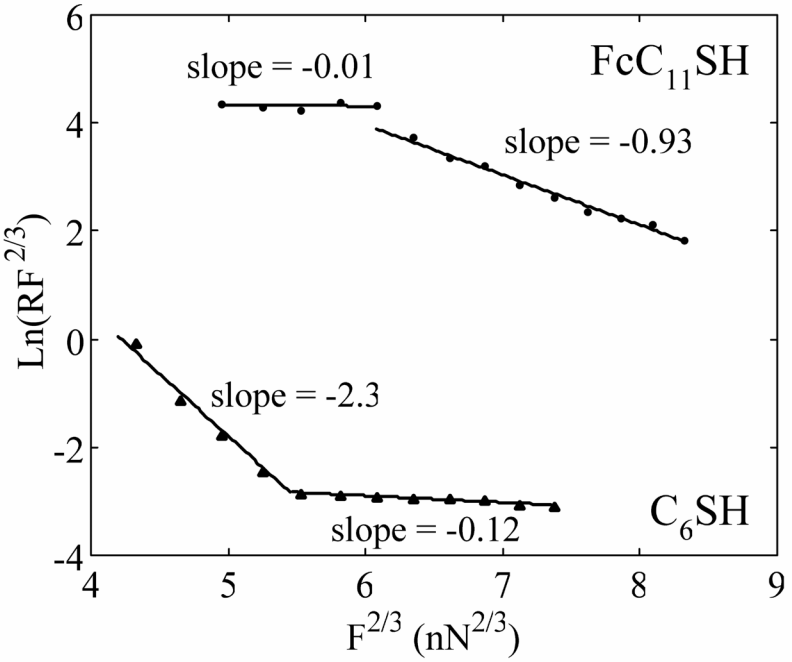

Figure 6-4 Plot of $Ln(RF^{2/3})$ as a function of $F^{2/3}$ for $FcC_{11}SH$ (points) and C_6SH SAMs (triangles) with the corresponding linear fit (solid lines).

The second region in Figure 6-4 for $FcC_{11}SH$ showed a linear decrease with a slope of almost exactly zero, thus the junction resistance is directly proportional to $F^{-2/3}$ which represents the case when the contact area change is the dominant contribution to the junction resistance. The presence of Fe in the $FcC_{11}SH$ SAM decreases the chain-to-chain coupling to the electron tunneling through the film (the coverage density of the $FcC_{11}SH$ SAM is roughly two times smaller than that for the similar length alkanethiol[13]), so under relatively small applied forces

(less than 15 nN in our case), the through-bond charge transfer is the dominant tunneling mechanism. Again, within the small force regime, the change in junction appears to be limited by a change in the number of conductive contacts between the AFM tip and the sample which is proportional to the contact area. Under larger compression forces (15 – 30 nN in our case), the number of the gauche defects in the alkyl chains increases, resulting in a decrease of the through-bond coupling efficiency; the increase in the volume density of the chains will result in a concomitant increase in the chain-to-chain coupling efficiency to electron tunneling.

The third region in Figure 6-4 showed a linear decrease with slopes of -0.95 and -0.12 $nN^{-2/3}$ for $FcC_{11}SH$ and C_6SH, respectively. While for the $FcC_{11}SH$ monolayer, the observed slope is the same as the one predicted by the elastic compression model over closely packed and compressed monolayer film presented above, it differs significantly for the C_6SH SAM. In the case of C_6SH, direct tunneling between the Pt-coated AFM tip and Au substrate can become the dominant path to the charge transfer due to the significantly smaller tunneling length compared with the case for the longer chain SAM. Similar studies performed on C_8 and C_{10} alkanethiol SAMs showed that the observed slopes in this region are nearly independent of the molecular length,[5] suggesting that change in the charge transfer mechanism is not sufficient to explain the smaller slope observed here. Since the tunneling decay coefficient is not expected to change with compressing forces applied here, the origin of the smaller observed slope lies in the change of the mechanical properties of the film. Apparently, for the shorter C_6SH SAM the mechanical properties are dominated by the supporting Au substrate. Assuming an elasticity modulus of the sample similar to Au with E_s~77 GPa, the above model predicts a slope of -0.22 $nN^{-2/3}$, reasonably close to -0.12 $nN^{-2/3}$ observed here.

We also note that unlike the C_6SH SAM, the $FcC_{11}SH$ sample shows a discrete transition between two scaling regions occurring at around 15 nN. For the tip radius of about 25 nm used in these experiments, a contact area of 11 nm^2 can be obtained using the Hertzian model, and the loads producing the abrupt transitions correspond to pressures close to 1.3 GPa. Barena et al[20] studied the change of the molecular packing in SAMs of alkanethiols on Au induced by external pressure. They observed, consistent with our work, discrete changes in film thickness accompanied by simultaneous change in friction versus applied load that were attributed to a collective transition to denser molecular configurations. Pressures at which the first discrete change occurred for a similar length monolayer in Barena's work were about 0.5 GPa which is similar to the threshold pressure observed here. A small discrepancy is probably due to the sharper tip used in their work (15 nm radius of curvature). Thus, we believe that the origin of the discrete change between the second and third regions for the $FcC_{11}SH$ SAM is due to a transitional increase in the volume density of alkyl chains that makes the chain-to-chain coupling contribution to the tunneling charge transfer efficient. The absence of such a discrete change for the C_6SH SAM is consistent with different structural properties of the films, as discussed previously.

In summary, electrical conduction through molecular m-M-m junctions under compression was investigated using conducting probe atomic force microscopy (CP-AFM). Observed junction resistances showed two distinct power laws scaling changes with compressing interaction force for both 1-hexanethiol and ferrocenyl-1-undecanethiol SAMs. These regions were quantitatively described using an elastic model for the change in contact area and tunneling gap between the AFM tip and the sample, including the different molecular structures of the films.

BIBLIOGRAPHY

1. Bumm, L. A.; Arnold, J. J.; Dunbar, T. D.; Allara, D. L.; Weiss, P. S. *J. Phys. Chem. B* **1999**, *103*, 8122.

2. Gorman, C. B.; Carroll, R. L; Fuierer, R. R. *Langmuir* **2001**, *17*, 6923.

3. Xu, B.; Tao, N. J. *Science* **2003**, *301*, 1221.

4. Fan, F. F.; Yang, J.; Cai, L.; Price, Jr., D. W.; Dirk, S. M.; Kosynkin, D. V.; Yao, Y.; Rawlett, A. M.; Tour, J. M.; Bard, A. J. *J. Am. Chem. Soc.* **2002**, *124*, 5550.

5. Cui, D.; Zarate, X.; Tomfohr, J.; Sankey, O. F.; Primak, A.; Moore, A. L.; Moore, T. A.; Gust, D.; Harris, G.; Lindsay, S. M. *Nanotechnology* **2002,** *13*, 5.

6. Gomar-Nadal, E.; Ramachandran, G. K.; Chen, F.; Burgin, T.; Rovira, C.; Amabilino, D. B.; Lindsay, S. M. *J. Phys. Chem. B* **2004**, *108*, 7213.

7. Leatherman, G.; Durantini, E. N.; Gust, D.; Moore, T. A.; Moore, A. L.; Stone, S.; Zhou, Z.; Rez, P.; Liu, Y. Z.; Lindsay, S. M. *J. Phys. Chem. B* **1999**, *103*, 4006.

8. Wold, D. J.; Frisbie, C. D. *J. Am. Chem. Soc.* **2001**, *123*, 5549.

9. Lee, T.; Wang, W.; Klemic, J. F.; Zhang, J. J.; Su, J.; Reed, M. A. *J. Phys. Chem. B* **2004**, *108*, 8742.

10. Tivanski, A. V.; Bemis, J. E.; Akhremitchev, B. B.; Liu, H.; Walker, G. C. *Langmuir* **2003**, *19*, 1929.

11. Ishida, T.; Mizatani, W.; Aya, Y.; Ogiso, H.; Sasaki, S.; Tokumoto, H. *J. Phys. Chem. B* **2002**, *106*, 5886.

12. Suganuma, Y.; Trudeau, P. -E.; Dhirani, A. –A. *Phys. Rev. B* **2002**, *66*, 241405.

13. Chidsey, C. E. D.; Betozzi, C. R.; Putvinski, T. M.; Mujsce, A. M. *J. Am. Chem. Soc.* **1990**, *112*, 4301.

14. Porter, M. D.; Bright, T. B.; Allara, D. L.; Chidsey, C. E. D. *J. Am. Chem. Soc.* **1987**, *109*, 3559.

15. Simmons, J. H. *Appl. Phys.* **1963**, *281*, 1793.

16. Weihs, T. P.; Nawaz, Z.; Jarvis, S. P.; Pethica, J. B. *Appl. Phys. Lett.* **1991**, *59*, 3536.

17. Slowinski, K.; Chamberlain, R. V.; Miller, C. J.; Majda, M. *J. Am. Chem. Soc.* **1997**, *119*, 11910.

18. Burnham, N, A.; Colton, R. J. *J. Vac. Sci. Technol. A* **1989**, *7*, 2906.

19. Joyce, A.; Thomas, R. C.; Houston, J. E.; Michalske, T. A.; Crooks, R. M. *Phys. Rev. Lett.* **1992**, *68*, 2790.

20. Barrena, E.; Ocal, C.; Salmeron, M. *J. Chem. Phys.* **2000**, *113*, 2413.

21. Tivanski, A. V.; Walker, G. C. submitted for publication to *JACS*.

7. CONCLUDING REMARKS AND FUTURE OUTLOOK

In this work, ultrafast infrared spectroscopy and conducting probe atomic force microscopy (CP-AFM) have been used to study temporally and spatially resolved electron transfer (ET) reactions in solutions and thin organic interfaces.

Ultrafast infrared spectroscopy study presented in the second chapter of this thesis has been used to reveal the coupling of vibrational excitations to photoinduced ET in a mixed-valance transition metal complex $[(CN)_5Os^{II}CNRu^{III}(NH_3)_5]^-$ (OsRu). The time-resolved infrared spectra of OsRu in formamide (FA) and deuterium (D_2O) water solutions following optical excitation and reverse electron transfer were presented. We have showed that non-totally symmetric vibrational mode is populated after reverse ET process. The measured reverse electron transfer rates were greater than 3×10^{12} s^{-1}. We have measured the vibrational relaxation time of *trans* CN in D_2O and FA. Our results showed faster vibration relaxation in D_2O than in FA, reflecting the correlation between vibrational relaxation time of the OsRu and the IR absorption cross section of the solvent. We have provided a simulation of the spectral dynamics in FA and D_2O solutions. In this simulation we included effects of vibrational excitation and relaxation together with effects of the coupling between high frequency stretch-CN mode and low frequency solvent modes.

CP-AFM has been used to measure the electrical conductance of nanocontacts between gold-grafted polythiophene self-assembled monolayer (SAM) and conductive tip in tetradecane solvent under different applied load (Chapter 3). We have presented theoretical and

experimental results of how the electrostatic part of the adhesion force depends on the applied external bias. Obtained results showed good agreement with the analytical expressions of the capacitance force as a function of applied bias and tip-sample separation both at the jump off event and at long-range forces. We observed an increase in electrical conduction with increasing applied pressure. Under pressure, the contact area change alone could not explain the observed conductivity; the potential barrier for charge injection was found to be reduced. Based on the adhesion force *versus* applied bias dependence and current-voltage characteristics of polythiophene molecules, we determined that characterization of electrical properties of conducting polymers at nanoscale using CP-AFM requires taking into account an offset in the interaction force determined by the bias-dependent adhesion force.

A novel method to probe charge transfer involving electroactive groups on the nanoscale by measuring the adhesion forces as a function of applied bias in an electrolyte-free environment using CP-AFM was demonstrated in Chapter 4. Simultaneous and independent measurements of currents and bias-dependent adhesion forces under different applied tip biases between the conductive AFM probe and the electroactive 11-ferrocenylundecanethiol SAMs revealed reversible peak-shaped current-voltage (*I-V*) characteristics and correlated maxima in the potential-dependent adhesion force. Trapped positive charges in the molecular junction were found to correlate with high conduction in a feature showing negative differential resistance. A mechanism involving two-step resonant hole transfer through the occupied molecular orbitals (MOs) of ferrocene-end groups *via* sequential oxidation and subsequent reduction, where a hole is trapped by the phonon relaxation, is proposed to explain the observed current-force correlation. These results suggest a new approach to probe charge transfer involving

electroactive groups on the nanoscale by measuring the adhesion forces as a function of applied bias in an electrolyte-free environment.

The importance of the molecular linking unit influences to the tunneling efficiency in metal-Molecule-metal (m-M-m) junctions was established in Chapter 5. Single molecule CP-AFM measurements of electrical conduction through m-M-m junctions showed enhanced conduction for the junctions involving biphenyl-4,4'-dicarbodithioic acid (**2**) double thiol linker on both sides over that for biphenyl-4,4'-dithiol (**1**) single thiol linker. In particular, the magnitude of the current was higher for **2** as compared to **1** and the tunneling barriers that were extracted from the *I-V* curves were smaller. This result is especially significant since the tunneling length for **2** is larger than that for **1**, and based on the difference in tunneling length one would expect the opposite order. Characterization of the contacts implied that only one conducting molecule binds to a Au nanoparticle, so that the smaller tunneling barrier must lie with the difference in overlap of the electronic wavefunctions of the substrate and the molecules.

Chapter 6 described CP-AFM measurements of how electrical conduction through molecular m-M-m junctions changes under compression and how these changes can be correlated with structural and mechanical properties of the thin organic films. In this study, the observed junction resistances showed two distinct power laws scaling changes with compressing interaction force for both 1-hexanethiol and ferrocenyl-1-undecanethiol SAMs. These regions were quantitatively described using an elastic model for the change in contact area and tunneling gap between the AFM tip and the sample, including the different molecular structures of the films.

Several straightforward suggestions can be made for *future work*. The development of the technique to probe charge transfer involving electroactive groups on the nanoscale is only at its

early stages. First of all, this method can be tried on different concentrations, lengths and types of electroactive molecules. By inserting small number of redox-active molecules into corresponding length insulating alkanethiol SAM, charge transfer using this method can be probed on a single molecule level. The effect of surrounding media is far from been understood. Quantitative analysis for the exact energies of the electronic states participating in ET relative to the mean Fermi level of metal electrodes is needed. It would provide valuable insight into the detailed mechanism of charge transfer in and through MO of electroactive groups.

For many of the assemblies of nanosized objects that have been created and can be created, chemical and physical connectors are needed to guide objects into self alignment and then hold them collectively. Some connectors, like the gold-thiol chemical bond, are widely used yet still far from well understood. As demonstrated in Chapter 5, the conjugated double thiol linker can be used instead of the single thiol-gold bond. Many other connectors are needed to be synthesized and characterized and research in this direction will be important and essential for the future of molecular-based electronic devises.

In addition, nanoscience will also demand new developments in techniques for the determination of structural and electrical properties of nanosized objects. Here we presented a technique to correlate electrical conduction with structural and mechanical properties of relatively simple SAMs. This method can be extended to different organic films, for example involving conducting polymers where the structural properties are expected to be disordered in the absence of applied compressing force.